Measurement of the CP Violating Phase ϕ_s and the Decay Width Difference $\Delta\Gamma_s$ in the Decay $B_s^0 \to J/\psi\phi$ with the ATLAS Experiment

Claudio Heller

München 2013

Measurement of the CP Violating Phase ϕ_s and the Decay Width Difference $\Delta\Gamma_s$ in the Decay $B_s^0 \to J/\psi\phi$ with the ATLAS Experiment

Claudio Heller

Dissertation
an der Fakultät für Physik
der Ludwig–Maximilians–Universität
München

vorgelegt von
Claudio Heller
aus München

München, den 18.06.2013

Erstgutachter: Prof. Dr. Jochen Schieck
Zweitgutachter: Prof. Dr. Christian Kiesling
Tag der mündlichen Prüfung: 26.07.2013

Zusammenfassung

Ein Merkmal des neutralen B_s^0 Mesons ist die Oszillation zwischen Teilchen und Antiteilchen vor dem Zerfall, welches CP Verletzung durch die Interferenz von Mischung und Zerfall ermöglicht. Der zeitabhängige $B_s^0 \to J/\psi\phi$ Zerfall wird durch die Zerfallsbreite Γ_s und den Zerfallsbreitenunterschied $\Delta\Gamma_s$ charakterisiert. Die $B_s^0 - \bar{B}_s^0$ Oszillation ist durch die Massendifferenz Δm_s bestimmt und die CP Verletzung wird durch die relative Phase ϕ_s zwischen der Oszillation und dem Zerfall beschrieben. Die Analyse des Zerfallskanals bietet die Möglichkeit die Vorhersagen des Standard Models der Teilchenphysik für diese Größen zu testen. Insbesondere hat die Messung der CP verletzenden Phase ϕ_s das Potenzial die Vergrößerung des kleinen Standard Model Wertes durch Neue Physik zu enthüllen.
In der vorliegenden Arbeit wird die Messung von ϕ_s, Γ_s und $\Delta\Gamma_s$ im Zerfall $B_s^0 \to J/\psi\phi$ präsentiert. Die Analyse verwendet Daten, die mit dem ATLAS Detektor, in den durch den LHC bei einer Schwerpunktsenergie von $\sqrt{s} = 7\,\text{TeV}$ erzeugten $p - p$ Kollisionen, aufgenommen wurden. Die analysierte Datenmenge entspricht einer integrierten Luminosität von $4.9\,\text{fb}^{-1}$. Nach der Rekonstruktion und Selektion der Daten wird eine zeitabhängige Winkelanalyse des $B_s^0 \to J/\psi\phi$ Zerfalls durchgeführt. Dabei werden zwei Methoden zur Bestimmung des Flavors der B_s^0 Mesonen im Anfangszustand verwendet. Die relevanten Parameter werden durch die Verwendung einer Maximum-Likelihood-Fit-Methode bestimmt, die die Detektoreffizienz und Detektorauflösung berücksichtigt. Mögliche Beiträge durch S-Wellen Zerfälle und fehlrekonstruierte Zerfälle von B_d^0 Mesonen sind in der Fitfunktion enthalten. Das Ergebnis der Messung stimmt mit der Standard Model Vorhersage überein und wird als Konfidenzbereich mit 68 %, 90 % und 95 % in der $\phi_s - \Delta\Gamma_s$ Ebene präsentiert.

Abstract

A feature of the neutral B_s^0 meson is that it can oscillate into its antiparticle before it decays, which can give rise to CP violation due to interference of the two processes mixing and decay. The time-dependent $B_s^0 \to J/\psi\phi$ decay is characterized by the decay width Γ_s and the decay width difference $\Delta\Gamma_s$. The $B_s^0 - \bar{B}_s^0$ oscillation is governed by the mass difference Δm_s, and the CP violation is described by the relative phase ϕ_s between the mixing and the decay. The analysis of the decay channel provides the possibility to test the predictions of the Standard Model of particle physics for those parameters. In particular the measurement of the CP violating phase ϕ_s has the capability to unveil enhancement of the small Standard Model value by New Physics.
In this thesis the measurement of ϕ_s, Γ_s and $\Delta\Gamma_s$ in the decay $B_s^0 \to J/\psi\phi$ is presented. The analysis makes use of an integrated luminosity of $4.9\,\mathrm{fb}^{-1}$ that was collected with the ATLAS detector in $p-p$ collision produced by the LHC at a center-of-mass energy of $\sqrt{s} = 7\,\mathrm{TeV}$. After the reconstruction and selection of the decay channel, a time-dependent angular analysis of the $B_s^0 \to J/\psi\phi$ decay is performed. An untagged as well as a tagged analysis, using opposite side flavor tagging to determine the production flavor of the B_s^0 mesons, are presented. The parameters of interest are extracted through the application of an unbinned maximum likelihood fit method, which takes detector efficiency and resolution effects into account. A possible contribution from S-wave decays to the data sample as well as the contamination due to reflections from B_d^0 decays are incorporated in the fit. The result of the measurement is found to be consistent with the Standard Model prediction and is presented as 68 %, 90 % and 95 % confidence regions in the $\phi_s - \Delta\Gamma_s$ plane.

Contents

Chapter 1

Introduction

For centuries scientists have been investigating matter and are searching for the answer to the question what it is made of. Since the early 1970s the Standard Model of particle physics [1–3] has been the accepted theory describing the current knowledge of elementary particles and their interactions. Three generations of fermion pairs, the quarks and the leptons, constitute the fundamental particles of the Standard Model. For each particle there exists an antiparticle that has the same mass but opposite charge. The three interactions, weak, electromagnetic and strong interaction, are represented by force mediating particles, the gauge bosons.
During the development of the Standard Model, the theory did not only explain experimental observations, but it also predicted the existence of new particles, e.g. charm, bottom and top quarks, which were not yet discovered at that time. During the last decades the Standard Model has been verified and tested with high precision and great success in numerous high energy collider experiments. The latest and probably most prominent success of the Standard Model is the prediction of the Higgs boson. The electroweak symmetry breaking via the Higgs mechanism and the Higgs boson were already predicted independently by several scientists in 1964 [4–8]. However, the existence of the Higgs particle was not acknowledged until March 2013, when the two LHC (Large Hadron Collider) experiments, ATLAS and CMS, confirmed its experimental observation [9, 10].

Despite being very successful, the Standard Model has some unresolved issues and open questions. One of the deficiencies is the fact that it only accounts for 4.9 % of the known universe as it cannot explain dark matter and dark energy. Recent measurements of perturbations in the Cosmic Microwave Background by the Planck satellite [11] determined the share of dark matter

of the universe to be 26.8 %, while the mysterious dark energy contributes the remaining 68.3 %. The reason for dominance of matter over antimatter in the known universe is another unanswered question. Cosmology and field theory state that the universe was created in the Big Bang 13.8 billion years ago [11]. During the first moments of its existence the universe had an extremely high energy density and was in a perfectly symmetric state where all interactions, except for gravitation, were of the same strength [12]. In the extremely hot and dense plasma, pairs of particle and antiparticle were created and thus matter and antimatter existed in equal amounts. When the universe expanded and cooled down, nearly all of the particle-antiparticle pairs were annihilated to photons. This resulted in the matter to photon ratio of 10^{-9} that can be observed today. While the stars and galaxies in the observable universe consist of the remaining matter, no evidence for significant amounts of antimatter has been found. The excess of matter over antimatter in the universe can be established by an asymmetry in the way matter and antimatter react. In 1967 Andrei Sakharov formulated a mechanism to generate the cosmological matter asymmetry (baryogenesis) [13] that is based on three conditions:

- Non-conservation of baryonic charge,
- Deviation from the thermal equilibrium,
- Breaking of the matter-antimatter symmetry (breaking of the C and CP symmetry.)

The third condition, breaking of the CP symmetry, referred to as CP violation, was discovered in the Standard Model in 1964 by Jim Cronin and Val Fitch in the decay of neutral kaons [14]. CP violation states that the laws of physics are not conserved under a combined transformation of charge conjugation and parity. Charge conjugation means that a particle is transformed into its antiparticle and parity is a mirror transformation.

CP violation in weak interaction was integrated into the Standard Model by Makoto Kobayashi and Toshihide Maskawa [15]. Their formalism required three generations of quarks with two quarks each, although by that time only the three lightest quarks were known. They introduced a quark mixing matrix called Cabibbo-Kobayashi-Maskawa (CKM) matrix that describes the transition probability of one quark to another in flavor changing weak decays.
With the discovery of the bottom quark in 1977 [16], the third quark generation was established and in 1980 Bigi, Carter and Sanda [17, 18] proposed to

search for CP violation in the neutral B meson system. Large time-dependent CP violation was indicated by the unexpected large lifetime ($\tau_B \approx 1.5\,\text{ps}$) of the B mesons. During the next decades huge efforts were made to measure CP violation in the decay of B mesons, which was confirmed in 2001 [19, 20]. However, the CP violation described in the Standard Model is not enough to explain a matter dominated universe [21]. Additional sources for CP violation are needed to explain the baryogenesis leading to the universe we see today. Theoretical models beyond the Standard Model do include new sources of CP violation and could reveal themselves as small deviations from the CKM mechanism. Particular systems that have very small expected values of CP violation provide the possibility to measure these small deviations.

This thesis describes a measurement of the CP violating phase ϕ_s in the decay $B_s^0 \to J/\psi\phi$ using $4.9\,\text{fb}^{-1}$ integrated luminosity collected with the ATLAS experiment in 2011. ATLAS is one of four experiments at the Large Hadron Collider, the largest particle accelerator ever built. The value predicted for ϕ_s by the Standard Model is close to zero [22], and thus a large measured value would clearly indicate New Physics. This is the first measurement at ATLAS that makes use of initial state flavor tagging, improving the precision of ϕ_s by $\approx 40\,\%$ compared to the untagged measurement. In addition the average decay width Γ_s and the decay width difference $\Delta\Gamma_s$ between the heavy and the light B_s^0 meson are extracted. Although these two quantities are not expected to be affected by theories beyond the Standard Model, a precise experimental determination provides a test of theoretical predictions [23]. The results of the untagged and tagged analysis presented in this thesis have been published in [24] and [25]. The results of the tagged analysis were first presented at the Beauty Conference 2013 in Bologna [26]. Furthermore, in the course of the analysis, a method to determine systematic effects from residual misalignment is applied, which is documented in [27].

The thesis is divided into 9 chapters. A short overview of the Standard Model is presented in Chapter 2, followed by the derivation of the time-dependent decay rate of the $B_s^0 \to J/\psi\phi$ decay and a review of results of measurements performed by the collaborations of other experiments. The experimental apparatus, consisting of the LHC accelerator and the ATLAS detector, is introduced in chapter 3. Chapter 4 describes the data collected with the ATLAS detector in 2011 and simulated datasets used in the analysis. The specific selection of the data for the measurement and reconstruction of the signal candidates are discussed in chapter 5. In chapter 6 the different mathematical functions used to describe signal and background properties of the decay are presented and combined into an unbinned maximum likelihood fit. Results of the untagged measurement are discussed in chapter 7. Chapter

8 covers the new components and results of the tagged analysis. Chapter 9 gives a summary of this thesis and discusses possibilities for improvements of the $B_s^0 \to J/\psi\phi$ analysis at ATLAS.

Chapter 2

Theoretical Overview

This chapter deals with the theoretical background of the $B_s^0 \to J/\psi\phi$ decay. First a short overview of the Standard Model of elementary particle physics, focusing on the weak interaction, is given. The CKM mechanism and CP violation are discussed, introducing the parameters of interest for this measurement: ϕ_s, Γ_s and $\Delta\Gamma_s$. Furthermore the time-dependent decay rates of the neutral B_s system, that are used in the analysis, are presented and explained. The effect of possible enhancement to ϕ_s of beyond Standard Model processes and theoretical aspects of the $\Delta\Gamma_s$ measurement are discussed. In the last section the experimental status of the $B_s^0 \to J/\psi\phi$ analysis is reviewed, presenting an overview of the latest results from other experiments.

2.1 Standard Model

The Standard Model of particle physics is a relativistic quantum field theory providing a set of mathematical formalisms describing the elementary particles and the fundamental interactions between them. It has been thoroughly tested in numerous low and high energy experiments and most of its predictions have been confirmed with surprisingly high precision.

According to the Standard Model all matter is made up from two types of elementary fermions: quarks and leptons. They are grouped into three generations, where each generation contains a pair of quarks and a pair of leptons. All stable matter in the visible universe is made from particles from the first generation (up, down, electron, electron neutrino). The fermions of the second (charm, strange, muon, muon neutrino) and third generation

Table 2.1: Elementary fermions of the Standard Model [21].

Particle	**Charge [e]**	**Generation**					
		I	*mass*	II	*mass*	III	*mass*
Quarks	$+\frac{2}{3}$	u	$2.3^{+0.7}_{-0.5}$ MeV	c	1.275 ± 0.025 GeV	t	$173.5 \pm 0.6 \pm 0.8$ GeV
	$-\frac{1}{3}$	d	$4.8^{+0.7}_{-0.3}$ MeV	s	95 ± 5 MeV	b	4.18 ± 0.03 GeV
Leptons	0	ν_e	< 255 eV	ν_μ	< 0.19 MeV	ν_τ	< 18.2 MeV
	-1	e	0.511 MeV	μ	105.658 MeV	τ	1776.82 ± 0.16 MeV

Table 2.2: The three fundamental forces of the Standard Model and their force mediating bosons [21].

Interaction	**Electromagnetic**	**Weak**	**Strong**
Relative Strength	$\frac{1}{137}$	10^{-5}	≈ 1
Range [m]	∞	$\ll 10^{-16}$	$10^{-15} - 10^{-16}$
Interacts between	charged particles	fermions	quarks, gluons
Mediating boson	γ (photon)	$W^{\pm}$, $Z^0 bosons$	g (gluon)
Boson mass [GeV]	0	$\approx 10^2$	0

(top, bottom, tau, tau neutrino) have higher masses and short lifetimes and can only be observed in high energy environments. Until today, only upper limits could be determined for the neutrino masses and thus it is not yet clear if their masses also increase with the generation. All fermions are subject to electroweak interaction, but strong interactions can only occur between quarks, since leptons do not carry color charge. In addition, there exists an antiparticle for each of the fermions with the same mass but opposite charge. The six quarks and six leptons are shown in table 2.1 together with their masses[1] and charges.

The Standard Model includes three out of the four fundamental interactions: electromagnetic, weak and strong interaction. The interactions between the particles are represented by force mediating gauge bosons (see table 2.2). The fourth fundamental force, gravitation, is not part of the Standard Model and its hypothetical force mediating particle, the graviton, has not yet been observed. In particle physics the gravitational force is negligible as its relative strength is very small ($\approx 10^{-38}$ compared to the strong force).

[1]Throughout this thesis the natural units ($\hbar = c = 1$) are used, and thus mass and momentum are given in the energy units eV instead of the actual units eV/c^2 and eV/c.

2.1.1 Electromagnetic Interaction

Quantum Electro-Dynamics (QED) is the theory describing electromagnetic interactions that bind e.g. negatively charged electrons to positively charged atomic nuclei. The massless photon is the force mediating boson of QED. The coupling constant, setting the scale for electromagnetic interactions, is given by Sommerfeld's fine-structure constant $\alpha \approx \frac{1}{137}$. As photons have no mass the range of the electromagnetic force is infinite but it decreases rapidly with distance ($\sim \frac{1}{r}$). QED describes all phenomena involving electrically charged particles by photon interactions. The theory has successfully been tested to very high precision in quantum loops and serves as a model for the other interactions.

2.1.2 Strong Interaction

In 1909 Ernest Rutherford performed a scattering experiment, where he fired alpha particles at a gold foil with a thickness of only a few atom layers [28]. From his observations he concluded the size of the atomic nucleus to be of the order $2 - 7 \times 10^{-15}$ m. This was the beginning of the development of the nuclear model as it is known today, which states that atomic nuclei consist of protons and neutrons. To explore and understand matter and its interactions on even smaller scales, particle accelerators (e.g. SLC, HERA, LEP, Tevatron) have been constructed during the last century. Especially experiments, analyzing the deep inelastic scattering of nucleons by electrons, led to the current understanding of the structure of nucleons, which states that nucleons are bound systems of smaller particles called quarks. The force that holds them together is the strong force [29]. It is more than 100 times stronger than the electromagnetic force and thus is the strongest of the four fundamental interactions. The mediating particle of the strong force is the massless gluon which is also responsible for the attraction between protons and neutrons.

Quantum Chromo-Dynamics (QCD) is the theory describing the strong interactions between quarks and gluons. In addition to electric charge, quarks carry a color charge, which is often just referred to as color. Quarks have one out of three different colors and antiquarks carry the corresponding anticolors. Since gluons carry color charges as well, they interact strongly with each other. This is also the reason why the range of the strong force is extremely small although gluons are massless.
The fact that single quarks cannot exist as free particles, but appear only

as color neutral compounds, is called confinement. Baryons, like the proton, consist of three quarks, each carrying a different color. Mesons are composed of a quark-antiquark pair with corresponding color and anticolor.

2.1.3 Weak interaction

There are two types of weak interaction that are mediated by three massive gauge bosons. Charged currents are mediated by W^+ and W^- bosons whereas neutral currents are mediated by Z^0 boson. Unlike the strong and electromagnetic interaction with their massless photons and gluons, the gauge bosons of the weak force are heavy. $W^\pm$ bosons have a mass of $\sim 80\,\mathrm{GeV}$ and the Z^0 is even heavier with a mass of $\sim 91\,\mathrm{GeV}$ [21]. These three massive gauge bosons were already postulated in 1968 by Sheldon Glashow, Steven Weinberg and Abdus Salam [1–3] who received the Nobel Price for their work on the unification of weak and electromagnetic interaction in 1979. Due to their large mass, the experimental discovery of the weak force mediators was not possible until there were particle accelerators powerful enough to produce them. In 1983 Carlo Rubbia and Simon van der Meer observed all three heavy gauge bosons [30] at the Super Proton Synchrotron at CERN and were awarded with the Nobel Price one year later. Compared to the strong interaction, the coupling strength of the weak interaction is 10^{-5} times smaller which is the reason why it is called weak. As a consequence of the massive gauge bosons, the weak force has only a very small range ($\ll 10^{-16}$) and it has the unique ability to change the flavor of particles. An example for the manifestation of the weak interaction is the radioactive β decay:

$$n \to p + e^- + \bar{\nu}_e$$

A neutron is converted into a proton producing an electron and an antineutrino in addition. On the quark level this means that a down quark transforms into an up quark by radiating a virtual W^-, which decays into an electron and the corresponding antineutrino (see figure 2.1). Even a transition from one quark generation to another is possible in weak decays. The strength of the possible quark transitions is described by the Cabibbo-Kobayashi-Maskawa model that will be explained in section 2.3.

One of the outstanding achievements of the Standard Model is the fact that weak interaction and QED can be joined into a single theory. This unified theory, developed by Glashow, Salam and Weinberg [1–3], is called the electroweak theory. It requires four massless spin-1 bosons as force carriers: one triplet W^1, W^2, W^3 and a singlet B^0. Linear combinations of these yield

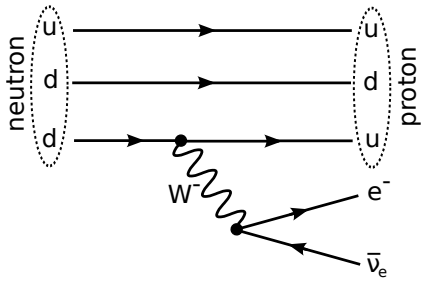

Figure 2.1: Radioactive β decay of a neutron.

the observable gauge bosons (γ, W^+, W^-, Z^0):

$$
\begin{aligned}
W^+ &= \frac{1}{\sqrt{2}}(W^1 - iW^2) \\
W^- &= \frac{1}{\sqrt{2}}(W^1 + iW^2) \\
Z^0 &= W^3 \cos(\theta_W) - B^0 \sin(\theta_W) \\
\gamma &= W^3 \cos(\theta_W) + B^0 \sin(\theta_W)
\end{aligned}
$$

The angle θ_W is called Weinberg angle and parametrizes the mixing of the bosons. This mixing is only valid for massless gauge bosons, but - as already mentioned - experimental observation proved that $W^\pm$ and Z^0 are heavy particles.

The solution to this problem was developed independently by Peter Higgs and two groups of physicists (Robert Brout and Francois Englert; Gerald Guralnik, C. R. Hagen and Tom Kibble) in 1964 [4–8] and is called the Higgs mechanism. It introduces a new field, the Higgs field, and the quantum excitation of one of the components of the field corresponds to a massive particle, the Higgs boson. The Higgs field has a non-zero vacuum expectation value and is responsible for the spontaneous breaking of the electroweak symmetry into the electromagnetic and the weak interaction. The Higgs mechanism gives mass to the gauge bosons $W^\pm$ and Z^0 while the photon remains massless. The masses of all other fermions are explained by their coupling strength to the Higgs boson. After years of unsuccessful searches, the Higgs boson has finally been experimentally observed by the two experiments ATLAS and CMS at CERN's Large Hadron Collider [9, 10].

2.2 Conservation Laws

A cornerstone of the Standard Model of particle physics are several conservation laws based on discrete symmetries. Three of these symmetries are charge conjugation (C), parity transformation (P) and time reversal (T).
Charge conjugation transforms a particle into its antiparticle, changing internal quantum numbers like electric charge or baryon number:

$$C|q\rangle = |\bar{q}\rangle. \tag{2.1}$$

While the laws of QCD and QED are invariant under charge conjugation, processes of particles and antiparticles in weak interactions can react differently and thus violate the C symmetry. An example is the exclusive experimental observation of left-handed neutrinos and right-handed antineutrinos. Left-handed particles have negative helicity which means that spin and velocity are parallel. Particles with positive helicity have a spin anti-parallel to their velocity and are called right-handed. Under charge conjugation a left-handed neutrino would transform into a left-handed antineutrino, but only right-handed antineutrinos could be observed in experiment.
Parity transformation denotes a mirroring of the physical system. When applied to a coordinate $\vec{r}$ or a momentum $\vec{p}$, the parity transformation results in a sign change. On the contrary the angular momentum $\vec{l} = \vec{r} \times \vec{p}$ is invariant under parity transformation.

$$\vec{r} \xrightarrow{P} -\vec{r}, \qquad \vec{p} \xrightarrow{P} -\vec{p}, \qquad \vec{l} \xrightarrow{P} \vec{l}. \tag{2.2}$$

Vectors that do not change sign, like $\vec{l}$, are called axial vectors and vectors, like $\vec{r}$ and $\vec{p}$, that change their sign are called polar vectors. Again the neutrino system serves as an example for the fact that parity is not conserved in weak interaction. Under a parity transformation a left-handed neutrino would become a right-handed neutrino, but the mediating bosons of the weak interaction only couple to left-handed particles, which was first shown in 1956 by Chien-Shiung Wu in the beta decay of polarized ^{60}Co [31]. When applied twice, the parity transformation results in no change of the physical system, and thus it is a unitary operator with eigenvalues ± 1.

Since parity and charge conjugation symmetry are not conserved in weak interactions, it was thought that physical processes remain unchanged under a combined operation of C and P. Under CP transformation a left-handed neutrino becomes a right-handed antineutrino, which agrees with experimental observation. However, in 1964 evidence for violation of CP invariance was found by James Cronin and Val Fitch in the decay of neutral kaons [14]. The

conclusion of their experiment established CP violation in weak interactions which constitutes the basis for further experimental investigation of the topic.

Time reversal T is a third operation besides C and P. It transforms t into -t and thus corresponds to a reversal of motion:

$$\vec{r} \xrightarrow{T} \vec{r}, \qquad \vec{p} \xrightarrow{T} -\vec{p}, \qquad \vec{l} \xrightarrow{T} -\vec{l}. \tag{2.3}$$

As Wolfgang Pauli already stated in 1955 [32], physics is invariant to the combined application of the three transformations C, P and T. This CPT-theorem is a substantial feature of quantum field theory, and conservation of the CPT symmetry has not been disproved with todays achievable precision [21].

2.3 CKM Matrix

Following the discovery of kaons in late 1947 and the introduction of a new quantum number called strangeness, it was found that charged currents ($W^{\pm}$) of the weak interaction allow transition between the first and the second generation of quarks. Unlike in strong and electromagnetic interaction, the transition of an s-quark into a u-quark was observed in the strangeness changing weak decay of $K^+ \to \pi^0 + e^+ + \nu_e$. This observation and the long lifetime of kaons inspired Nicola Cabibbo to the introduction of an angle in 1963 [33] to describe the difference between $d \to u$ and $s \to u$ transitions. It was derived by comparing the semileptonic decays of kaons and pions and is nowadays called the Cabibbo angle θ_C. In the following years **G**lashow, **I**lliopoulos and **M**aiani developed the GIM mechanism [34], that explained the low decay rate of $K_L^0 \to \mu^+\mu^-$ and predicted a new quark, the charm quark. Joining Cabibbo's theory with the GIM mechanism yields a 2×2 mixing matrix:

$$\begin{pmatrix} |d'\rangle \\ |s'\rangle \end{pmatrix} = \begin{pmatrix} \cos\theta_C & \sin\theta_C \\ -\sin\theta_C & \cos\theta_C \end{pmatrix} \begin{pmatrix} |d\rangle \\ |s\rangle \end{pmatrix}. \tag{2.4}$$

The matrix depends only on the Cabibbo angle and describes the weak states d' and s' as superpositions of the physical states d and s. The transition probabilities between them are given by the sine and cosine of θ_C.

The extension of the formalism and the mixing matrix to three quark generations was developed by Makoto Kobayashi and Toshihide Maskawa [15]. When publishing their work in 1972, they predicted the bottom and top quark (before experimental observation of the charm quark) and presented a

3×3 quark mixing matrix, the Cabibbo-Kobayashi-Maskawa (CKM) matrix:

$$\begin{pmatrix} |d'\rangle \\ |s'\rangle \\ |b'\rangle \end{pmatrix} = \underbrace{\begin{pmatrix} V_{ud} & V_{us} & V_{ub} \\ V_{cd} & V_{cs} & V_{cb} \\ V_{td} & V_{ts} & V_{tb} \end{pmatrix}}_{V_{CKM}} \begin{pmatrix} |d\rangle \\ |s\rangle \\ |b\rangle \end{pmatrix}. \tag{2.5}$$

The CKM matrix is required to be unitary to conserve the total probability and can be parametrized by three Euler angles (θ_{12}, θ_{23} and θ_{31}) and a CP violating complex phase δ.

$$V_{CKM} = \begin{pmatrix} c_{12}c_{13} & s_{12}c_{13} & s_{13}e^{-i\delta} \\ -s_{12}c_{23} - c_{12}s_{23}s_{13}e^{i\delta} & c_{12}c_{23} - s_{12}s_{23}s_{13}e^{i\delta} & s_{23}c_{13} \\ s_{12}s_{23} - c_{12}c_{23}s_{13}e^{i\delta} & -c_{12}s_{23} - s_{12}c_{23}s_{13}e^{i\delta} & c_{23}c_{13} \end{pmatrix}. \tag{2.6}$$

Cosines and sines of the mixing angles are denoted by c_{ij} and s_{ij}. θ_{12} is equivalent to the Cabibbo angle θ_C.

An approximation of the CKM matrix was introduced by Lincoln Wolfenstein [35] utilizing an expansion of each element as a power series in the parameter $\lambda = sin(\theta_C)$.

$$V_{CKM} = \begin{pmatrix} 1 - \lambda^2/2 & \lambda & A\lambda^3(\rho - i\eta) \\ -\lambda & 1 - \lambda^2/2 & A\lambda^2 \\ A\lambda^3(1 - \rho - i\eta) & -A\lambda^2 & 1 \end{pmatrix} + \mathcal{O}(\lambda^4) \tag{2.7}$$

The four parameters λ, A, ρ and η are related to the standard parameterization in the following way [36, 37]:

$$s_{12} = \lambda = \frac{|V_{us}|}{\sqrt{|V_{ud}|^2 + |V_{us}|^2}}, \tag{2.8}$$

$$s_{23} = A\lambda^2 = \lambda \left| \frac{V_{cb}}{V_{us}} \right|, \tag{2.9}$$

$$s_{13}e^{i\delta} = A\lambda^3(\rho + i\eta) = \frac{A\lambda^3 \left(\bar{\rho} + i\bar{\eta}\right) \sqrt{1 - A^2\lambda^4}}{\sqrt{1 - \lambda^2} \left[1 - A^2\lambda^4 \left(\bar{\rho} + i\bar{\eta}\right)\right]}. \tag{2.10}$$

The Wolfenstein parameterization visualizes that transitions within one quark generation, represented by diagonal matrix elements, are more likely than transitions between different quark generations (off-diagonal elements). A global fit using all available measurements combined with theory predictions yields $\lambda = 0.22535 \pm 0.00065$, $A = 0.811^{+0.022}_{-0.012}$, $\bar{\rho} = 0.131^{+0.026}_{-0.013}$ and $\bar{\eta} = 0.345^{+0.013}_{-0.014}$ [21].

Unitarity Constraints

The unitarity of the CKM matrix implies various relations between its complex elements [36]: 6 normalization relations and six orthogonality relations. The latter are

$$\sum_{i=1}^{3} V_{ji} V_{ki}^{*} = 0 \qquad j,k = 1,\ldots,3, \quad j \neq k. \tag{2.11}$$

Taking into account unitarity, a geometrical representation of the structure of the CKM matrix can be constructed. Each of the orthogonality relations can be visualized geometrically as a triangle in the complex plane. The shape of each unitarity triangle is different but they all possess the same area equal to half of the Jarlskog invariant J [38] defined as $J \sum_{m,n} \epsilon_{ikm}\epsilon_{jlm} = Im[V_{ij}V_{kl}V_{il}^{*}V_{kj}^{*}]$. J can be derived from equation 2.11 and accounts for the amount of CP violation in the SM. Combining the results of all available measurements yields $J = 2.96^{+0.20}_{-0.16} \times 10^{-5}$ [21].

The unitarity triangle corresponding to the relation

$$V_{ud}V_{ub}^{*} + V_{cd}V_{cb}^{*} + V_{td}V_{tb}^{*} = 0 \tag{2.12}$$

has three sides that are of $\mathcal{O}(\lambda^3)$ and large angles [39], and is often referred to as "The Unitarity Triangle" of the CKM matrix. The relation corresponds to the decay of B_d mesons, and the shape of the triangle has been experimentally well constrained by measurements at the B-factories Belle and BaBar. Rescaling and normalization yields the usual representation of the unitarity triangle which is shown in figure 2.2. The complex coordinates of the vertices of the triangle are (0,0), (1,0) and $(\bar{\rho}, \bar{\eta})$ with

$$\bar{\rho} \equiv \left(1 - \frac{\lambda^2}{2}\right)\rho \qquad and \qquad \bar{\eta} \equiv \left(1 - \frac{\lambda^2}{2}\right)\eta. \tag{2.13}$$

The inner angles of the triangle are defined by

$$\alpha \equiv \arg\left(-\frac{V_{td}V_{tb}^{*}}{V_{ud}V_{ub}^{*}}\right), \qquad \beta \equiv \arg\left(-\frac{V_{cd}V_{cb}^{*}}{V_{td}V_{tb}^{*}}\right), \qquad \gamma \equiv \arg\left(-\frac{V_{ud}V_{ub}^{*}}{V_{cd}V_{cb}^{*}}\right). \tag{2.14}$$

Instead of (α, β, γ) the notation (ϕ_1, ϕ_2, ϕ_3) with $\phi_1 = \beta$, $\phi_2 = \alpha$ and $\phi_3 = \gamma$ is also common.

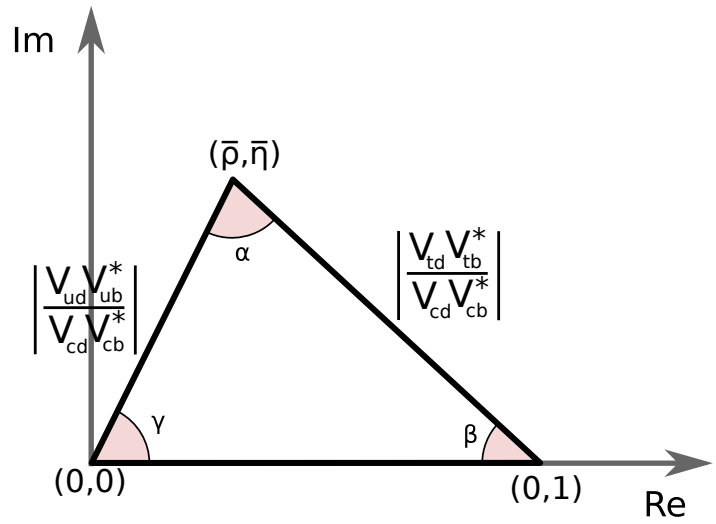

Figure 2.2: Unitarity triangle corresponding to the B_d system

In this thesis an analysis of the decay $B_s^0 \to J/\psi\phi$ is presented. The orthogonality relation describing the B_s^0 system is

$$V_{us}V_{ub}^* + V_{cs}V_{cb}^* + V_{ts}V_{tb}^* = 0 \tag{2.15}$$

and the corresponding unitarity triangle is shown in figure 2.3. The small angle β_s, defined as

$$\beta_s = \arg\left(-\frac{V_{ts}V_{tb}^*}{V_{cs}V_{cb}^*}\right), \tag{2.16}$$

of this unitarity triangle is related to the CP violating phase ϕ_s which is one of the parameters of interest of the $B_s^0 \to J/\psi\phi$ analysis (see section 2.5).

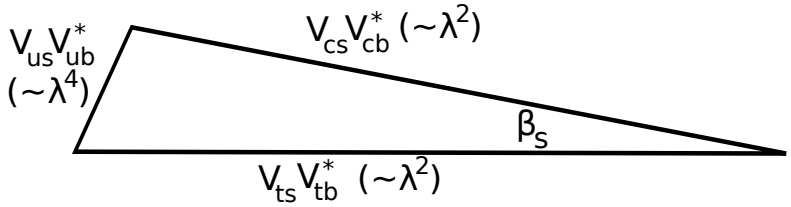

Figure 2.3: Unitarity triangle corresponding to the unitarity relation of the B_s^0 system (equation 2.15). λ is the sine of the Cabibbo angle.

In general, the measurement of all of the parameters of a unitarity triangle is an overconstraint and serves therefore as a precision test of the Standard

Model predictions. To fulfill the unitarity constraints of the CKM matrix, each of the six unitarity triangles must close exactly. Non-fulfillment of the unitarity constraints would be evidence for the incompleteness of the Standard Model and would signal new physics. Latest results of measurements of the CKM parameters can be seen in figure 2.4 [40]. To this day the results are in good agreement with the Standard Model predictions.

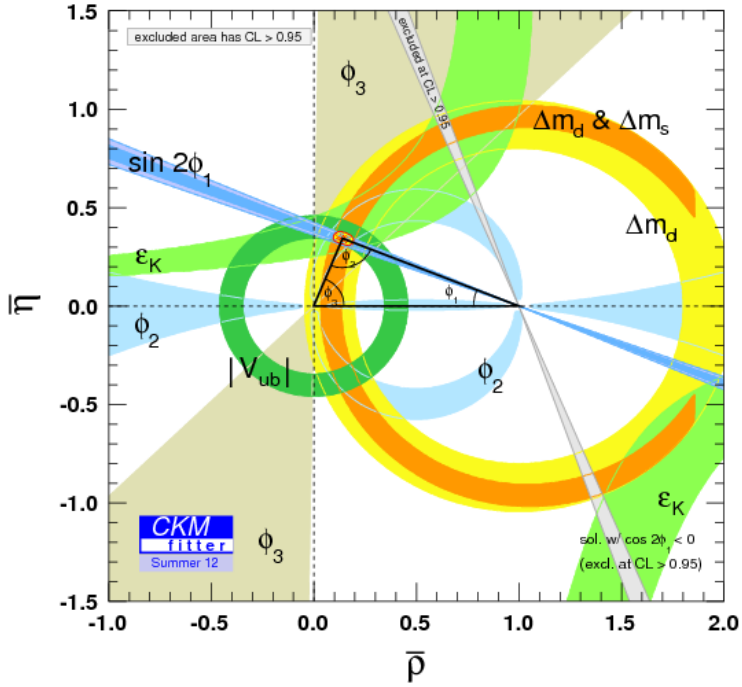

Figure 2.4: Constraints in the $\bar{\rho}$ - $\bar{\eta}$ plane. The red hashed region of the global combination constraining the upper corner of the triangle corresponds to 68 % CL. [40]

2.4 CP Violation in the Decay of Neutral Mesons

In the Standard Model CP violation is described by a complex phase in the CKM matrix (see section 2.3). The first sign of CP violation was observed in the neutral kaon system. The two neutral kaons, K^0 and its antiparticle $\bar{K^0}$, can oscillate into each other before they decay via weak interaction. This

can be observed by producing a pure K^0 beam and studying it after a couple of meters. One will find that it contains both particles K^0 and antiparticles $\bar{K^0}$. K^0 and $\bar{K^0}$ are the flavor eigenstates of the system. The two mass eigenstates are quantum mechanical superpositions of the flavor eigenstates and one of them is short-lived (K_S^0) while the other is long-lived (K_L^0). At first it was thought that the mass eigenstates were also CP eigenstates, as the K_S^0 decays to two pions and a decay of the K_L^0 to three pions was observed. However, in 1964 Cronin and Fitch performed an experiment to measure a better upper limit for the CP violating decay $K_L^0 \to \pi\pi$ [39]. K^0 and $\bar{K^0}$ were produced 17 meters in front of the spectrometer, and over the distance the K_S^0 component completely fades away and a pure K_L^0 beam remains. The surprising result of the experiment [14] was a branching ratio of

$$\frac{\Gamma(K_L^0 \to \pi\pi)}{\Gamma(K_S^0 \to \pi\pi)} = \left[(2.0 \pm 0.4) \times 10^{-3}\right]^2 .$$

This measurement showed that the mass eigenstates are not equivalent to the CP eigenstates and thus established CP violation as a fact. K_L^0 consists of a dominant CP odd part and a small CP even component and K_S^0 contains in turn a small CP odd component in addition to its dominant CP even component.

The source of CP violation in the decay of neutral mesons is the same for the K^0, D^0, B^0 and B_s^0 systems. The subsequent sections discuss the theory of neutral meson mixing by means of the B_s^0 system, the time evolution of the eigenstates and different types of CP violation in the decay of neutral mesons.

2.4.1 Neutral Meson Mixing

The oscillation between a neutral meson and its antiparticle is referred to as neutral meson mixing which, in the Standard Model, is described by box diagrams. The one loop Feynman diagrams for the B_s^0 system are illustrated in figure 2.5. The transitions via u, c and t quarks are shown, but the top quark plays a dominant role due to its large mass, since the amplitude of the process is proportional to the mass of the exchanged fermion.

The initial state of the oscillating B_s system is a superposition of B_s^0 and $\bar{B_s^0}$ and can be denoted as [41]

$$|\psi(0)\rangle = a(0)|B_s^0\rangle + b(0)|\bar{B_s^0}\rangle. \tag{2.17}$$

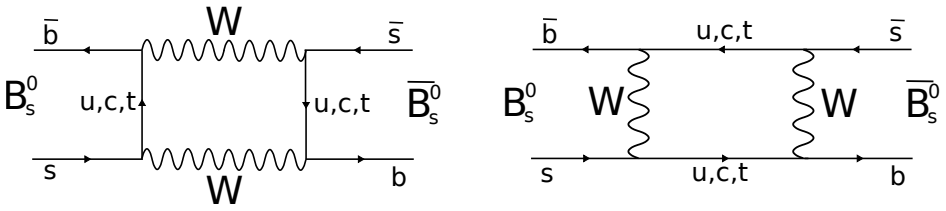

Figure 2.5: Feynman box diagrams responsible for mixing of B_s^0 mesons.

The time evolution of the wave function

$$|\psi(t)\rangle = a(t)|B_s^0\rangle + b(t)|\bar{B}_s^0\rangle. \tag{2.18}$$

is governed by the time dependent "Schrödinger-like" equation:

$$i\hbar\frac{\partial}{\partial t}\psi(t) = \mathbf{H}\psi(t). \tag{2.19}$$

A simplified 2×2 Hamiltonian $\mathbf{H}$ is composed of the mass and decay matrices $\mathbf{M}$ and $\mathbf{\Gamma}$ [21, 36, 42].

$$\mathbf{H} = \left(\mathbf{M} - \frac{i}{2}\mathbf{\Gamma}\right) = \begin{pmatrix} M_{11} & M_{12} \\ M_{12}^* & M_{22} \end{pmatrix} - \frac{i}{2}\begin{pmatrix} \Gamma_{11} & \Gamma_{12} \\ \Gamma_{12}^* & \Gamma_{22} \end{pmatrix} \tag{2.20}$$

The matrices $\mathbf{M}$ and $\mathbf{\Gamma}$ are hermitian. But as the mesons do oscillate and decay their combination in the Hamiltonian $\mathbf{H}$ is not hermitian [41]. Assuming CPT invariance, the diagonal elements of each matrix are the same: $M_{11} = M_{22} = M$ and $\Gamma_{11} = \Gamma_{22} = \Gamma$. The diagonal elements correspond to flavor conserving processes while the off-diagonal elements are associated with the flavor changing transitions of mixing.

Solving equation 2.19 by diagonalizing the matrix $\mathbf{H}$ leads to the mass eigenstates of the B_s system:

$$\begin{aligned} |B_L\rangle &\equiv p|B_s^0\rangle + q|\bar{B}_s^0\rangle \\ |B_H\rangle &\equiv p|B_s^0\rangle - q|\bar{B}_s^0\rangle \end{aligned} \tag{2.21}$$

with $\dfrac{q}{p} = \sqrt{\dfrac{M_{12}^* - \frac{i}{2}\Gamma_{12}^*}{M_{12} - \frac{i}{2}\Gamma_{12}}}$ and normalization $\sqrt{p^2+q^2} = 1$. The B_H denotes the heavy mass eigenstate and B_L the light one. The real and imaginary parts of their corresponding eigenvalues $\omega_{H,L}$ represent their masses and decay widths:

$$\omega_{H,L} = M - \frac{i}{2}\Gamma \pm \frac{q}{p}\left(M_{12} - \frac{i}{2}\Gamma_{12}\right). \tag{2.22}$$

The differences in mass and decay width of the heavy and light state are defined as

$$\begin{aligned} \Delta M &\equiv M_H - M_L = \Re(\omega_H - \omega_L) \\ \text{and} \qquad \Delta\Gamma &\equiv \Gamma_L - \Gamma_H = -2\Im(\omega_L - \omega_H). \end{aligned} \tag{2.23}$$

2.4.2 Time Evolution

The time evolution of the mass eigenstates is described by an exponential function depending on mass and decay width of the corresponding state:

$$\begin{aligned} |B_L(t)\rangle &= e^{-(iM_L - \frac{\Gamma_L}{2})t}|B_L(0)\rangle \\ |B_H(t)\rangle &= e^{-(iM_H - \frac{\Gamma_H}{2})t}|B_H(0)\rangle. \end{aligned} \tag{2.24}$$

Combining equations 2.21 and 2.24 yields the time evolution of the initially pure flavor eigenstates B_s^0 and $\bar{B}_s^0$

$$\begin{aligned} |B_s^0(t)\rangle &= g_+(t)|B_s^0\rangle - \frac{q}{p}g_-(t)|\bar{B}_s^0\rangle \\ |\bar{B}_s^0(t)\rangle &= g_+(t)|\bar{B}_s^0\rangle - \frac{p}{q}g_-(t)|B_s^0\rangle \end{aligned} \tag{2.25}$$

with

$$g_\pm(t) = \frac{1}{2}\left(e^{-iM_H t - \frac{1}{2}\Gamma_H t} \pm e^{-iM_L t - \frac{1}{2}\Gamma_L t}\right). \tag{2.26}$$

Instead of using the mass and decay width of the heavy and light states, the time evolution of neutral mesons is often expressed in terms of the mass difference, the decay width difference (see equation 2.23), the average mass $M = \frac{1}{2}(M_H + M_L)$ and the decay width $\Gamma = \frac{1}{2}(\Gamma_H + \Gamma_L)$:

$$g_\pm(t) = \frac{1}{2}e^{-iMt}e^{-\frac{1}{2}\Gamma t}\left(e^{-i\frac{\Delta M}{2}t + \frac{\Delta\Gamma}{4}t} \pm e^{i\frac{\Delta M}{2}t - \frac{\Delta\Gamma}{4}t}\right). \tag{2.27}$$

The amplitudes of the decay of B_s ($\bar{B}_s$) to the final state f ($\bar{f}$) via the weak interaction Hamiltonian $\mathcal{H}$ are defined as

$$\begin{aligned} A_f &= \langle f|\mathcal{H}|B_s\rangle, \qquad \bar{A}_f = \langle f|\mathcal{H}|\bar{B}_s\rangle, \\ A_{\bar{f}} &= \langle \bar{f}|\mathcal{H}|B_s\rangle, \qquad \bar{A}_{\bar{f}} = \langle \bar{f}|\mathcal{H}|\bar{B}_s\rangle. \end{aligned} \tag{2.28}$$

The time-dependent decay rates follow from equations 2.25 and 2.28:

$$\begin{aligned} d\Gamma(B_s(t) \to f)/dt = \mathcal{N}_f e^{-\Gamma t}[\ & (|A_f|^2 + |\frac{q}{p}\bar{A}_f|^2)\cosh\frac{\Delta\Gamma t}{2} \\ & +(|A_f|^2 - |\frac{q}{p}\bar{A}_f|^2)\cos\Delta M t \\ & -2\Re(\frac{q}{p}A_f^*\bar{A}_f)\sinh\frac{\Delta\Gamma t}{2} \\ & -2\Im(\frac{q}{p}A_f^*\bar{A}_f)\sin\Delta M t] \end{aligned} \tag{2.29}$$

$$\begin{aligned} d\Gamma(\bar{B}_s(t) \to f)/dt = \mathcal{N}_f e^{-\Gamma t}[\ & (\frac{p}{q}|A_f|^2 + |\bar{A}_f|^2)\cosh\frac{\Delta\Gamma t}{2} \\ & -(\frac{p}{q}|A_f|^2 - |\bar{A}_f|^2)\cos\Delta M t \\ & -2\Re(\frac{p}{q}A_f\bar{A}_f^*)\sinh\frac{\Delta\Gamma t}{2} \\ & -2\Im(\frac{q}{p}A_f\bar{A}_f^*)\sin\Delta M t] \end{aligned} \tag{2.30}$$

where $\mathcal{N}_f$ is a common, time-independent normalization factor. The parts of the decay rates that are proportional to $|A_f|^2$ or $|\bar{A}_f|^2$ correspond to direct decays without oscillation. The terms featuring amplitudes with a factor of $\frac{q}{p}$ or $\frac{p}{q}$ are associated with decays following a net oscillation. The parts containing $\sinh\frac{\Delta\Gamma t}{2}$ or $\sin\Delta M t$ terms are associated with interference between direct decays and decays following oscillations. The decay rates for the CP conjugate final state $\bar{f}$ are derived analogously with the substitutions $A_f \to A_{\bar{f}}$, $\bar{A}_f \to \bar{A}_{\bar{f}}$ and $\mathcal{N}_f = \mathcal{N}_{\bar{f}}$.

These general decay rates are valid for all neutral meson systems. The explicit differential decay rate for the analysis of the $B_s^0 \to J/\psi\phi$ decay will be discussed in section 2.5.2.

2.4.3 Types of CP Violation

Since physical observables do not depend on phase conventions, it is useful to define phase-independent quantities that are used to distinguish between three different CP violating effects in the decay of mesons, leading to three categories of CP violation. The classification has been developed for B decays but can be used for the decays of all mesons M [43].

CP violation in decay occurs when the decay amplitudes of $M \to f$ and $\bar{M} \to \bar{f}$ are different. It is also called direct CP violation and is defined by

$$|\frac{\bar{A}_{\bar{f}}}{A_f}| \neq 1.$$

This is the only possible CP violating effect in the decay of charged mesons.

CP violation in mixing occurs in the presence of an asymmetry in the particle antiparticle oscillations. It is also called indirect CP violation and is defined by

$$\frac{q}{p} \neq 1.$$

In this case the CP eigenstates are not equivalent to the mass eigenstates.

CP violation in interference of mixing and decay can only occur if M^0 and $\bar{M}^0$ decay into the same final state. The common final state is reached via two different decay chains: $M^0 \to f$ and $M^0 \to \bar{M}^0 \to f$. This CP violating effect is defined by

$$\Im(\lambda_f) \neq 0 \quad \text{with} \quad \lambda_f = \frac{q}{p}\frac{\bar{A}_f}{A_f}.$$

If the common final state is a pure CP eigenstate the time-dependent asymmetry can be written as

$$\mathcal{A}_{f_{CP}}(t) = \frac{d\Gamma(\bar{M}^0(t) \to f_{CP})/dt - d\Gamma(M^0(t) \to f_{CP})/dt}{d\Gamma(\bar{M}^0(t) \to f_{CP})/dt + d\Gamma(M^0(t) \to f_{CP})/dt}. \quad (2.31)$$

In the $B_s^0 \to J/\psi\phi$ channel the CP violating weak phase of the CKM matrix is suppressed by a factor of λ^2. It follows that in a good approximation there is no direct CP violation in the B_s^0 decay [44]. CP violation in $B_s^0 - \bar{B}_s^0$ mixing is a very small effect. Its Standard Model prediction is $|\frac{q}{p}| = 1 + \mathcal{O}(10^{-3})$ and an upper bound of $|\frac{q}{p}| = 1.0052 \pm 0.0032$ was measured in the charge asymmetry of semileptonic B_s decays [21]. Because oscillation between the initial states B_s^0 and $\bar{B}_s^0$ is possible and both decay into the common final state $J/\psi\phi$, CP violation in the $B_s^0 \to J/\psi\phi$ channel happens via interference of mixing and decay.

2.5 $B_s^0 \to J/\psi\phi$ Phenomenology

In this section the phenomenology specific to the $B_s^0 \to J/\psi\phi$ decay is discussed. First the physics parameters characterizing the decay process are introduced and defined. Since the final state $J/\psi\phi$ of the decay is an admixture of CP even and CP odd states, the states are separated via an angular analysis to study the CP violation. In section 2.5.2 the explicit decay rate used in the measurement is presented.

Due to the oscillation between B_s^0 and $\bar{B}_s^0$ and their subsequent decay to a common final state, CP violation in this channel occurs via interference of mixing and decay. Figure 2.6 shows a schematic of the interference of $B_s^0 - \bar{B}_s^0$ oscillation and the decay of both states to $J/\psi\phi$.

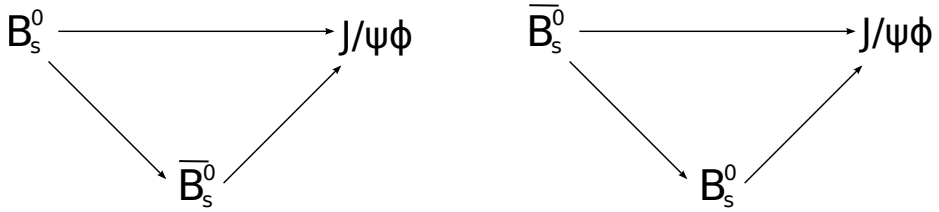

Figure 2.6: Interference between mixing and decay of B_s^0 and $\bar{B}_s^0$.

The $B_s^0 - \bar{B}_s^0$ oscillations described by the Hamiltonian in equation 2.20 involve three different physical quantities: M_{12}, Γ_{12} and the phase[2] $\phi_{12} = \arg(-M_{12}/\Gamma_{12})$ [23]. With the experimentally found relation $\Delta M \gg \Delta\Gamma$ that implies $|\Gamma_{12}| \ll |M_{12}|$ the eigenvalues (equation 2.22) and q/p can be expanded in Γ_{12}/M_{12} [45]:

$$\Delta M = M_H - M_L = 2|M_{12}|, \quad \Delta\Gamma = \Gamma_L - \Gamma_H = 2|\Gamma_{12}|\cos\phi_{12} \tag{2.32}$$

$$\text{and} \quad \frac{q}{p} = -e^{-i\phi_M}\left[1 - \frac{1}{2}\left|\frac{\Gamma_{12}}{M_{12}}\right|\sin\phi_{12}\right]. \tag{2.33}$$

ϕ_{12} is the CP violating phase in mixing. In the Standard Model it has a very small value of $\phi_{12} \approx 4.2 \cdot 10^{-3}$ [23] and thus the second term in equation

[2] In the literature, e.g. [23], ϕ_{12} is often denoted by ϕ_s. ϕ_{12} is used here to avoid confusion with the ϕ_s defined in 2.38, which is one of the key quantities of the measurement presented in this thesis.

2.34 can be neglected. The (not CP violating) mixing phase ϕ_M is given by $e^{-i\phi_M} = V_{ts}V_{tb}^*/V_{ts}^*V_{tb}$ and therefore

$$\frac{q}{p} = -e^{-i\phi_M} = -\frac{V_{ts}V_{tb}^*}{V_{ts}^*V_{tb}}. \tag{2.34}$$

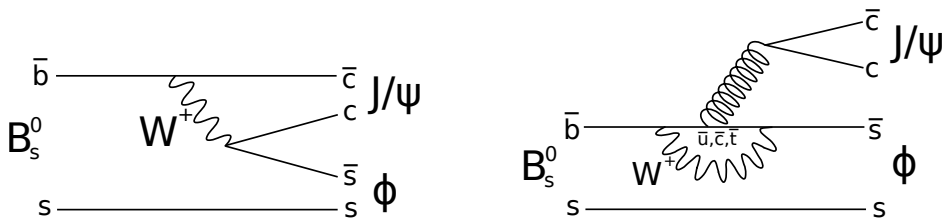

Figure 2.7: Tree (left) and penguin (right) Feynman diagrams contributing to the $B_s^0 \to J/\psi\phi$ decay in the Standard Model.

The tree level and penguin Feynman diagrams of the $\bar{b} \to \bar{c}c\bar{s}$ transition in the $B_s^0 \to J/\psi\phi$ decay are presented in figure 2.7. The same diagrams for the $\bar{B}_s^0$ decay can be derived by replacing all particles by their antiparticles. The total amplitude of the $\bar{b} \to \bar{c}c\bar{s}$ transition is a combination of tree (t_f) and penguin (p_f^q) diagrams:

$$\mathcal{A}_f = (V_{cb}^*V_{cs})\, t_f + \sum_{q=u,c,t} \left(V_{qb}^*V_{qs}\right) p_f^q, \tag{2.35}$$

where f denotes the final state $J/\psi\phi$. Making use of the CKM unitarity $V_{ub}^*V_{us} + V_{cb}^*V_{cs} + V_{tb}^*V_{ts} = 0$, this can be written as

$$\mathcal{A}_f = (V_{cb}^*V_{cs})\,(t_f + p_f^c - p_f^t) + (V_{ub}^*V_{us})\,(p_f^u - p_f^t). \tag{2.36}$$

Because $V_{cb}^*V_{cs} \approx A\lambda^2(1-\lambda^2)$ and $V_{ub}^*V_{us} \approx A\lambda^4(\rho + i\eta)$, the $(p_f^u - p_f^t)$ term is suppressed by a factor of λ^2 relative to the first term. Neglecting the second term, the ratio of decay amplitudes is given by [45]

$$\frac{\bar{\mathcal{A}}_f}{\mathcal{A}_f} = -\eta_f^{CP}\frac{V_{cb}V_{cs}^*}{V_{cb}^*V_{cs}} \tag{2.37}$$

with $\eta_f^{CP} = \pm 1$ for the CP even and CP odd final states. In combination with equation 2.34, CP violation in the interference of mixing and decay of $B_s^0 \to J/\psi\phi$ is described by

$$\lambda_{J/\psi\phi} = \eta^{CP}_{J/\psi\phi} e^{-i\phi_s} \approx \eta^{CP}_{J/\psi\phi} \frac{V_{ts}V_{tb}^*}{V_{ts}^*V_{tb}} \frac{V_{cs}^*V_{cb}}{V_{cs}V_{cb}^*} = \eta^{CP}_{J/\psi\phi} e^{i2\beta_s}. \tag{2.38}$$

The size of the phase ϕ_s determines the amount of CP violation in the $B_s^0 \to J/\psi\phi$ decay. Neglecting a small penguin pollution, it is related to the small angle of the B_s unitarity triangle (figure 2.3) via the relation $\phi_s \approx -2\beta_s$. The Standard Model prediction for ϕ_s is [22]

$$\phi_s = -0.037 \pm 0.002\,\text{rad}. \tag{2.39}$$

New Physics in B_s^0 Mixing

A sizable deviation from this value would be a clear sign of beyond Standard Model physics. The New Physics processes could introduce additional contributions to the box diagrams describing the B_s^0 mixing and alter the off-diagonal matrix elements M_{12} in the Hamiltonian in equation 2.20. Examples of New Physics models affecting B_s^0 mixing can be found in [46] and [47]. A CP violating New Physics phase ϕ^{NP} would contribute to ϕ_s and ϕ_{12} in the same way: $\phi_s = \phi_s^{SM} + \phi^{NP}$ and $\phi_{12} = \phi_{12}^{SM} + \phi^{NP}$. Since both their Standard Model values are small, the New Physics phase would dominate both quantities and the approximation $\phi_s \approx \phi_{12}$ would be valid [48].

2.5.1 Angular Analysis in the Transversity Basis

In section 2.5 it was shown that indirect CP violation is negligible in $B_s^0 \to J/\psi\phi$ and thus the mass eigenstates are assumed to be equal to the CP eigenstates. Following the definition in equation 2.21, the heavy mass eigenstate B_H is CP odd and the light mass eigenstate B_L is CP even.

In the decay $B_s^0 \to J/\psi\phi$ a pseudoscalar decays into a final state composed of two vector mesons. The pseudoscalar B_s^0 has a spin of 0 and the vector particles J/ψ and ϕ each have spin 1. Due to conservation of total angular momentum, a relative orbital angular momentum l between the two vector mesons arises which can have the values $l = 0, 1, 2$. These different values of relative orbital angular momentum lead to different CP values of the final state.

$$\eta^{CP}_{J/\psi\phi} = \eta^{CP}_{J/\psi}\eta^{CP}_{\phi}(-1)^l = (-1)^l.$$

The J/ψ and ϕ are both CP even ($J^{PC}(J/\psi) = 1^{--}$, $J^{PC}(\phi) = 1^{--}$) and therefore the CP of the final state is determined by l resulting in an admixture

of CP even ($l = 0,\ 2$) and CP odd ($l = 1$) states. An angular analysis is used to statistically disentangle the CP even and CP odd portions of the final state [45, 49].

To achieve the separation of the CP states, the transversity basis is chosen. Three transversity amplitudes, A_0, $A_\parallel$ and $A_\perp$, describe the relative linear polarizations of the vector particles and are related to the CP even and odd final states. For A_0 the spins of the vector particles are polarized longitudinally with respect to their momentum, for $A_\parallel$ and $A_\perp$ the spins are polarized transversely with respect to their momentum. The spins are parallel to each other for $A_\parallel$ and perpendicular to each other for $A_\perp$. While $A_\perp$ represents the CP odd state, a linear combination of A_0 and $A_\parallel$ corresponds to the CP even states.
In this thesis the decay of $B_s^0 \to J/\psi\phi$ where the J/ψ decays to $\mu^+\mu^-$ and the ϕ decays to K^+K^- is analyzed. The transversity basis defines a set of three angles between the relative motion of the two muons and two kaons to describe the angular distribution of the final state that is shown in figure 2.8.

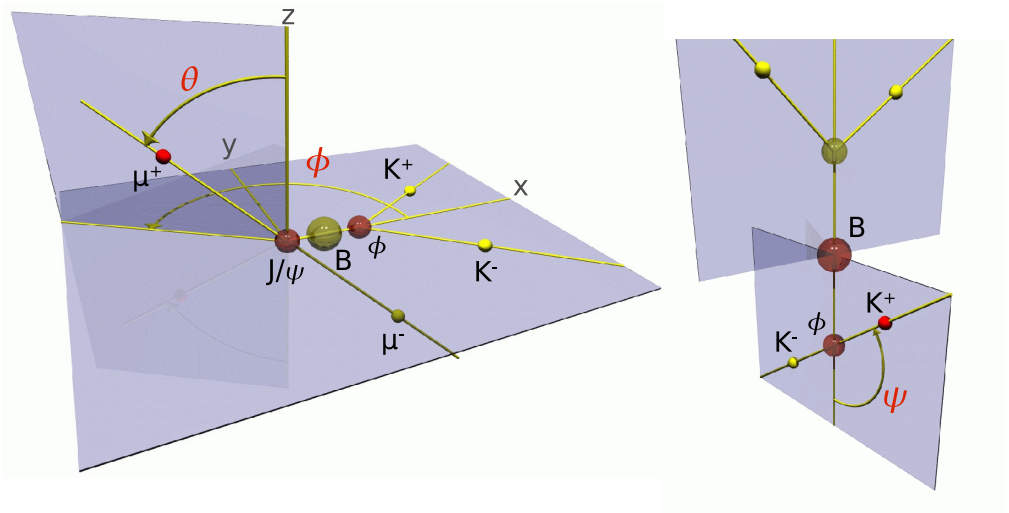

Figure 2.8: Transversity basis defined in terms of three angles between the final state particles. The angles θ and ϕ are defined in the J/ψ meson rest frame and the angle ψ is defined in the ϕ rest frame.

The three transversity angles are defined in the rest frames of the J/ψ and ϕ particles. The positive x axis is assigned to the direction of the ϕ in the J/ψ rest frame and the xy plane is defined by the K^+ and K^- momenta, where the direction of the K^+ corresponds to the positive y axis. Using this coordinate system the angles are defined as:

- θ is the angle between the momentum of the positively charge muon and the xy plane in the J/ψ rest frame.
- ϕ is the angle between the x axis and the projection of the positively charged muon momentum onto the xy plane in the J/ψ rest frame.
- ψ is the angle between the K^+ momentum and the negative flight direction of the J/ψ in the ϕ rest frame.

Using the definition of the coordinate system and the transversity angles, the unit vector of the μ^+ momentum is

$$\hat{n} = (\sin\theta\cos\phi,\ \sin\theta\sin\phi,\ \cos\theta). \tag{2.40}$$

Each of the transversity amplitudes has an associated phase: $\delta_0 = \arg A_0$, $\delta_\parallel = \arg A_\parallel$ and $\delta_\perp = \arg A_\perp$. Since only phase differences between the amplitudes appear in the differential decay rate (section 2.5.2), one phase can conveniently be set to zero: $\delta_0 = 0$.

2.5.2 Time-Dependent Decay Rate

The derivation of the differential decay rate can be found in [49,50]. The probability density of B_s^0 and $\bar{B}_s^0$ is defined by

$$\begin{aligned} P_B(\theta,\phi,\psi,t) &= \frac{9}{16\pi}\left|\mathbf{A}(t)\times\hat{n}\right|^2 \\ \text{and}\qquad P_{\bar{B}}(\theta,\phi,\psi,t) &= \frac{9}{16\pi}\left|\bar{\mathbf{A}}(t)\times\hat{n}\right|^2 \end{aligned} \tag{2.41}$$

where $\hat{n}$ is the unit vector defined by θ and ϕ (see equation 2.40). The dependence on the remaining angle ψ is contained in the complex amplitude vectors $\mathbf{A}$ and $\bar{\mathbf{A}}$:

$$\begin{aligned} \mathbf{A}(t) &= \left(A_0(t)\cos\psi,\ -\frac{A_\parallel(t)\sin\psi}{\sqrt{2}}, i\frac{A_\perp(t)\sin\psi}{\sqrt{2}}\right), \\ \bar{\mathbf{A}}(t) &= \left(\bar{A}_0(t)\cos\psi,\ -\frac{\bar{A}_\parallel(t)\sin\psi}{\sqrt{2}},\ i\frac{\bar{A}_\perp(t)\sin\psi}{\sqrt{2}}\right). \end{aligned} \tag{2.42}$$

The probability densities of B_s^0 and $\bar{B}_s^0$ are normalized to one:

$$\iiint \sum_{k=B,\bar{B}} P_k(\theta,\phi,\psi,t)\,d(\cos\theta)\,d(\cos\psi)\,d\phi\,dt = 1. \tag{2.43}$$

The time-dependent amplitudes of the transition of an initial B_s^0 or $\bar{B}_s^0$ into the final state f_i can be defined as

$$\begin{aligned} A_i(t) &= \langle f_i|H|B_s^0\rangle\langle B_s^0|B_{s,phys}^0(t)\rangle + \langle f_i|H|\bar{B}_s^0\rangle\langle \bar{B}_s^0|B_{s,phys}^0(t)\rangle \\ \bar{A}_i(t) &= \langle f_i|H|B_s^0\rangle\langle B_s^0|\bar{B}_{s,phys}^0(t)\rangle + \langle f_i|H|\bar{B}_s^0\rangle\langle \bar{B}_s^0|\bar{B}_{s,phys}^0(t)\rangle. \end{aligned} \tag{2.44}$$

$B_{s,phys}^0(t)$ and $\bar{B}_{s,phys}^0(t)$ denote an initially pure B_s^0 or $\bar{B}_s^0$ after a proper time t has elapsed and thus are superpositions of mixed and unmixed states. The final state $\mu^+\mu^-K^+K^-$ is characterized by the transversity angles and the time-dependent transversity amplitudes $A_i(t)$ and $\bar{A}_i(t)$ can be explicitly expressed as [50]

$$\begin{aligned} A_i(t) =& \frac{e^{-imt}e^{-\Gamma t/2}}{\sqrt{\tau_H+\tau_L \pm \cos\phi_s(\tau_L-\tau_H)}}\left[E_+(t) \pm e^{-i\phi_s}E_-(t)\right]A_i(t=0) \\ \bar{A}_i(t) =& \frac{e^{-imt}e^{-\Gamma t/2}}{\sqrt{\tau_H+\tau_L \pm \cos\phi_s(\tau_L-\tau_H)}}\left[\pm E_+(t) + e^{i\phi_s}E_-(t)\right]A_i(t=0) \end{aligned} \tag{2.45}$$

with

$$E_\pm(t) = \frac{1}{2}\left[e^{+\left(\frac{\Delta\Gamma}{4}+i\frac{\Delta M}{2}\right)t} \pm e^{-\left(\frac{\Delta\Gamma}{4}+i\frac{\Delta M}{2}\right)t}\right]. \tag{2.46}$$

These time-dependent amplitudes can now be used with the probability densities defined in equation 2.41. When fitting the rate of the B_s^0 decay, each time-dependent term must be convolved with a Gaussian smearing function to account for the limited detector resolution. This is necessary as the decay length of the B_s^0 mesons is of the same order as the detector resolution of the vertex detector [50] used in the experiment. The convolution can be carried out analytically but the challenging calculation can be simplified by expanding the probabilities in terms of separate decay rates of CP even and CP odd terms. The CP even amplitudes, $A_0(t)$ and $A_\parallel(t)$, have identical time evolution, but different from the one of the CP odd amplitude $A_\perp(t)$.

Because of this the time-dependent amplitude vectors $\mathbf{A}$ and $\bar{\mathbf{A}}$ (see equation 2.42) are decomposed into CP even (+) and CP odd (-) components.

$$\mathbf{A}(t) = \mathbf{A}_+(t) + \mathbf{A}_-(t), \quad \bar{\mathbf{A}}(t) = \bar{\mathbf{A}}_+(t) + \bar{\mathbf{A}}_-(t). \tag{2.47}$$

In the CP even and CP odd amplitudes the time dependence is separated and the remaining term contains only the amplitudes at $t = 0$.

$$\begin{aligned}
\mathbf{A}_+(t) &= \mathbf{A}_+ f_+(t) = (A_0 \cos\psi,\ -\frac{A_\parallel \sin\psi}{\sqrt{2}},\ 0) \cdot f_+(t) \\
\bar{\mathbf{A}}_+(t) &= \bar{\mathbf{A}}_+ \bar{f}_+(t) = (A_0 \cos\psi,\ -\frac{A_\parallel \sin\psi}{\sqrt{2}},\ 0) \cdot \bar{f}_+(t) \\
\mathbf{A}_-(t) &= \mathbf{A}_- f_-(t) = (0,\ 0,\ i\frac{a_\perp \sin\psi}{\sqrt{2}}) \cdot f_-(t) \\
\bar{\mathbf{A}}_-(t) &= \bar{\mathbf{A}}_- \bar{f}_-(t) = (0,\ 0,\ i\frac{a_\perp \sin\psi}{\sqrt{2}}) \cdot \bar{f}_-(t)
\end{aligned} \tag{2.48}$$

where

$$\begin{aligned}
f_\pm =& \frac{e^{-\Gamma t/2}}{\sqrt{\tau_H + \tau_L \pm \cos\phi_s(\tau_L - \tau_H)}} \left[E_+(t) \pm e^{-i\phi_s} E_-(t)\right] \\
\bar{f}_\pm =& \frac{e^{-\Gamma t/2}}{\sqrt{\tau_H + \tau_L \pm \cos\phi_s(\tau_L - \tau_H)}} \left[\pm E_+(t) + e^{i\phi_s} E_-(t)\right].
\end{aligned} \tag{2.49}$$

Equation 2.41 can then be written as

$$\begin{aligned}
P_B(\theta,\psi,\phi,t) =& \frac{9}{16\pi}\{|\mathbf{A}_+(t) \times \hat{n}|^2 + |\mathbf{A}_-(t) \times \hat{n}|^2 + 2\Re((\mathbf{A}_+(t) \times \hat{n}) \cdot (\mathbf{A}_-^*(t) \times \hat{n}))\} \\
=& \frac{9}{16\pi}\{|\mathbf{A}_+ \times \hat{n}|^2 |f_+(t)|^2 + |\mathbf{A}_- \times \hat{n}|^2 |f_-(t)|^2 \\
&+ 2\Re((\mathbf{A}_+ \times \hat{n}) \cdot (\mathbf{A}_-^* \times \hat{n}) f_+(t) \cdot f_-^*(t))\}
\end{aligned} \tag{2.50}$$

and

$$
\begin{aligned}
P_{\bar{B}}(\theta,\psi,\phi,t) =& \frac{9}{16\pi}\{|\bar{\mathbf{A}}_+(t)\times\hat{n}|^2 + |\bar{\mathbf{A}}_-(t)\times\hat{n}|^2 + 2\Re((\bar{\mathbf{A}}_+(t)\times\hat{n})\cdot(\bar{\mathbf{A}}_-^*(t)\times\hat{n}))\} \\
=& \frac{9}{16\pi}\{|\mathbf{A}_+\times\hat{n}|^2|\bar{f}_+(t)|^2 + |\mathbf{A}_-\times\hat{n}|^2|\bar{f}_-(t)|^2 \\
&+2\Re((\mathbf{A}_+\times\hat{n})\cdot(\mathbf{A}_-^*\times\hat{n})\bar{f}_+(t)\cdot\bar{f}_-^*(t))\}.
\end{aligned}
\tag{2.51}
$$

The diagonal time-dependent terms are

$$
\begin{aligned}
|f_\pm(t)|^2 =& \frac{1}{2}\frac{(1\pm\cos\phi_s)e^{-\Gamma_L t} + (1\mp\cos\phi_s)e^{-\Gamma_H t} \pm 2\sin\phi_s e^{-\Gamma t}\sin\Delta M}{\tau_L(1\pm\cos\phi_s)+\tau_H(1\mp\cos\phi_s)} \\
|\bar{f}_\pm(t)|^2 =& \frac{1}{2}\frac{(1\pm\cos\phi_s)e^{-\Gamma_L t} + (1\mp\cos\phi_s)e^{-\Gamma_H t} \mp 2\sin\phi_s e^{-\Gamma t}\sin\Delta M}{\tau_L(1\pm\cos\phi_s)+\tau_H(1\mp\cos\phi_s)}
\end{aligned}
\tag{2.52}
$$

and the interference terms are

$$
\begin{aligned}
f_+(t)f_-^*(t) =& \frac{e^{-\Gamma t}\cos\Delta M t + i\cos\phi_s e^{-\Gamma t}\sin\Delta M t + i\sin\phi_s(e^{-\Gamma_H t}-e^{-\Gamma_L t})/2}{\sqrt{[(\tau_H-\tau_L)\sin\phi_s]^2 + 4\tau_L\tau_H}} \\
\bar{f}_+(t)\bar{f}_-^*(t) =& \frac{-e^{-\Gamma t}\cos\Delta M t - i\cos\phi_s e^{-\Gamma t}\sin\Delta M t + i\sin\phi_s(e^{-\Gamma_H t}-e^{-\Gamma_L t})/2}{\sqrt{[(\tau_H-\tau_L)\sin\phi_s]^2 + 4\tau_L\tau_H}}.
\end{aligned}
\tag{2.53}
$$

The separated terms of the decay rate can be used in a likelihood fitting function as it is done for the measurement presented in this thesis. To take the proper time resolution of the measurement with the detector into account, the time-dependent terms are convolved with a Gaussian function of the proper time resolution. The complete time- and angle-dependent differential decay rate of the $B_s^0 \to J/\psi\phi$ decay are summarized in the expression

$$
\frac{d\Gamma}{dt\,d\Omega} = \sum_{k=1}^{10} h^k(t)g^k(\theta,\psi,\phi) \tag{2.54}
$$

where Ω denotes the transversity angles. Terms one to six describe the signal decay, while term seven to ten describe the S-wave terms that are discussed

in section 2.5.3. The terms depending on the transversity angles $g^k(\theta, \psi, \phi)$ are presented in table 2.3. The time-dependent terms $h^k(t)$ are explicitly defined in equations 2.55 to 2.64:

$$\begin{aligned} h^{(1)}(t) =& \frac{1}{2}|A_0(0)|^2 \Big[(1+\cos\phi_s)\, e^{-\Gamma_L t} + (1-\cos\phi_s)\, e^{-\Gamma_H t} \\ & \pm 2e^{-\Gamma_s t} \sin(\Delta m_s t) \sin\phi_s \Big] \end{aligned} \tag{2.55}$$

$$\begin{aligned} h^{(2)}(t) =& \frac{1}{2}|A_\parallel(0)|^2 \Big[(1+\cos\phi_s)\, e^{-\Gamma_L t} + (1-\cos\phi_s)\, e^{-\Gamma_H t} \\ & \pm 2e^{-\Gamma_s t} \sin(\Delta m_s t) \sin\phi_s \Big] \end{aligned} \tag{2.56}$$

$$\begin{aligned} h^{(3)}(t) =& \frac{1}{2}|A_\perp(0)|^2 \Big[(1-\cos\phi_s)\, e^{-\Gamma_L t} + (1+\cos\phi_s)\, e^{-\Gamma_H t} \\ & \mp 2e^{-\Gamma_s t} \sin(\Delta m_s t) \sin\phi_s \Big] \end{aligned} \tag{2.57}$$

$$\begin{aligned} h^{(4)}(t) =& \frac{1}{2}|A_0(0)||A_\parallel(0)| \cos\delta_{||} \Big[(1+\cos\phi_s)\, e^{-\Gamma_L t} \\ & + (1-\cos\phi_s)\, e^{-\Gamma_H t} \pm 2e^{-\Gamma_s t} \sin(\Delta m_s t) \sin\phi_s \Big] \end{aligned} \tag{2.58}$$

$$\begin{aligned} h^{(5)}(t) =& |A_\parallel(0)||A_\perp(0)| \Big[\frac{1}{2}(e^{-\Gamma_L t} - e^{-\Gamma_H t}) \cos(\delta_\perp - \delta_{||}) \sin\phi_s \\ & \pm e^{-\Gamma_s t} (\sin(\delta_\perp - \delta_\parallel) \cos(\Delta m_s t) - \cos(\delta_\perp - \delta_\parallel) \cos\phi_s \sin(\Delta m_s t)) \Big] \end{aligned} \tag{2.59}$$

$$\begin{aligned} h^{(6)}(t) =& |A_0(0)||A_\perp(0)| \Big[\frac{1}{2}(e^{-\Gamma_L t} - e^{-\Gamma_H t}) \cos\delta_\perp \sin\phi_s \\ & \pm e^{-\Gamma_s t} (\sin\delta_\perp \cos(\Delta m_s t) - \cos\delta_\perp \cos\phi_s \sin(\Delta m_s t)) \Big] \end{aligned} \tag{2.60}$$

$$\begin{aligned} h^{(7)}(t) =& \frac{1}{2}|A_S(0)|^2 \Big[(1-\cos\phi_s)\, e^{-\Gamma_L t} + (1+\cos\phi_s)\, e^{-\Gamma_H t} \\ & \mp 2e^{-\Gamma_s t} \sin(\Delta m_s t) \sin\phi_s \Big] \end{aligned} \tag{2.61}$$

$$\begin{aligned} h^{(8)}(t) =& |A_S||A_\parallel(0)| \Big[\frac{1}{2}(e^{-\Gamma_L t} - e^{-\Gamma_H t}) \sin(\delta_\parallel - \delta_S) \sin\phi_s \\ & \pm e^{-\Gamma_s t} (\cos(\delta_\parallel - \delta_S) \cos(\Delta m_s t) - \sin(\delta_\parallel - \delta_S) \cos\phi_s \sin(\Delta m_s t)) \Big] \end{aligned} \tag{2.62}$$

$$\begin{aligned} h^{(9)}(t) =& \frac{1}{2}|A_S||A_\perp(0)| \sin(\delta_\perp - \delta_S) \Big[(1-\cos\phi_s)\, e^{-\Gamma_L t} \\ & + (1+\cos\phi_s)\, e^{-\Gamma_H t} \mp 2e^{-\Gamma_s t} \sin(\Delta m_s t) \sin\phi_s \Big] \end{aligned} \tag{2.63}$$

$$h^{(10)}(t) = |A_0(0)||A_S(0)|\Big[\frac{1}{2}(e^{-\Gamma_H t} - e^{-\Gamma_L t})\sin\delta_S \sin\phi_s \pm e^{-\Gamma_s t}(\cos\delta_S\cos(\Delta m_s t) + \sin\delta_S\cos\phi_s\sin(\Delta m_s t))\Big]. \tag{2.64}$$

Table 2.3: Table showing the angular component $g^{(k)}(\theta,\psi,\phi)$ of the decay rate depending on the transversity angles. Terms 1 - 6 correspond to the signal decay $B_s^0 \to J/\psi\phi$ and terms 7 - 10 correspond to the S-wave decays $B_s^0 \to J/\psi f_0$ and non-resonant $B_s^0 \to J/\psi K^+K^-$.

k	$g^{(k)}(\theta,\psi,\phi)$
1	$2\cos^2\psi(1-\sin^2\theta\cos^2\phi)$
2	$\sin^2\psi(1-\sin^2\theta\sin^2\phi)$
3	$\sin^2\psi\sin^2\theta$
4	$-\frac{1}{\sqrt{2}}\sin 2\psi\sin^2\theta\sin 2\phi$
5	$\sin^2\psi\sin 2\theta\sin\phi$
6	$\frac{1}{\sqrt{2}}\sin 2\psi\sin 2\theta\cos\phi$
7	$\frac{2}{3}(1-\sin\theta\cos^2\phi)$
8	$\frac{1}{3}\sqrt{6}\sin\psi\sin^2\theta\sin 2\phi$
9	$\frac{1}{3}\sqrt{6}\sin\psi\sin 2\theta\cos\phi$
10	$\frac{4}{3}\sqrt{3}\cos\psi\left(1-\sin^2\theta\cos^2\phi\right)$

In equations 2.55 to 2.64, the upper sign is valid for mesons that were initially a B_s^0 and the lower sign describes the decay of mesons that were initially a $\bar{B}_s^0$. Determining if the initial meson was a particle or antiparticle is referred to as initial state flavor tagging and will be discussed in section 2.6. In this thesis the results of an untagged (chapter 7) as well as a tagged analysis (chapter 8) of $B_s^0 \to J/\psi\phi$ are presented. In case of a tagged analysis, the decay rate for an initial B_s^0 ($\bar{B}_s^0$) is multiplied by the corresponding probability derived from flavor tagging. If no flavor tagging information is available, equal probabilities (0.5) are assumed for particle and antiparticle, which has the effect that all terms containing Δm_s in the equations for $h^k(t)$ are canceled out. In the case of an untagged analysis a simplified version of the time-dependent decay rate can be used by removing the terms containing Δm_s. Consequently the equations are identical for particle and antiparticle. Since the terms containing Δm_s also contain $\sin\phi_s$ or $\cos\phi_s$, a tagged analysis provides higher sensitivity to the measurement of ϕ_s resulting in a higher precision. The information loss due to removing the terms in an untagged analysis of the same data, results in a higher uncertainty of the ϕ_s measurement. The simplified version for the untagged analysis can be found in appendix A.1.

2.5.3 S-Wave Contribution

The data sample for the analysis of the $B_s^0 \to J/\psi\phi$ decay contains an additional contribution from the decay $B_s^0 \to J/\psi f_0$ and from the non-resonant $B_s^0 \to J/\psi K^+K^-$ decay. Both decays reach the same final state $\mu^+\mu^-K^+K^-$ as the signal decay and cannot be identified and removed from the data sample. The $B_s^0 \to J/\psi\phi$ signal could be contaminated with this S-wave contribution by up to 10 % [51]. The effect of this level of contamination of the signal with S-wave K^+K^- was studied in [52] with the result that it could significantly bias the ϕ_s measurement towards zero which approximately coincides with the Standard Model value. To avoid possible bias from the S-wave contribution, the decays of $B_s^0 \to J/\psi f_0$ and non-resonant $B_s^0 \to J/\psi K^+K^-$ are combined with the $B_s^0 \to J/\psi\phi$ decay rate and included in the fit.

Due to resulting in a CP odd final state, the S-wave decays have the same time dependence as the CP odd portion of the signal decay. The modified decay rate for the measurement including the S-wave contamination are derived in [50]. The S-wave decays correspond to the terms seven to ten in the differential decay rate (equation 2.54) where the explicit time-dependent terms $h^k(t)$ are presented in equations 2.61 to 2.64 and the angle dependent terms $g^{(k)}(\theta, \psi, \phi)$ are shown in table 2.3.

2.6 Flavor Tagging Principles

Including information about the initial flavor of the B_s meson at production in the $B_s^0 \to J/\psi\phi$ analysis, increases the sensitivity to the CP violating phase ϕ_s. In general, knowledge of the initial flavor can improve any CP violation measurement of B mesons. Because there is no oscillation between charged B mesons, their production flavor can be easily inferred from the decay products. However, due to the oscillation in neutral B meson systems, the decay products are typically not helpful to identify the production flavor. Determining whether the initial B meson was a particle or antiparticle is referred to as initial state flavor tagging, usually just called flavor tagging. The methods to work out the production flavor of a signal decay are divided into two categories: same side taggers and opposite side taggers. All flavor tagging techniques exploit the physical processes related to the production of the signal meson and thus it is important to understand the production mechanism of B mesons in the experiment.

At the LHC (chapter 3) B mesons (and baryons) are produced in the

hadronization of $b\bar{b}$ quark pairs. In proton - proton colliders, like LHC, $b\bar{b}$ pairs are principally produced via QCD interaction. The main production mechanisms are [53]:

- **Flavor creation** refers to the lowest order of $b\bar{b}$ production mechanisms and summarizes two processes. In the first case two gluons of the colliding protons interact via hard QCD scattering and produce the $b\bar{b}$ pair. The other possibility is the annihilation of a quark and a sea antiquark of the same flavor. The Feynman diagrams of these processes can be seen in 2.9.
- **Gluon splitting** means the production of a $b\bar{b}$ pair in the splitting of a gluon after a hard scattering process. The process is illustrated in the left diagram of figure 2.10.
- **Flavor excitation** occurs when a b type sea quark from the parton distribution of one beam particle interacts via hard scattering with a parton of the other beam. This is shown in the right diagram of figure 2.10 for a gluon. The b type sea quark arises from a $g \to b\bar{b}$ branching.

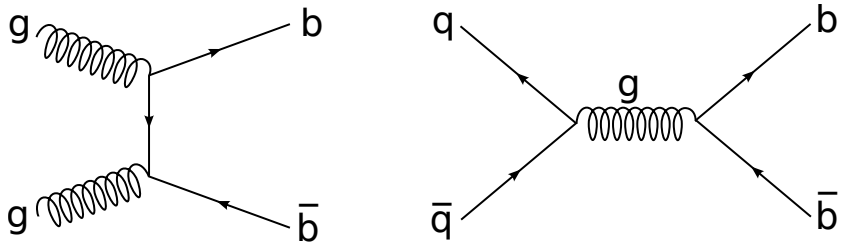

Figure 2.9: Lowest order Feynman diagrams of $b\bar{b}$ production via flavor creation. Gluon fusion is illustrated in the left diagram, and the right diagram shows $q\bar{q}$ annihilation.

Due to the large energies at the LHC and as a consequence of the three production mechanisms, the majority of $b\bar{b}$ quark pairs are produced either both in the forward or both in the backward direction of the detector. This is illustrated in the left plot of figure 2.11 that shows the angle θ of the b quark versus the θ of the $\bar{b}$ quark. θ is the polar angle of the particle direction from the beam axis and thus θ values close to zero (π) correspond to the forward (backward) direction. This also means that the transverse momenta of the produced b and $\bar{b}$ quark are relatively low in comparison to the collision energy.

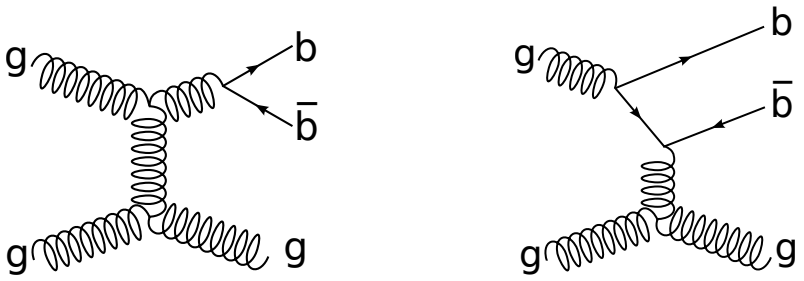

Figure 2.10: Lowest order Feynman diagrams of $b\bar{b}$ production via gluon splitting (left) and flavor excitation (right).

After the production of the $b\bar{b}$ pair, the two quarks hadronize and form B mesons. As each b quark needs a partner quark from the vacuum to make a meson, a cascade of additional lighter mesons are a byproduct of the hadronization process.

Thus the signal B meson is produced together with another B hadron that contains a b quark of the opposite flavor. This other B hadron is referred to as opposite side B hadron, and tagging methods that make use of its properties are called opposite side taggers. The decay products, as well as the additional particles produced in the hadronization of the opposite side hadron, can be used to infer the flavor of the signal particle. An opposite side flavor tagging method uses e.g. a semileptonic decay on the opposite side and the flavor is derived from the charge of the lepton. The same side taggers, on the other hand, make use of the particles that are produced in the hadronization of the signal B meson. In the case of a B_s^0 signal, a kaon is usually produced in the hadronization and its charge can be used to determine the B_s^0 flavor. Figure 2.12 illustrates the mechanics of opposite side and same side flavor tagging.

In the analysis presented in this thesis, two opposite side tagging methods are applied, and they are discussed in detail in chapter 8.

2.7 Lifetime and $\Delta\Gamma_s$ Measurement

In addition to the CP violating phase ϕ_s, the $B_s^0 \to J/\psi\phi$ analysis also provides a measurement of the average decay width Γ_s and the decay width difference $\Delta\Gamma_s$ between the heavy and the light B_s meson. The decay width is related to the lifetime with $\Gamma = \frac{1}{\tau}$. The B_s^0 meson has a rather long lifetime

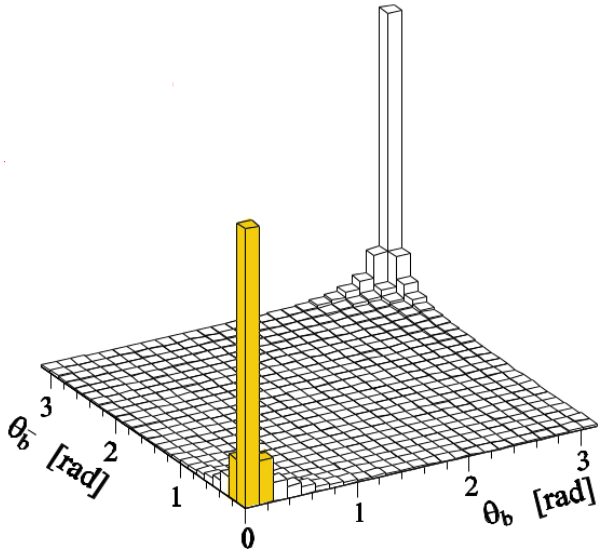

Figure 2.11: Two-dimensional θ distribution of the $b\bar{b}$ quark pairs created in the simulation of LHC collisions using the event generator *Pythia* [54]. The majority of $b\bar{b}$ quark pairs have either both a very low θ close to zero or a very high θ close to π.

of $\sim 1.5\,\mathrm{ps}$, which is caused by the b-quark. The bottom quark cannot decay into the much heavier top quark and is therefore forced to decay into a quark of a different generation. But in the CKM matrix the generation changing decays of the b-quark are suppressed by at least a factor of λ^2 (see equation 2.7).
In this analysis the lifetime *tau* is determined from a fit, which uses the proper lifetime calculated of each individual B_s^0 meson reconstructed with the ATLAS detector. The proper lifetime of a B_s^0 candidate is defined as

$$t = \frac{L}{\beta\gamma c} \tag{2.65}$$

where L is the B mesons decay length, $\beta = \frac{v}{c}$ the ratio of its velocity v to the speed of light c and γ the Lorentz factor. The decay length L of the B meson is the distance between its production vertex and its decay vertex. While the coordinates of the decay vertex are determined from the tracks of the decay products $\mu^+\mu^-K^+K^-$, the position of the primary vertex is determined from other tracks in the event. Using the momentum $p = \beta\gamma c M_{B_s}$ the proper

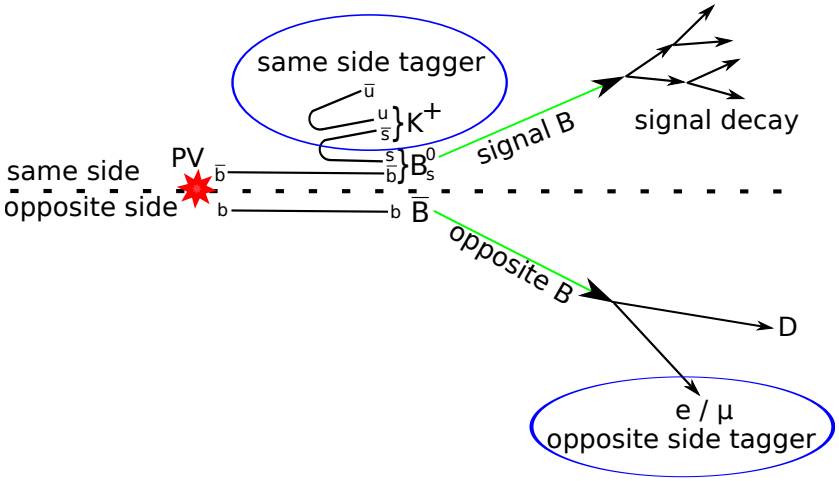

Figure 2.12: Illustration of same side kaon and opposite side lepton taggers.

decay time becomes

$$t = \frac{L\ M_{B_s}}{p}. \tag{2.66}$$

As the tracking detectors of ATLAS do not measure the momentum of the particles but the transverse momentum, because they are embedded into a magnetic field parallel to the beam direction, the proper lifetime of the B_s mesons is calculated as

$$t = \frac{L_{xy}\ M_{B_s}}{p_{T_B}} \tag{2.67}$$

where p_{T_B} is the transverse momentum of the B_s^0 meson and M_{B_s} is the world average value of its mass: $M_{B_s} = 5.3668\,\text{GeV}$ [21]. L_{xy} is the projection of the decay length into the transverse plane.
In contrast to ϕ_s the observable $\Delta\Gamma_s$ is not expected to be significantly affected by beyond Standard Model processes [23]. However, the $\Delta\Gamma_s$ measurement can test the Standard Model that predicts a value of $\Delta\Gamma_s = 0.087 \pm 0.021\,\text{ps}^{-1}$ [55]. It is also useful since it gives constraints on the ratio $\Delta\Gamma_s/\Delta M_s$ which has very small theoretical uncertainties as hadronic quantities appear only in sub-dominant terms in the calculation [23].

2.8 Review of Current Experimental Status

An analysis of the $B_s^0 \to J/\psi\phi$ channel has been performed by both Tevatron experiments CDF and D0. At the LHC, measurements with this

channel were performed by ATLAS, CMS and LHCb, but CMS did not measure ϕ_s. All analysis groups found $\Delta\Gamma_s$ values consistent with the Standard Model and, if measured, the observed ϕ_s value was also in agreement with the Standard Model expectation. The results of the ATLAS measurements are the topic of this thesis and will be presented in chapter 7 and 8. The latest results of the other four experiments are summarized in table 2.4.

CDF has published the results of a tagged analysis with the full data set [56] collected at the Tevatron, corresponding to an integrated luminosity of $9.6\,\text{fb}^{-1}$. An artificial neural network is used to discriminate $\sim 11\,000$ signal decays from the background, and the average lifetime and the decay width difference are measured with ϕ_s fixed to the Standard Model value.
The final result of the tagged analysis from the D0 collaboration using $8.0\,\text{fb}^{-1}$ is reported in [57]. A multivariate technique as well as limits on kinematic and event quality parameters are used to reduce and identify background events before τ_s, $\Delta\Gamma_s$ and ϕ_s are measured.
Preliminary results of a $B_s^0 \to J/\psi\phi$ analysis were released by the CMS collaboration [58]. The evaluation of $5.0\,\text{fb}^{-1}$, corresponding to ~ 14500 signal decays collected in 2011, with a cut based approach and the assumptions of $\phi_s = 0$ and no S-wave contribution yields $\Delta\Gamma_s = 0.048 \pm 0.024(\text{stat.}) \pm 0.003(\text{syst.})\,\text{ps}^{-1}$ and $\tau_s = 0.045\,80 \pm 0.000\,59(\text{stat.}) \pm 0.000\,22(\text{syst.})\,\text{cm}$.
The world's most precise measurement in the $B_s^0 \to J/\psi\phi$ channel was performed by the LHCb collaboration [59]. With an integrated luminosity of $1.0\,\text{fb}^{-1}$ and various same and opposite side tagging methods $\phi_s = 0.07 \pm 0.09(\text{stat.}) \pm 0.01(\text{syst.})$ is measured. The profile likelihood in the $\Delta\Gamma_s$ - ϕ_s plane derived in the analysis is shown in figure 2.13. LHCb performed an additional study inspecting the fraction of S-wave decays in the B_s^0 data depending on the invariant K^+K^- mass to determine the sign of $\Delta\Gamma_s$.

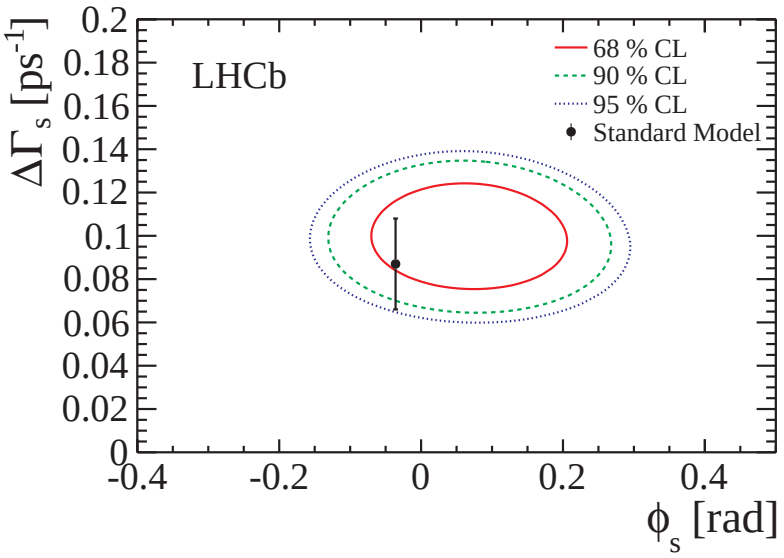

Figure 2.13: Two-dimensional profile likelihood in the $\Delta\Gamma_s$ - ϕ_s plane derived in the LHCb analyis of $B_s^0 \to J/\psi K^+K^-$. Only the statistical uncertainty is included. The Standard Model expectation of $\Delta\Gamma_s = 0.082 \pm 0.021\,\text{ps}^{-1}$ and $\phi_s = -0.036 \pm 0.002\,\text{rad}$ is shown as the black point with error bar. This figure was taken from [59].

Table 2.4: Summarized results of $B_s^0 \to J/\psi\phi$ analysis of Tevatron and LHC experiments. For each observable the central value is given followed by statistical and systematic uncertainty.

	CDF	**D0**	**CMS**	**LHCb**
$\boldsymbol{\Delta\Gamma_s}$ [ps^{-1}]	$0.068 \pm 0.026 \pm 0.009$	$0.163^{+0.065}_{-0.064}$ [1]	$0.048 \pm 0.024 \pm 0.003$	$0.100 \pm 0.016 \pm 0.003$
$\boldsymbol{\Gamma_s}$ [ps^{-1}]	$0.654 \pm 0.08 \pm 0.004$ [2]	$0.693^{+0.017}_{-0.018}$ [13]	$0.655 \pm 0.008 \pm 0.003$ [4]	$0.663 \pm 0.005 \pm 0.006$
$\boldsymbol{\phi_s}$ **[rad]**	- [5]	$-0.55^{+0.38}_{-0.36}$ [1]	- [6]	$0.07 \pm 0.09 \pm 0.01$

[1] Uncertainty includes statistical and systematic uncertainties.
[2] Derived from $\tau_s = 1.528 \pm 0.019(\text{stat.}) \pm 0.009(\text{syst.})\,\text{ps}$ [56].
[3] Derived from $\tau_s = 1.443^{+0.038}_{-0.036}\,\text{ps}$ [57]:.
[4] Derived from $\tau_s = 0.045\,80 \pm 0.000\,59(\text{stat.}) \pm 0.000\,22(\text{syst.})\,\text{cm}$ [58].
[5] CDF gives a 68 % confidence level for β_s as $\beta_s \in [-\pi/2, -1.51] \cup [-0.06, 0.30] \cup [1.26, \pi/2]$ [56].
[6] CMS fixes the value of ϕ_s to zero in the fit [58].

Chapter 3

The ATLAS Experiment

In this chapter the experimental setting used for the $B_s^0 \to J/\psi\phi$ analysis is introduced. ATLAS (**A** **T**oroidal **L**HC **A**pparatu**S**) is one of four particle detectors at the **L**arge **H**adron **C**ollider at CERN[1]. ATLAS is a general purpose detector designed to perform precision measurements of particles produced in proton-proton collisions at the LHC. The physical scope covers testing of the Standard Model predictions with high accuracy as well as the search for New Physics phenomena.
For the $B_s^0 \to J/\psi\phi$ analysis the measurements in the muon detector are used to select events identified by the $J/\psi \to \mu^+\mu^-$ decay. For the reconstruction of the B_s^0 signal decay and the determination of the primary vertex and the decay vertex, the high precision measurements of the inner tracking detectors are used.
In-depth descriptions of the technical details and properties of LHC and ATLAS can be found in [60–62].

3.1 The Large Hadron Collider

The LHC is a proton-proton synchrotron located at CERN near Geneva, Switzerland. With a circumference of 27 km it is one of the largest experiments that was ever built on planet earth. The circular particle accelerator is installed in the tunnel of the predecessor experiment LEP[2] at a depth of up to 175 m below the French-Swiss border. The 50 MeV protons, produced in a linear accelerator, gradually gain momentum in the pre-accelerators Pro-

[1] **C**onseil **E**uropéen pour la **R**echerche **N**ucléaire
[2] **L**arge **E**lectron-**P**ositron Collider

ton Synchrotron Booster, Proton Synchrotron and Super Proton Synchrotron before they are finally injected into the two vacuum pipes of the main accelerator ring with an energy of 450 GeV. In the LHC ring, bunches of more than 10^{11} protons are accumulated and accelerated to their peak energy before brought to collision. Superconducting magnets, cooled with liquid helium to a temperature of $\sim 2\,\mathrm{K}$, are installed in the tunnel along the beampipe to keep the proton bunches on their circular path. In 2011 the oppositely running proton beams were accelerated to an energy of 3.5 TeV colliding with a center-of-mass energy of 7 TeV. The center-of-mass energy was increased to 8 TeV for the 2012 run and is expected to reach the design value of 14 TeV in 2015. The LHC's design instantaneous luminosity of $\mathcal{L} = 10^{34}\,/\mathrm{cm}^2/\mathrm{s}$ provides a bunch collision rate of 40 MHz at four interaction points distributed around the ring. This is where the particle detectors ATLAS, CMS[3], LHCb[4] and ALICE[5] are located. ATLAS and CMS are general-purpose experiments sensitive to a wide range of physics phenomena. LHCb is a particle detector especially designed for B-physics and the purpose of ALICE is the study of the quark-gluon plasma in heavy-ion collisions[6]. Figure 3.1 shows an overview of the LHC accelerator facilities and particle detectors at CERN.

3.2 ATLAS Detector

ATLAS is the largest detector at the LHC with a length of 44 m and a height of 25 m. It has a weight of about 7000 tonnes and is forward-backward symmetric with respect to the interaction point. The broad physics program of ATLAS covers observation of the Higgs boson and measurement of its properties, the search for New Physics phenomena like SUSY[7] particles or extra dimensions, as well as precision measurements of Standard Model parameters like the top quark and gauge boson masses, their coupling strengths, CKM matrix elements and CP violation. To successfully handle all these physics topics, the detector has to fulfill several technical requirements:

- fast and radiation-hard electronics and sensor elements to cope with the experimental conditions at the LHC,

[3] **C**ompact **M**uon **S**olenoid

[4] **L**arge **H**adron **C**ollider **b**eauty experiment

[5] **A** **L**arge **I**on **C**ollider **E**xperiment

[6] In addition to the p-p collisions, the LHC program also includes shorter run periods of heavy-ion collisions, e.g. Pb-Pb at $\sqrt{s} = 5.52\,\mathrm{TeV}$.

[7] **Su**per **Sy**mmetry is a possible theoretical extension of the Standard Model that is based on the natural symmetry between fermions and bosons.

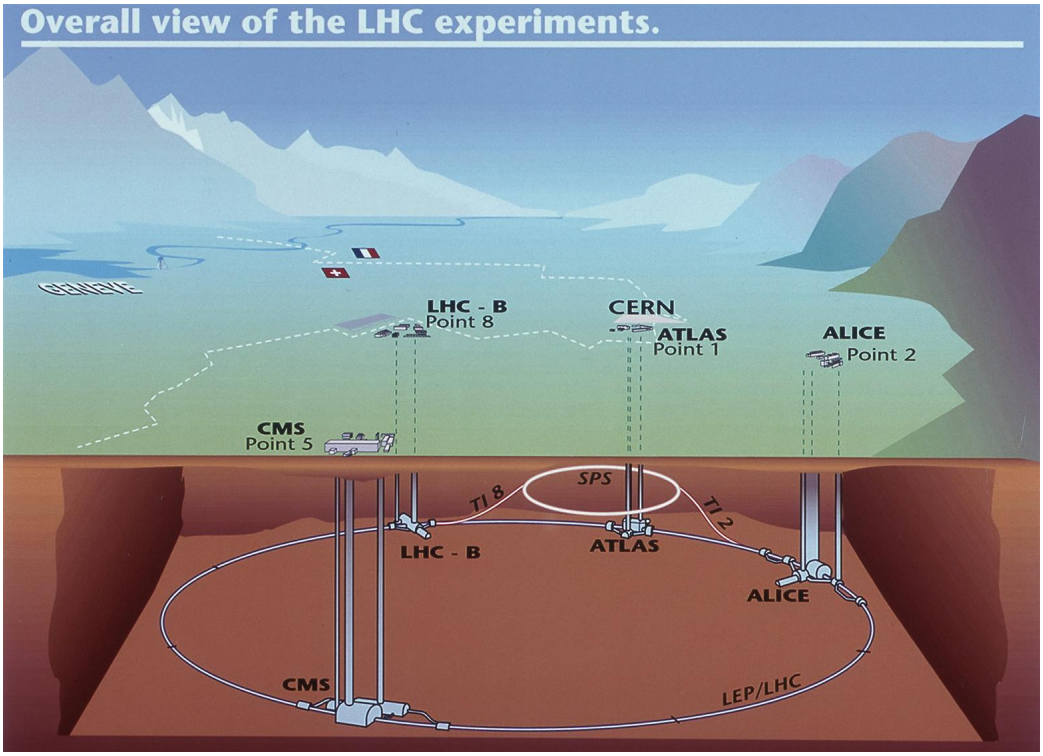

Figure 3.1: The four particle detectors around the LHC accelerator ring at CERN.

- high detector granularity to manage the particle fluxes and overlapping events,
- large acceptance in pseudorapidity with almost full azimuthal angle coverage,
- tracking systems with good charged-particle momentum resolution and high reconstruction efficiency,
- very good electromagnetic and hadronic calorimetry,
- specialized systems for efficient identification of muons and their high precision momentum measurement,
- good vertex detectors to allow precise determination of secondary vertices,
- efficient triggering with sufficient background rejection.

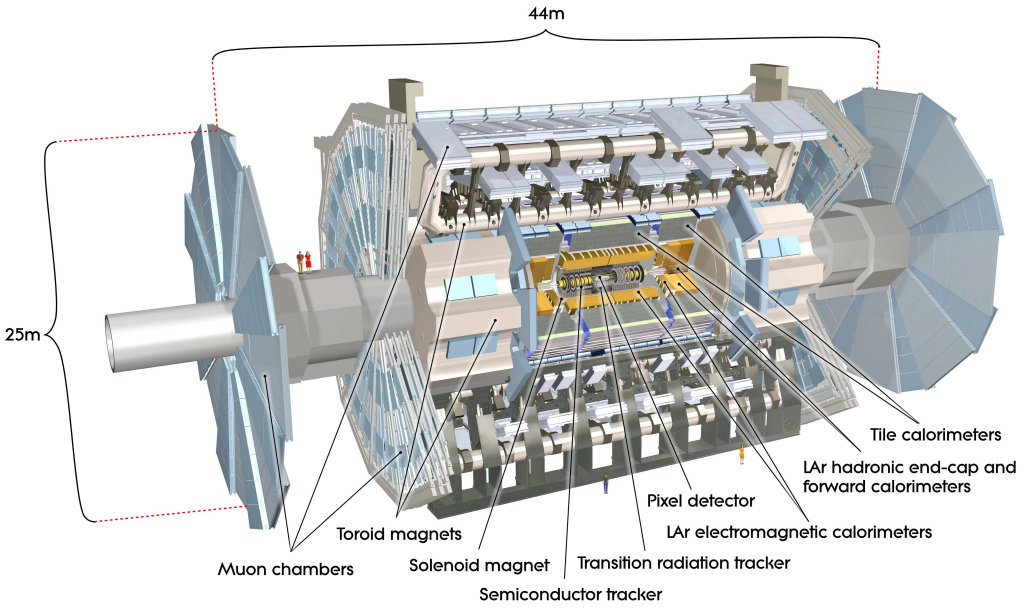

Figure 3.2: Illustration of the ATLAS detector and its subsystems [62].

To comply with these prerequisites the ATLAS detector consists of several layers of complementing subsystems, each fulfilling a different purpose. The inner tracking detectors are in the middle of ATLAS close to the beam pipe, surrounded by a solenoid magnet. The next layers are the electromagnetic and hadronic calorimeters followed by the outermost subdetector, the muon spectrometer with an air-core toroid magnet system. The ATLAS detector is illustrated in figure 3.2, and table 3.1 shows what particles can be detected in which of the different subsystems.

3.2.1 Coordinate System

To describe the ATLAS detector and the trajectories of particles produced in the $p-p$ collisions, a right handed coordinate system is defined in figure 3.3. The origin of the coordinate system is given by the nominal interaction point, and the z axis is defined along the beam direction. The xy plane is perpendicular to the beam direction, and the positive x axis points towards the center of the LHC accelerator ring, while the y axis points upwards.
The azimuthal angle ϕ is the angle around the beam axis and $\phi = 0$ denotes the positive x axis. The polar angle θ is the angle measured from the positive z axis: $\tan\theta = \frac{r}{z}$ with $r = \sqrt{x^2+y^2}$. At hadron-hadron colliders like the LHC, usually the pseudorapidity $\eta = -\ln(\tan\frac{\theta}{2})$ is used instead of θ.

Table 3.1: Different particles can be detected in the different subsystems inner detector (ID), electromagnetic calorimeter (ECAL), hadronic calorimeter (HCAL) and muon spectrometer (MS). Neutrinos are detected indirectly from the other particles in the event and missing energy or missing transverse momentum.

	ID	**ECAL**	**HCAL**	**MS**
Electron	√	√		
Photon		√		
Muon	√			√
Charged Hadron	√		√	
Neutral Hadron			√	
Neutrino				

The distance ΔR in the pseudorapidity-azimuthal angle space is defined as $\Delta R = \sqrt{\Delta\eta^2 + \Delta\phi^2}$. Transverse momentum p_T and transverse energy E_T are defined in the xy plane.

3.2.2 Magnet System

To identify and measure the trajectories of charged particles every particle detector needs to be embedded into a magnetic field. The magnet system of ATLAS consists of a central solenoid and three air-core toroids.

- The superconducting **central solenoid** of ATLAS surrounding the inner detector (see section 3.2.3) has a length of 5.3 m and a diameter of 2.5 m. It provides the inner tracking detectors with a magnetic field of 2 T which causes bending of charged particles trajectories in the xy plane.

- Three air-core **toroids** are used to generate the magnetic field for the muon spectrometer (see section 3.2.5). The barrel toroid as well as the two end-cap toroids consist of eight superconducting coils. The end-cap magnets are placed inside the barrel toroid at both ends and are rotated by 22.5° with respect to it. The toroid system provides a bending power of 1.5 to 5.5 T m in the pseudorapidity range $0 < |\eta| < 1.4$ and 1 to 7.5 T m in the region $1.6 < |\eta| < 2.7$.

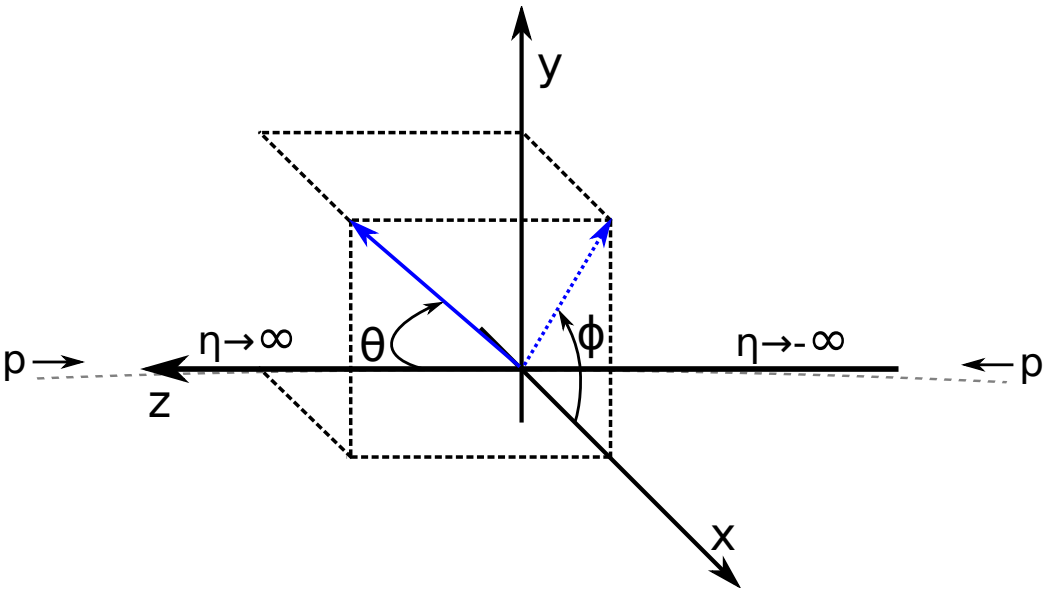

Figure 3.3: Coordinate system used in ATLAS.

3.2.3 Inner Detector

The inner detector is placed around the interaction point and is embedded in the magnetic field of the solenoid. It has a length of 6.2 m and a diameter of 2.1 m and is used to measure tracks and momenta of charged particles covering a pseudorapidity range of $|\eta| < 2.5$. The inner detector is composed of three subsystems (figure 3.4): a semiconductor pixel detector, a semiconductor strip detector and a transition radiation tracker.

The **pixel detector** is the innermost detector system and provides a very high granularity that is needed to precisely measure the tracks of charged particles. It consists of three layers of concentric cylinders in the barrel region and three disks in each end-cap region of ATLAS and thus a charged particle typically crosses three layers of pixel sensors. The pixel layers are segmented in $R-\phi$ and z with identical pixel sensors having a minimum size of $R-\phi \times z = 40 \times 500\,\mu\text{m}^2$. In the barrel the accuracies are 10 µm in $R-\phi$ and 115 µm in z, while the end-cap pixel sensors reach accuracies of 10 µm in $R-\phi$ and 115 µm in R. The pixel detector has more than 80 million readout channels and the innermost layer is situated only ~ 5 cm from the beam axis guaranteeing a high vertex reconstruction precision.

The **semiconductor tracker** (SCT) consists of four cylindrical barrel layers and nine end-cap disks on each side. Stereo strips are used to measure both coordinates. The SCT has a resolution of 17 µm in $R-\phi$ and 580 µm in

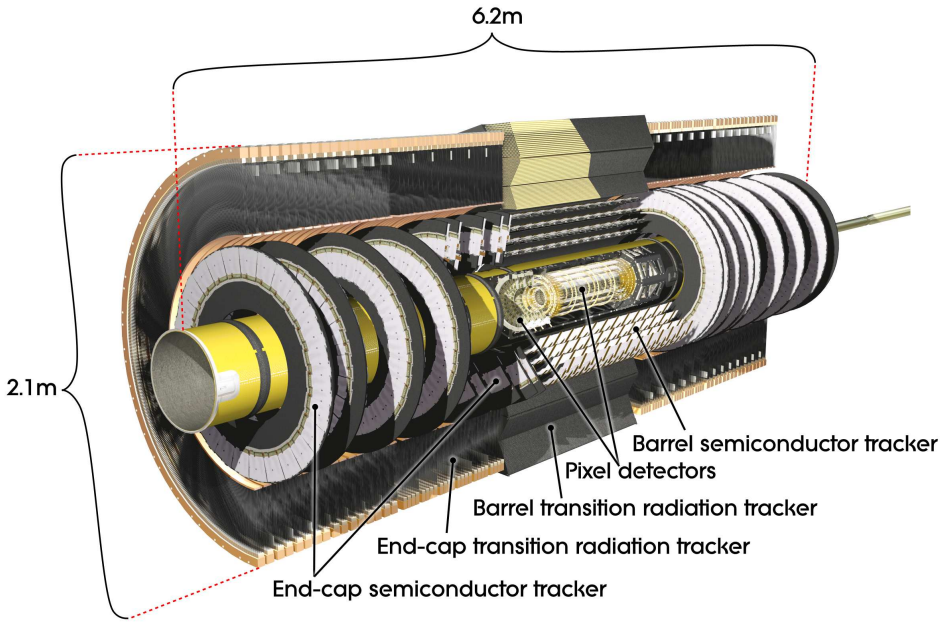

Figure 3.4: The inner detector tracking systems of ATLAS.

z in the barrel and 17 µm in $R-\phi$ and 580 µm in R in the end-caps. With a total of approximately 6.3 million readout channels the SCT contributes with four hits per track to the measurement of momentum, impact parameter and vertex position.

The **transition radiation tracker** (TRT) measures on average another ~ 36 hits per charged particle track. It consists of straw tubes with a diameter of 4 mm and a length covering a pseudorapidity region of $|\eta| < 2.0$. The TRT performs drift time measurements in the straw tubes. Hits in the TRT provide information only in $R-\phi$ with an accuracy of 113 µm per straw. With a length of 144 cm the straws are installed parallel to the beam axis in the barrel region. In the end-cap region straws with a length of 37 cm are arranged radially in wheels. A total of approximately 351 000 TRT readout channels contribute to the momentum measurement. In addition to the tracking information, the TRT has the capability to identify electrons using the transition radiation in the xenon containing gas mixture of the straw tubes.

3.2.4 Calorimetry

The calorimeter provides an energy measurement for particles via absorption. The ATLAS calorimeter system consists of two parts: the electromagnetic calorimeter designed for electrons and photons and a hadronic calorimeter designed to detect hadrons. Both are sampling calorimeters which means that they are constructed with layers of energy absorbing materials and sensor elements in between to measure the resulting particle showers. The **electromagnetic calorimeter** is placed around the central solenoid. Its absorber plates are made of lead and the gaps are filled with liquid argon. The particle showers are detected with accordion-shaped kapton electrodes. It has a total thickness of > 22 radiation lengths (X_0) in the barrel and $> 24 \cdot X_0$ in the end-caps.
The barrel part of the **hadronic calorimeter** is a tile calorimeter with steel absorbers and scintillator tiles as active material. The end-cap parts of the hadronic calorimeter utilize copper as absorber and liquid argon as sampling material. The total thickness of the detector corresponds to ~ 9.7 times the interaction length λ.

3.2.5 Muon Spectrometer

The purpose of the **muon spectrometer** (MS) of ATLAS (figure 3.5) is to identify muons and measure their momentum. In contrast to other particles, muons traverse the inner detectors and calorimeters almost without interaction and therefore provide clean signatures. The momentum measurement of the muons is based on the deflection of their tracks in the superconducting air-core toroid magnets. The toroids are arranged in such a way that they provide a magnetic field mostly orthogonal to the muon trajectories. The MS consists of separate muon chambers for triggering and high precision tracking. In both, barrel and end-caps, the chambers are arranged in three layers. The largest part of the pseudorapidity region is covered by monitored drift tubes (MDT) that are filled with a mixture of argon and carbon dioxide and provide a resolution of 80 mm. At pseudorapidity regions of $2 < |\eta| < 2.7$ cathode strip chambers (CSC), which are multiwire proportional chambers with cathodes segmented into strips, are used. An optical alignment system is used to provide the required information about the location of each part of the muon spectrometer. The pseudorapidity range $|\eta| < 2.4$ is covered by the muon trigger system, which consist of resistive plate chambers (RPC) in the barrel and thin gap chambers (TGC) in the end-caps.

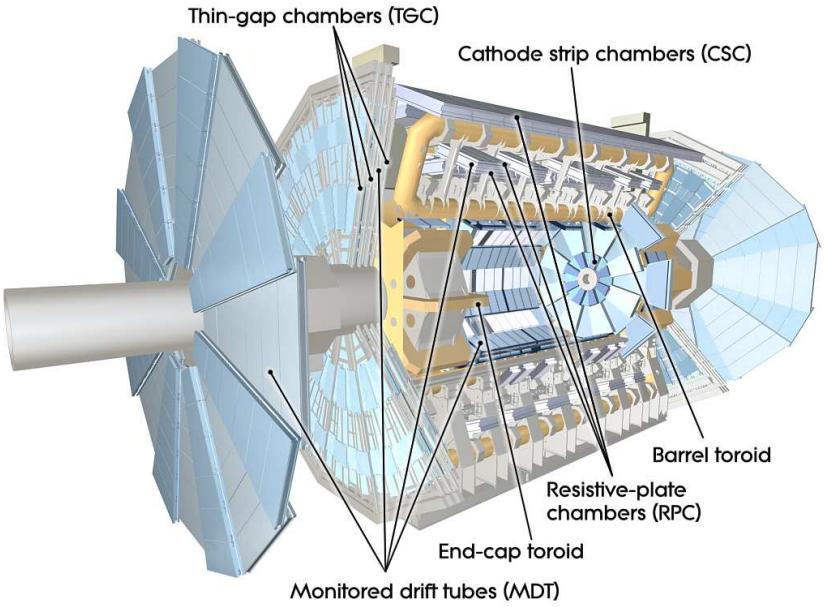

Figure 3.5: Cut-away view of the ATLAS muon spectrometer.

3.2.6 Trigger System

The LHC design provides a proton-proton bunch collision every 50 ns which corresponds to a collision rate of 40 MHz. Since an average event has a size of approximately 1.3 MB the maximum rate at which data can be stored is 200 Hz. This means that only 5 out of 10^6 events can be stored for physics analysis. The purpose of the ATLAS trigger system is to identify events of interest with high efficiency, but at the same time provide a high background rejection efficiency, and thus reduce the data rate to an amount feasible for permanent storage.

A simplified overview of the trigger system of ATLAS is shown in 3.6. It is divided into three levels of event selection: level 1 (L1), level 2 (L2) and the event filter (EF). At each level the decision made by the previous level is refined and, if necessary, additional selection criteria are applied. The L2 triger and the event filter are both software based and together are also referred to as high level trigger (HLT).

The **level 1** trigger is a hardware trigger that selects events based on information gathered in the calorimeters and trigger chambers of the muon spectrometer. Since the L1 decision has to be taken in less than 2.5 µs, signals in the calorimeters can only be evaluated with reduced granularity. The L1 trigger searches for muons, electrons, photons and jets with high

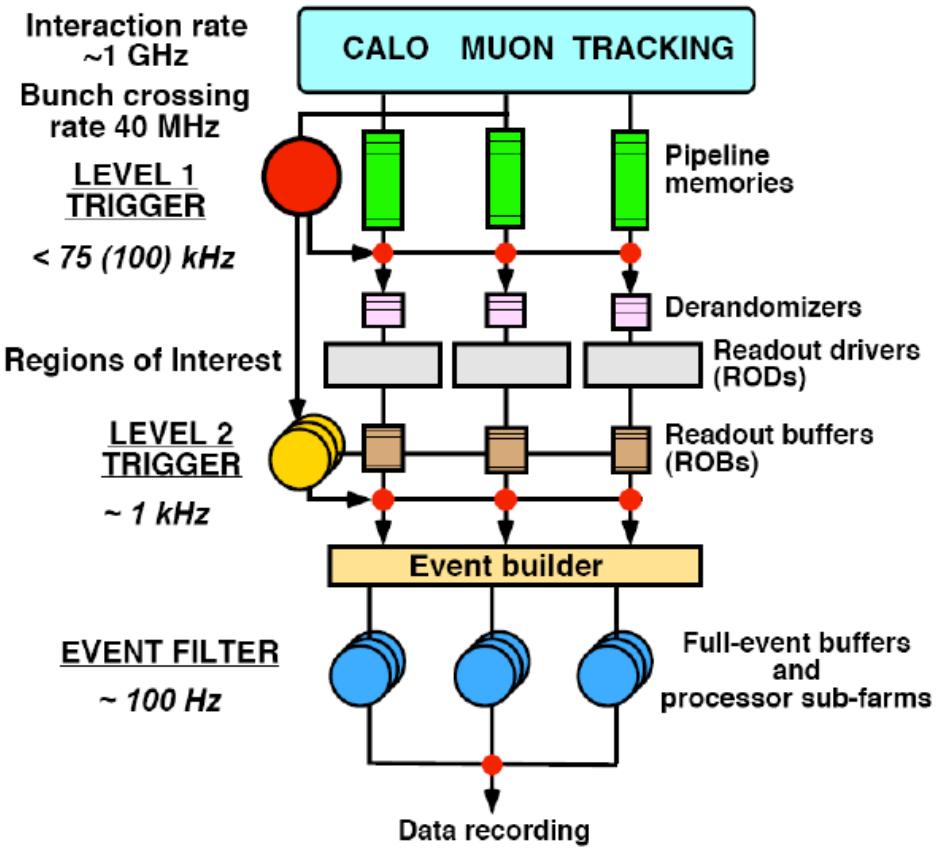

Figure 3.6: An overview of the ATLAS trigger system [63].

transverse momentum, for τ-leptons decaying into hadrons, as well as for large missing and total transverse energy. In each selected event the L1 trigger also defines regions-of-interest (RoIs) containing information about the geographical coordinates of interesting physics features combined with the selection criteria that were passed. During the decision taking the data is kept in pipeline memories and events passing the L1 trigger are transferred to the HLT. The L1 trigger reduces the rate to about 75 kHz.

The **L2 trigger** refines the event selection based on the RoIs defined by the L1 trigger. It makes use of the full granularity and also includes information collected in the inner detector within the RoIs, which corresponds to approximately 2 % of the total event data. A sequence of L2 algorithms is executed for individual RoIs and combinations of RoIs and further selection criteria are applied to select events for further analysis. The average processing time of an event in the L2 trigger is 40 ms and the resulting data rate is

approximately $\sim 1\,\mathrm{kHz}$.

The **event filter** takes the final decision over the remaining events. The event filter is based on software algorithms which are executed on a computer cluster. It makes use of the same software algorithms that are later used in the offline data analysis with an average event processing time of four seconds. Due to advanced pattern recognition techniques and calibrations the data rate is further reduced to $\sim 200\,\mathrm{Hz}$.

The HLT has access to more than 700 different algorithms and configurations. There are specific triggers for the different topologies used in the data analysis later. Since the data storage rate is limited, the total bandwidth is divided into the various ATLAS physics groups. In addition there are trigger chains needed for calibration and efficiency measurements, which either reuse physics trigger algorithms with different selection criteria, or make use of suitable additional trigger algorithms. The trigger chains are constantly monitored and adapted to the increasing luminosity during data-taking. In some cases it is necessary to prescale a trigger algorithm, which means that not every positive decision is taken into account.

Chapter 4

Data and Monte Carlo

This chapter gives a short summary about the data sample and Monte Carlo simulation that is used in the $B_s^0 \to J/\psi\phi$ analysis.

4.1 Data Sample

The analysis presented in this thesis uses the data collected with the ATLAS detector between February and November 2011. In that year, the LHC was running in $p-p$ mode with a center-of-mass energy of $\sqrt{s} = 7\,\text{TeV}$. Figure 4.1 shows the integrated luminosity delivered by the LHC and collected by ATLAS with stable beams in 2011. For the $B_s^0 \to J/\psi\phi$ analysis only data was used, where the muon spectrometer and the inner detector tracking systems were both operating correctly, which corresponds to $4.9\,\text{fb}^{-1}$.

From this data the following decay modes are reconstructed and used in the measurement:

- $B_s^0 \to J/\psi\phi$, where $J/\psi \to \mu^+\mu^-$ and $\phi \to K^+K^-$, is used to measure Γ_s, $\Delta\Gamma_s$ and ϕ_s.
- $B^\pm \to J/\psi K^\pm$, where $J/\psi \to \mu^+\mu^-$, is used for the calibration and validation of the flavor tagging methods.
- $B_d^0 \to J/\psi K^*$, where $J/\psi \to \mu^+\mu^-$ and $K^* \to K^+\pi^-$, is used as a cross-check of the flavor tagging methods.

In case of the decays of the neutral mesons, B_s^0 and B_d^0, also the charge

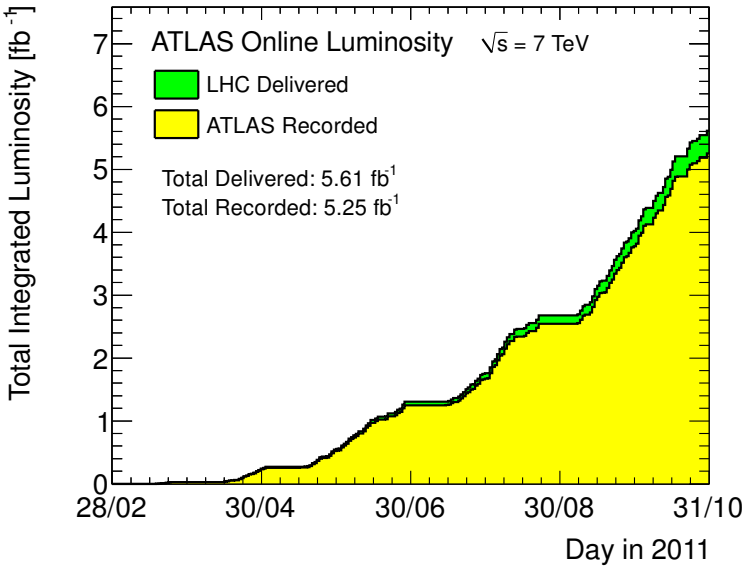

Figure 4.1: Cumulative luminosity delivered by LHC (green) and recorded by ATLAS (yellow) during stable beams in $p-p$ collisions at $\sqrt{s} = 7\,\text{TeV}$ in 2011.

conjugate decays are assumed. All decay modes are fully reconstructed, meaning that all final state particles (muons, kaons and pions) have been reconstructed from hits in the ATLAS detector. All three modes have the decay into a J/ψ in common and the resulting two muons represent a characteristic feature that can be exploited by the trigger algorithms in the online selection of the data. A detailed description of the triggers used in the analysis can be found in chapter 5. However, all $J/\psi \to \mu^+\mu^-$ events can pass the triggers, allowing a large portion of events from non-B decays. The data sample after the trigger selection will, for example, contain many J/ψ mesons thar are directly produced in $p-p$ collisions. Many of these events will be rejected in the offline reconstruction and selection, but still a large number of background events will be present in the final data ntuple, which have to be taken into account in the fit model. As already mentioned in section 2.5.3, the $B_s^0 \to J/\psi f_0$ decay and the non-resonant $B_s^0 \to J/\psi K^+K^-$ decay cannot be distinguished from the signal as they have the same final state. Therefore they are also contained in the data sample and are accounted for in the decay rate of the signal model. Since the $B_s^0 \to J/\psi\phi$ and $B_d^0 \to J/\psi K^*$ decays have a very similar topology, large parts of the reconstruction software are identical. The only differences are assumptions about the mass of the hadronic final state particles and the allowed mass window of the ϕ and K^*

mesons. The detailed reconstruction and selection of the B_s^0 are described in chapter 5. The specific selections for the reconstruction of the $B^{\pm}$ and B_d^0 decays are discussed in chapter 8.

4.2 Monte Carlo Simulation

In the $B_s^0 \to J/\psi\phi$ analysis simulated events, referred to as Monte Carlo (MC) data, is needed to determine detector effects, estimate backgrounds and model systematic effects. The simulation of MC data is a complex process which proceeds in several steps. In the first step the studied physics process is generated at particle level, which means that the $p-p$ collisions and all subsequent processes such as particle decay or hadronization are modeled. In the next step the generated processes are combined with the detector simulation. The trajectories of the particle determine where and when a response in the detector happens. A digitizer models the hits of the particles in the detector as if they were from real data. After this step the treatment of real and simulated data is the same except that each event of simulated data is associated to the initially generated physics process.

In the ATLAS collaboration, the event generator *Pythia 6* [54,64] is used to simulate B-physics processes. *Pythia 6* generates not only the signal process but also a very large amount of background processes in the $p-p$ collisions, which results in unrealistic computing requirements. In *Pythia 6* $b\bar{b}$ pairs are generated via the three processes discussed in section 2.6. As the cross sections of theses processes are quite small, only a very low fraction (1 %) of the generated $p-p$ collisions produce a $b\bar{b}$ pair. In addition, the signal processes of interest have usually a low branching ratio resulting in unacceptable CPU times for the generation of B-physics processes. A solution for this problem would be to artificially increase the probability for the $b\bar{b}$ production, but it turned out that doing this alters the resulting cross sections and p_T spectra [65] in a way that makes it impossible to use the simulated events for realistic MC studies.
Therefore, the *PythiaB* interface [65] is used to speed up the process by utilizing the repeated hadronization algorithm. It exploits the fact that the largest part of the simulation computing time is needed for parton collision. If a $b\bar{b}$ quark pair was produced in a collision, the event is cloned several times and for each clone the hadronization into b-hadrons is generated as if these were independent events. The number of cloned events is selected in a way that in average one event is accepted with the same parton collision to avoid biases in the MC sample. In addition *PythiaB* allows to explicitly

generate one exclusive final state for the b-hadron of interest, while all other b-hadrons may decay freely. With the usage of the *PythiaB* interface the efficiency of the MC event generation improves a lot. All MC sample used in this analysis were generated using *PythiaB*.

To simulate the detector response *Geant4* [66] is used. A detailed model of the whole ATLAS detector including active parts, magnet systems and dead material is defined and the interaction between the high energy particles traversing the detector volume and the detector material is simulated. The simulated interactions include energy loss, ionization, multiple scattering and bremsstrahlung. in addition to the energy deposits in the active detector material, this also results in the creation of secondary particles, electromagnetic showers or particles from nuclear interactions.
In the next step the response of the detector electronics to the energy deposits is simulated, which is called digitization. To produce a realistic and data like output of the simulation, each detector subsystem has its own digitization algorithms [67] that were tested in beam tests during the development and construction of the ATLAS detector.
Because of the large luminosities at the LHC, more than one $p-p$ collision happens per bunch crossing. In the 2011 dataset used for the analysis the number of these pileup interactions is ~ 5.6. The pileup events also need to be accounted for in the MC simulation, where only one collision is generated. To reduce the necessary computing power for the pileup interactions, large samples of minimum bias events are pre-simulated and digitized. In the last step of the MC simulation the dedicated physics processes are combined with these minimum bias events to account for the multiplicity of $p-p$ collisions per bunch crossing.

For the $B_s^0 \to J/\psi\phi$ analysis the following simulated datasets are used:

- 12 million $B_s^0 \to J/\psi\phi$ signal events with flat angular distributions to determine angular, trigger, reconstruction and selection efficiencies.
- 100 thousand $B_s^0 \to J/\psi\phi$ signal events with realistic angular distributions to determine effects of residual misalignment of the inner detector. This MC sample was also used for the validation of the signal model of the fitter and for the determination of a bias induced by the muon triggers (see chapter 6).
- $B_d^0 \to J/\psi K^*$, $B_d^0 \to J/\psi K^+\pi^-$, $B_d^0 \to J/\psi K^+K^-$, $bb \to J/\psi X$ and $pp \to J/\psi X$ to study the background contributions (see chapter 5) and determine the fractions of dedicated background included in the fit (see chapter 6).

The reconstruction and analysis software works the same way for simulated MC events as it does for real data. The only difference is that in the MC simulation the signals in the detector are connected to the generator particles. This means that every reconstructed object in the analysis is associated to the initially generated particles, which allows to test if the analysis algorithms work as intended. MC simulation is also used to determine selection efficiencies and to study the composition of the background events.

Chapter 5

Data Selection and Event Reconstruction

In this chapter, the procedure for the reconstruction of the signal decays from the data collected with the ATLAS detector is presented. First the triggers used to identify events containing possible signal candidates are described. Then, the reconstruction of the B_s^0 mesons from the final state particles, including kinematic selection cuts, is illustrated. An overview of all steps of the reconstruction of the signal B_s^0 is illustrated in figure 5.1.

5.1 Trigger Selection

The basis of the trigger algorithms used to select events for the $B_s^0 \to J/\psi\phi$ analysis is the identification of the characteristic $J/\psi \to \mu^+\mu^-$ decay. Due to the high luminosities at LHC, it is not sufficient to select events containing two muons with certain transverse momenta. In addition, the triggers make use of a fast vertexing algorithm that checks whether the two muon candidates could originate from a common vertex. The applied trigger chains can be divided into two categories:

- The **topological di-muon trigger** is the basic algorithm usable in all luminosities and it requires signatures of two muons at L1. At L2 the tracks in the muon spectrometer are reconstructed as well as inner detector tracks in the corresponding RoIs. The tracks of the different subdetectors are matched and the two muons are fitted into a common vertex and the invariant mass of the di-muon pair is calculated.

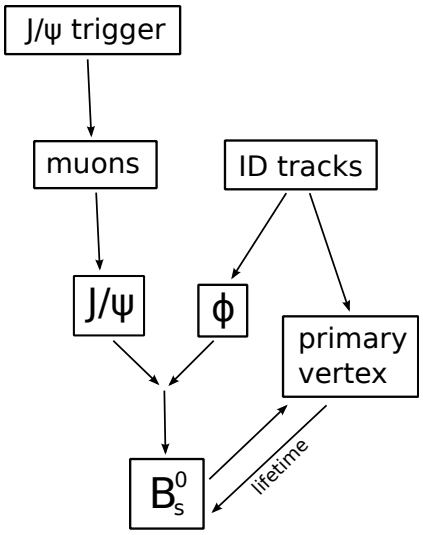

Figure 5.1: Overview of the stepwise reconstruction of the signal decay.

If the quality of the vertex fit and the invariant mass satisfies the selection criteria, the event is accepted. Only events where both muons have a transverse momentum of at least 4 GeV can be selected since muons with lower p_T hardly reach the ATLAS muon spectrometer due to energy loss in the calorimeters.

- The **TrigDiMuon trigger** requires the signature of only a single muon at L1. The second muon is searched for in an extended RoI (region of interest; see chapter 3.2.6) in the inner detector. If one of the ID tracks fulfills certain selection criteria to form a J/ψ with the first muon, the possible hits in the muon spectrometer are searched for in a region around the extrapolated ID track. Again a vertex fit and the invariant mass of the di-muon pair have to meet the requirements. This algorithm has the capability to select events with asymmetric muon p_T. The threshold for the L1 muon p_T is 4 GeV but the second muon can have a p_T down to 2.5 GeV.

Several configurations with different selection cuts exist for each of the triggers. The minimum L1 muon p_T threshold can for example be 4 GeV or 6 GeV. For the L2 selection an invariant di-muon mass window is chosen around the J/ψ mass of 2.5 GeV to 4.3 GeV. Table 5.1 shows the trigger topologies that were used to collect the data in each period of the data taking. The names of the trigger chains indicate the muon p_T cuts, the width of the allowed invariant J/ψ mass window ("tight") and the selection

Table 5.1: Table showing the different triggers that were used in each period of the data taking. The portion of total events in each period selected by the trigger is given. The first four triggers in the table are of the TrigDiMuon type, and the last four are topological di-muon triggers. The numbers indicate the required minimum muon p_T. Due to overlap of different triggers, the sum of the numbers in each column can be larger than one. The first three triggers in the list were prescaled and an average prescale factor is given.

	Prescale	B to F	G to H	I	J	K	L	M
TrigDiMuon:								
EF_mu4_Jpsimumu	26.27	9 %	7 %					
EF_mu6_Jpsimumu	1.34	67 %	23 %					
EF_mu6_Jpsimumu_tight	3.98	25 %	50 %	30 %	18 %	23 %		
EF_mu10_Jpsimumu	1.0	26 %	29 %	34 %	30 %	31 %		
Topological di-muon:								
EF_2mu4_Jpsimumu	1.0	48 %	54 %	62 %	69 %	68 %		
EF_2mu4T_Jpsimumu	1.0						78 %	75 %
EF_mu4mu6_Jpsimumu	1.0	13 %	39 %	46 %	51 %			
EF_mu4Tmu6_Jpsimumu	1.0						58 %	56 %

criteria applied to the inner detector tracks ("T"). A detailed discussion of the triggers specialized on B-physics used in ATLAS can be found in [62,68].

Figure 5.2 shows the mass and η distributions of the total angled $B_s^0 \to J/\psi\phi$ signal MC sample and after applying the trigger selection. The trigger selection efficiency determined from the simulated MC data sample using the triggers listed in table 5.1 is $\sim 79\,\%$ of the signal events in the fiducial volume of the detector. It can also be seen in figure 5.2 that a larger fraction of B_s^0 candidates is reconstructed in the barrel part of the detector than in the detector end-caps.

5.2 $B_s^0 \to J/\psi\phi$ Decay Reconstruction

After the data has been selected by the di-muon triggers described in the previous section, possible signal candidates are reconstructed in an offline analysis. The procedure to reconstruct the decay chain includes the fitting and refitting of tracks and vertices, kinematic reconstruction of the decay and applying selection cuts to reduce the background. In the follow-

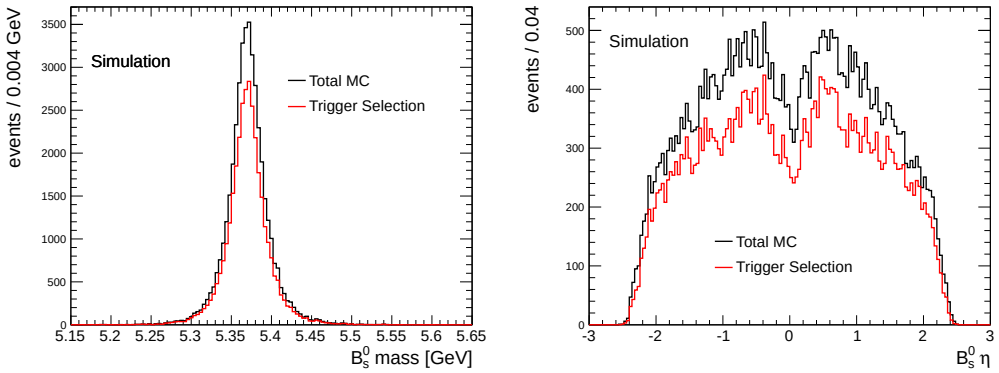

Figure 5.2: Mass (left) and η (right) distributions of simulated signal events before (black) and after the trigger selection (red).

ing two sections track fitting and vertexing are explained and afterwards the reconstruction of the signal decay is discussed.

5.2.1 Track Fitting

When the particles produced in $p-p$ collisions traverse the detector volume, they create electric signals, called hits, in the different detector subsystem. A particle track can then be fitted to the coordinates of several hits, taking into account deflection through the magnetic fields and energy loss in the detector material. For all tracks this happens with the information collected in the inner detector. For muons an additional track is fitted to the hits in the muon spectrometer and, if possible, matched to an inner detector track [62]. In the $B_s^0 \to J/\psi\phi$ analysis the p_T of the muon tracks is determined only from the measurements in the inner detector, because it provides a better resolution in the relevant low p_T region. The contribution of the muon spectrometer to the p_T measurement in the low p_T region is negligible. The measurements in the muon spectrometer are still needed for the triggers and to identify the corresponding inner detector tracks to the tracks found in the MS.

5.2.2 Vertex Fitting

Determining the location of decay and production vertices is an essential part of the decay chain reconstruction. In ATLAS vertexing is performed using algorithms based on the Kalman filter approach [69]. Tracks that were

reconstructed in the detector are fitted together with the assumption that they originate from a common vertex. The quality of the vertex fit is given by the software in form of a χ^2 probability, which is used to reject or accept the fitted vertices. For B meson lifetime measurements the decay vertex and a primary vertex are needed. The primary vertex corresponds to the production vertex of the B meson and is determined in a fit to tracks that are not associated to the signal B decay. The lifetime is calculated from the vertex positions using equation 2.67.

5.2.3 Signal Reconstruction

In addition to the trigger requirement, events used for the $B_s^0 \to J/\psi\phi$ analysis also have to pass the following criteria:

- Events must contain at least one reconstructed primary vertex which was built from at least four inner detector tracks.
- Events must contain at least one pair of oppositely charged muon candidates that were reconstructed combining information from the inner detector and muon spectrometer.

It is required that the tracks used for the B_s^0 reconstruction have at least one hit in the pixel detector and at least four hits in the silicon strip detector.

The first step of the offline reconstruction process is the formation of J/ψ candidates. Pairs of oppositely charged muons are built from all muon candidates in the event. Two types of muons coming from the ATLAS reconstruction software are taken into account:

- **Combined muons** have a full track in the muon spectrometer that is matched to a full track in the inner detector.
- **Segment tagged muons** have a full track in the inner detector that is matched to track segments in the muon spectrometer.

The two muons of each muon pair are fitted to a common vertex and accepted for further analysis if the vertex fit satisfies the quality criteria of χ^2 per number of degrees of freedom (χ^2/ndf) smaller than 10. The measured track parameters are then used to calculate the invariant mass of the muon pair which is required to be in a mass window around the world average J/ψ mass

Table 5.2: Three different mass windows are accepted for the invariant di-muon mass depending on where the two muons have passed the detector.

combination	muon 1	muon 2	J/ψ mass window
barrel / barrel	$\lvert\eta\rvert < 1.05$	$\lvert\eta\rvert < 1.05$	$2.959\,\text{GeV} - 3.229\,\text{GeV}$
barrel / end-cap	$\lvert\eta\rvert < 1.05$	$1.05 < \lvert\eta\rvert < 2.5$	$2.913\,\text{GeV} - 3.273\,\text{GeV}$
end-cap / end-cap	$1.05 < \lvert\eta\rvert < 2.5$	$1.05 < \lvert\eta\rvert < 2.5$	$2.852\,\text{GeV} - 3.332\,\text{GeV}$

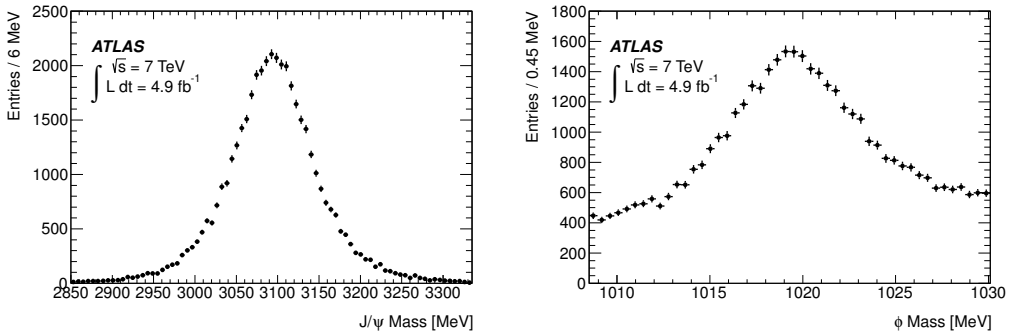

Figure 5.3: Mass distribution of the $J\psi \to \mu^+\mu^-$ (left) and $\phi \to K^+K^-$ (right) decays for B_s^0 candidates in the mass interval $5.317\,\text{GeV} - 5.417\,\text{GeV}$.

of 3.0969 GeV [21]. Depending on where the muons traversed the detector, the accepted interval for the invariant mass is different, because the mass resolution in the barrel part of the detector is better than in the end-caps. A maximum likelihood fit to the J/ψ mass is performed to determine mass and resolution in three different cases. In each fit the signal region is defined in such a way that it contains 99.8 % of the identified J/ψ candidates. Table 5.2 shows the resulting mass windows for the three combinations which are symmetric around the fitted mean value. The di-muon pairs are accepted as J/ψ candidates for further analysis steps if their invariant mass lies in the corresponding allowed mass range. Figure 5.3 shows the distribution of invariant $J/\psi \to \mu^+\mu^-$ mass for B_s^0 candidates in the signal mass region.

The next step is the building of the the ϕ candidates. The approach is basically the same as for the J/ψ candidates. All possible combinations of two inner detector tracks, fulfilling the requirements $p_T > 0.5\,\text{GeV}$ and $|\eta| < 2.5$, are taken into account. The two tracks must have opposite charge and must not be identified as muons. The invariant mass of the two tracks is calculated under the assumption that they are kaons, and has to lie within the interval $1.0085\,\text{GeV} < m(K^+K^-) < 1.0305\,\text{GeV}$. The invariant $\phi \to K^+K^-$ mass distribution for $B_s^0 \to J/\psi\phi$ candidates in the signal mass region is

shown in figure 5.3.

For the B_s^0 candidates the four tracks of each combination of J/ψ and ϕ in each event are fitted to a common vertex. In this fit the invariant mass calculated from the two muons is fixed to the world average J/ψ mass [21]. If the vertex fit fulfills $\chi^2/ndf < 3$ and all three tracks of $\phi \to K^+K^-$ comply with the criteria $p_T > 1\,\text{GeV}$, the quadruplet of tracks is accepted as a B_s^0 candidate for further analysis. Within the mass range of $5.15 < m(B_s^0) < 5.65\,\text{GeV}$ a total of 131 thousand B_s^0 candidates was found in the data.

In the last step of the reconstruction, the lifetime is calculated from the transverse distance between the primary vertex and the B meson decay vertex (see equation 2.67). Due to the high luminosity at LHC the average number of pileup interactions in the selected data is ~ 5.6. Pileup means that several primary interactions took place in one bunch crossing, leading to several reconstructed primary vertices. Consequently it is necessary to pick one primary vertex to calculate the B meson lifetime. First the primary vertices are refitted excluding all particles used in the B_s^0 meson reconstruction. To discriminate the best primary vertex, the three-dimensional impact parameter is calculated as the distance between the flight path of the B_s^0 meson to the primary vertex. The flight path of the B_s^0 meson is the line extrapolated from the B_s^0 decay vertex in the opposite direction of the B_s^0 momentum. The primary vertex with the smallest three-dimensional impact parameter is chosen. A test with MC simulated data showed that less than 1 % B_s^0 candidates are assigned to the wrong primary vertex using this selection method and that the effect on the result of the fit is negligible.

To determine the efficiency for reconstruction of the signal decays, the $B_s^0 \to J/\psi\phi$ MC sample with realistically simulated transversity angles is used. This MC sample contains 10^5 simulated events. After running the reconstruction algorithm and applying the selection cuts described above, ~ 42319 B_s^0 candidates remain. However, not all of the candidates are selected by the trigger chains described in section 5.1, and thus the overall B_s^0 candidate selection efficiency is $\sim 33\,\%$.

5.3 Fitter Input

After the reconstruction of the B_s^0 candidates an unbinned maximum likelihood fit is performed (see chapter 6). The quantities of the reconstructed B_s^0 candidates are calculated during the reconstruction from the measured signals of the decay products in the detector. The input variables entering

the fit are:

- mass and mass uncertainty of the B_s^0 candidate,
- lifetime and lifetime uncertainty of the B_s^0 candidate,
- three transversity angles θ, ψ and ϕ.

In addition, the tagged fit utilizes the outcome of the flavor tagging in form of a probability that the B_s^0 candidate was initially a particle or an antiparticle. The discussion of the flavor tagging methods and the derivation of the tag probability is discussed in chapter 8.

5.4 Background Composition

The reconstructed data sample does not only contain the signal $B_s^0 \to J/\psi\phi$ decay, but also background contributions from different sources that survived the selection cuts. To determine the background composition simulated MC samples are used and processed through the reconstruction algorithm. Figure 5.4 shows the mass distribution of the B_s^0 candidates reconstructed in six different MC samples of signal and background. The background contributions are scaled relative to the signal decay according to their branching fractions given in [21].

The background contribution denoted by $pp \to J/\psi X$ corresponds to J/ψ mesons that are directly produced in the $p-p$ collisions. The B_s^0 candidates reconstructed from this combinatorical background are reconstructed from the prompt J/ψ meson and two additional tracks in the event which satisfy all selection criteria. The combinatorical background does not have a significant lifetime which will be accounted for in the fit model (see chapter 6).
The source of another background contribution to the data sample are $bb \to J/\psi X$ decays. This background includes all b-hadrons that decay into a J/ψ meson (apart from the signal decays and the background contributions explained in the next paragraph). The B_s^0 candidates are reconstructed from the J/ψ meson and two hadronic tracks that are associated to the same primary vertex as the two muons from the J/ψ meson. As this background corresponds to real b-hadron decays it is expected to have a non-zero lifetime which will also be taken into account in the fit model (see chapter 6).
A specific background source are $B_d^0 \to J/\psi K^*(K^+\pi^-)$ decays, non-resonant $B_d^0 \to J/\psi K^+\pi^-$ decays and their charge conjugated decays. As the ATLAS detector provides no possibility to distinguish between kaons and pions, the

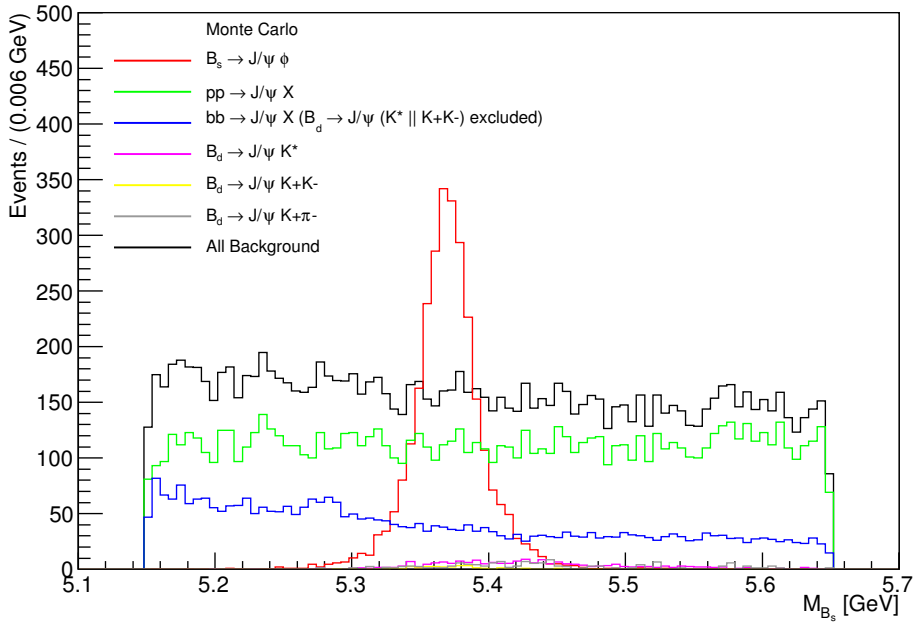

Figure 5.4: Mass distribution of the B_s^0 candidates reconstructed in MC samples of signal and the different backgrounds. The same plot with logarithmic scale on the y-axis can be found in appendix C.1.

final state pions of these decays are identified as kaons. When reconstructing the B_s^0 candidates a kaon hypothesis is used for the pion, which means that the pion is assumed to have the mass of a kaon. The calculated mass of the B_s^0 candidates reconstructed in the MC samples corresponding to the specific background lies rather in the B_s^0 mass range than in the lower B_d^0 mass range and can therefore not be excluded by a cut on the B_s^0 candidate mass. This is also the reason why the dedicated B_d^0 backgrounds are sometimes referred to as B_d^0 reflections. The mass, lifetime and angular distributions of the B_d^0 reflections are studied on the simulated MC samples described in chapter 4. In the likelihood function the B_d^0 backgrounds are treated by separate dedicated terms which will be discussed in chapter 6.
A possible background contribution from the $B_d^0 \to J/\psi K^+K^-$ decay was investigated but found to be very small and is therefore neglected in the analysis.

Table 5.3 shows the fraction of event that remains after selection cuts that are used in the reconstruction of the B_s^0 candidates. The numbers were

Table 5.3: Fraction of events of the signal decay and the different backgrounds that remains after cuts on the B_s^0 vertex fit, the p_T of the kaons and the invariant K^+K^- mass.

Decay Channel	B_s^0 $\chi^2/ndf < 3$	$p_T(K^\pm) > 1\,\text{GeV}$	$1.0085\,\text{GeV} < m(K^+K^-) < 1.0305\,\text{GeV}$
$B_s^0 \to J/\psi\phi$	96.0 %	93.7 %	94.4 %
$bb \to J/\psi X$	57.7 %	64.6 %	8.5 %
$pp \to J/\psi X$	86.6 %	57.0 %	10.1 %
$B_d^0 \to J/\psi K^*$	94.7 %	91.1 %	1.8 %
$B_d^0 \to J/\psi K^+\pi^-$	93.0 %	94.3 %	6.4 %

determined by processing the reconstruction algorithm with MC samples of the signal decay and the different backgrounds. The best performance in terms of background reduction is achieved by requiring the invariant K^+K^- mass to lie in the narrow ϕ meson mass window of 1.0085 GeV to 1.0305 GeV.

Chapter 6

Angular Analysis of $B_s^0 \to J/\psi\phi$

In this chapter the fit method of the angular analysis used to extract the physics parameters from the reconstructed B_s^0 candidates is described. At first the maximum likelihood method is introduced, followed by a detailed description of the likelihood function. The likelihood function has numerous components that describe the signal and background shapes of the variable distributions of the B_s^0 candidates. Each component is specified in form of a normalized probability density function (PDF) which will be presented in the following sections. In the last section of this chapter, the treatment of a time-dependent bias caused by the muon triggers is discussed.

6.1 Maximum Likelihood Method

In the $B_s^0 \to J/\psi\phi$ analysis, a simultaneous unbinned maximum likelihood fit of mass, time and angular distribution of the measured variables is used to extract values for the parameters of interest. The maximum likelihood method is a technique to estimate parameters of a statistical model that describes the data. The values of the parameters are estimated such that the likelihood function of the pre-defined model reaches a maximum. The model describing the data is defined by a set of PDFs. The PDF $P(\vec{x}|\vec{p})$ constitutes a function that determines the probability density to observe the measured variables $\vec{x}$ in the events, for the given set of unknown parameters

$\vec{p}$. The likelihood function is the product of the PDFs for each event:

$$\mathcal{L}(\vec{p}) = \prod_{i=1}^{N} P(\vec{x}_i|\vec{p}) \tag{6.1}$$

where N is the number of events in the dataset. The values of the parameters $\vec{p}$ are estimated by maximizing the likelihood function. It is usually easier to find the maximum of $\ln \mathcal{L}$, which is in the same spot as the maximum of $\mathcal{L}$, because the product in equation 6.3 converts into a sum.

$$\ln \mathcal{L}(\vec{p}) = \sum_{i=1}^{N} \ln P(\vec{x}_i|\vec{p}) \tag{6.2}$$

The estimation of the parameters in the $B_s^0 \to J/\psi\phi$ analysis is performed using the *MINUIT* package [70] which numerically minimizes the negative logarithm of the likelihood function $-\ln \mathcal{L}(\vec{p})$. Technically the implementation of *MINUIT* in the *ROOT* data analysis framework [71] is utilized.

6.2 Components of the Likelihood Function

To extract the parameters of the $B_s^0 \to J/\psi\phi$ decay, a simultaneous unbinned maximum likelihood fit of mass, proper decay time and angular distribution of the B_s^0 candidates is performed. The purpose of the mass fit is to separate the signal from the background, and the angular fit serves to disentangle the CP even and CP odd states. The aim of the proper decay time fit is to extract the parameters of interest that describe the time-dependence of the B_s^0 mesons decay such as ϕ_s, Γ_s and $\Delta\Gamma_s$. The PDFs in the likelihood function depend on the measured quantities mass m and mass uncertainty σ_m, proper decay time t and its uncertainty σ_t and the transversity angles $\Omega = (\theta, \psi, \phi)$ of the selected decay candidates. The total likelihood is a combination of the signal and background PDFs:

$$\begin{aligned} \ln \mathcal{L} = \sum_{i=1}^{N} w_i \cdot \ln\{ & f_s \cdot \mathcal{F}_s(m_i, t_i, \Omega_i) + f_s \cdot f_{B_d^0} \cdot \mathcal{F}_{B_d^0}(m_i, t_i, \Omega_i) \\ & + (1 - f_s \cdot (1 + f_{B_d^0})) \cdot \mathcal{F}_{bkg}(m_i, t_i, \Omega_i)\} \end{aligned} \tag{6.3}$$

where N is the number of selected candidates and w_i is a weighting factor to account for the lifetime dependent trigger efficiency that will be discussed in section 6.8. The mass m_i, the proper decay time t_i and the decay angles

Ω_i are the data values measured for each event i. f_s denotes the fraction of signal candidates and $\mathcal{F}_s(m_i, t_i, \Omega_i)$ is the total PDF of the signal component. $f_{B_d^0}$ is the fraction of the dedicated B_d^0 meson background events relative to the number of signal events and $\mathcal{F}_{B_d^0}(m_i, t_i, \Omega_i)$ is the PDF modeling this background. $f_{B_d^0}$ and the parameters of $\mathcal{F}_{B_d^0}(m_i, t_i, \Omega_i)$ are fixed in the maximum likelihood fit. The dedicated background from B_d^0 mesons and the components of its PDF are explained in section 6.7. The general background is described by the background PDF $\mathcal{F}_{bkg}(m_i, t_i, \Omega_i)$. The PDFs for signal and backgrounds are itself products of individual PDFs for the measured quantities. The signal PDF is defined as

$$\mathcal{F}_s(m_i, t_i, \Omega_i) = P_s(m_i|\sigma_{m_i}) \cdot P_s(\sigma_{m_i}) \cdot P_s(\Omega_i, t_i|\sigma_{t_i}) \cdot P_s(\sigma_{t_i}) \cdot A(\Omega_i, p_{\mathrm{T}i}) \cdot P_s(p_{\mathrm{T}i}) \tag{6.4}$$

where the individual terms are:

- the B_s^0 signal mass PDF $P_s(m_i|\sigma_{m_i})$,
- the mass uncertainty PDF $P_s(\sigma_{m_i})$,
- the signal decay time and angular PDF $P_s(\Omega_i, t_i|\sigma_{t_i})$,
- the proper decay time uncertainty PDF $P_s(\sigma_{t_i})$,
- the detector efficiency PDF $A(\Omega_i, p_{\mathrm{T}i})$,
- a PDF describing the B_s^0 transverse momentum $P_s(p_{\mathrm{T}i})$.

The total general background PDF is defined as

$$\mathcal{F}_{bkg}(m_i, t_i, \Omega_i) = P_b(m_i) \cdot P_b(\sigma_{m_i}) \cdot P_b(t_i|\sigma_{t_i}) \cdot P_b(\sigma_{t_i}) \cdot P_b(\theta) \cdot P_b(\psi) \cdot P_b(\phi) \cdot P_b(p_{\mathrm{T}i}) \tag{6.5}$$

with

- the background mass PDF $P_b(m_i)$,
- the mass uncertainty PDF $P_b(\sigma_{m_i})$,
- the proper decay time PDF $P_b(t_i|\sigma_{t_i})$,
- the proper decay time uncertainty PDF $P_b(\sigma_{t_i})$,
- the PDFs of the background angles $P_b(\theta)$, $P_b(\psi)$ and $P_b(\phi)$,
- a PDF describing the transverse momentum $P_b(p_{\mathrm{T}i})$.

In the following sections the different components of the likelihood function for the $B_s^0 \to J/\psi\phi$ analysis are discussed. Each component is a normalized function of one or more measured variables. If not stated differently the same PDFs are used in the untagged and tagged analysis. The distinctive features of the likelihood functions for each case will be discussed in chapter 7 and 8.

6.3 Mass Model

The mass distribution of the B_s^0 meson candidates has a distinct peak and thus the mass fit serves to separate the signal from the background. The PDF of the signal mass is modeled as a Gaussian function smeared with an event-by-event mass resolution that is normalized over the range $5.15\,\text{GeV} < m(B_s^0) < 5.65\,\text{GeV}$.

$$P_s(m|\sigma_m) = \frac{\dfrac{1}{\sqrt{2\pi}s_m\sigma_m} e^{-\frac{1}{2}\left(\frac{m-M}{s_m\sigma_m}\right)^2}}{\frac{1}{2}\left[erf\left(\frac{M_{max}-M}{\sqrt{2}s_m\sigma_m}\right) - erf\left(\frac{M_{min}-M}{\sqrt{2}s_m\sigma_m}\right)\right]} \tag{6.6}$$

M is the position of the B_s^0 peak, and the measured mass uncertainty σ_m is scaled by the scale factor s_m to account for misestimation of the mass errors. M_{max} and M_{min} are the upper and lower limits of the mass range and erf is the error function [72] defined as $erf(x) = \frac{2}{\sqrt{\pi}} \int_0^x e^{-t^2}\,dt$.

The background mass is modeled by a linear function, normalized over the same mass range as the signal PDF:

$$P_b(m) = \frac{1 + 2a\dfrac{m - \frac{1}{2}(M_{max} + M_{min})}{M_{max} - M_{min}}}{M_{max} - M_{min}} \tag{6.7}$$

where the parameter a is proportional to the slope of the function.

6.4 Signal Time and Angular Model

In chapter 2 the differential decay rate of the $B_s^0 \to J/\psi\phi$ decay including the S-wave component was derived. If the data had been recorded with a perfect detector, the time dependent decay rate (equation 2.54) could be directly used as $P_s(\Omega_i, t_i|\sigma_{t_i})$ in the likelihood fit. However, in a fit to real

data, two detector effects have to be taken into account: the limited detector resolution and the detector efficiency, which is a sculpting of the angular distributions due to trigger efficiency, reconstruction efficiency and selection cuts.

6.4.1 Detector Resolution

To take the limited time resolution of the decay time measurement into account, each time dependent term in the differential decay rate is smeared with the uncertainty of the decay time. Mathematically the smearing is done by a convolution of the time-dependent term with a Gaussian around zero that has a width corresponding to the decay time uncertainty. In the untagged decay rate the time dependence is expressed in form of exponentials of the heavy and light B_s^0 meson. The convolution of an exponential with a Gaussian yields

$$e^{-\Gamma t} * \frac{1}{\sqrt{2\pi}\sigma} e^{-\frac{t^2}{2\sigma^2}} = \frac{1}{2} e^{\frac{\Gamma^2\sigma^2}{2} - \Gamma t} (1 + erf\left(\frac{t}{\sqrt{2}\sigma} - \frac{\Gamma\sigma}{\sqrt{2}}\right) \tag{6.8}$$

where $\sigma = s_t\sigma_t$ and the scale factor s_t accounts for misestimation of the decay time uncertainty. In addition, the tagged decay rate contains products of time dependent exponentials and sine or cosine functions. The convolution of these terms with a Gaussian can also be done analytically and gives [73]

$$e^{-\Gamma t}\sin(\Delta M t) * \frac{1}{\sqrt{2\pi}\sigma} e^{-\frac{t^2}{2\sigma^2}} = \frac{1}{2} e^{\frac{(\Gamma^2 - \Delta M^2)\sigma^2}{2} - \Gamma t} \left(\sin(b)(1 + \Re(a)) + \cos(b)\,\Im(a)\right) \tag{6.9}$$

and

$$e^{-\Gamma t}\cos(\Delta M t) * \frac{1}{\sqrt{2\pi}\sigma} e^{-\frac{t^2}{2\sigma^2}} = \frac{1}{2} e^{\frac{(\Gamma^2 - \Delta M^2)\sigma^2}{2} - \Gamma t} \left(\cos(b)(1 + \Re(a)) - \sin(b)\,\Im(a)\right) \tag{6.10}$$

with

$$b = \Delta M(t - \Gamma\sigma^2) \qquad \text{and} \qquad a = erf(\frac{t - \Gamma\sigma^2}{\sqrt{2}\sigma} + i\frac{\Delta M\sigma}{\sqrt{2}}).$$

The calculation of the complex error function is performed numerically [74] on an event-by-event basis.

6.4.2 Angular Acceptance

The sculpting of the angular distributions through the detector is represented by the term $A(\Omega_i, p_{\mathrm{T}i})$ in the likelihood function. This angular

acceptance is treated as an angular sculpting PDF and is therefore multiplied with the time and angular part $P_s(\Omega_i, t_i|\sigma_{t_i})$. Consequently both terms have to be normalized together which is discussed in the following section. $A(\Omega_i, p_{\mathrm{T}i})$ is constructed as a four dimensional binned angular acceptance of the transversity angles and the B_s^0 meson p_T that is determined using MC events. A sample of $12 \cdot 10^6$ $B_s^0 \to J/\psi\phi$ signal events is generated with flat angular distributions. After the detector simulation, trigger chains, offline reconstruction and selection cuts, the angular distributions of the remaining events are not flat anymore and their shape depends on the p_T of the B_s^0 candidate. The acceptance in each bin is calculated as the number of remaining B_s^0 candidates over the number of generated B_s^0 mesons. The angular bins of $\cos\theta$, $\cos\psi$ and ϕ are normalized for each p_T bin and thus a four dimensional map is created used to weight the events in the signal part of the fit according to their transversity angles and p_t.

6.4.3 Normalization

Because $A(\Omega_i, p_{\mathrm{T}i})$ and $P_s(\Omega_i, t_i|\sigma_{t_i})$ both depend on the transversity angles, a normalization factor needs to be calculated for their product. The time dependent part of $P_s(\Omega_i, t_i|\sigma_{t_i})$ is independent and can be calculated analytically. The normalization over the angular part is done numerically by summing over the binned angular acceptance for the p_T of the B_s^0 candidate. For each bin the acceptance weight is multiplied with the time integrated $P_s(\Omega_i, t_i|\sigma_{t_i})$ for the central values of each angular bin interval. Since this calculation needs to be done for each event, the resulting normalization factors for the p_T bins are cached and only recalculated if the relevant parameters change during the fit procedure, to speed up the computation.

6.5 Background Time and Angles

The proper decay time of the background $P_b(t_i|\sigma_{t_i})$ has four components. A prompt peak of combinatorial background is modeled by a Gaussian around zero as it is not expected to have a significant lifetime. Two positive exponential functions represent a small fraction of longer-lived backgrounds, reconstructed from non-prompt J/ψ mesons and hadrons from the primary vertex. Events with a poor vertex resolution leading to negative decay time measurements are modeled by a negative exponential function. Again the detector resolution is taken into account by convolution with a Gaussian of

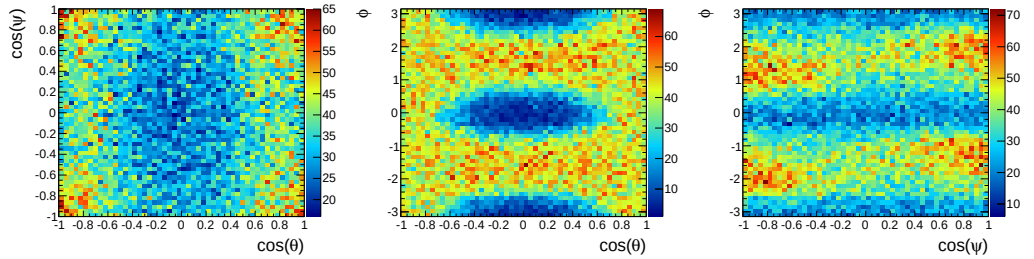

Figure 6.1: Two dimensional histograms of the transversity angles θ, ψ and ϕ for the B_s^0 sideband mass regions $5.150\,\text{GeV} < m(B_s^0) < 5.317\,\text{GeV}$ and $5.417\,\text{GeV} < m(B_s^0) < 5.650\,\text{GeV}$. While $\cos\psi$ shows only very small correlations to the other angles (left and right), there is a visible correlations between $\cos\theta$ and ϕ (middle).

the uncertainty measurement for each event. The mathematical form of the PDF modeling the background decay time is

$$P_b(t_i|\sigma_{t_i}) = \left\{ f_g + (1-f_g)\left[f_- \frac{1}{\tau_-} e^{-\frac{t}{\tau_-}} + (1-f_-)\left(f_+ \frac{1}{\tau_+} e^{-\frac{t}{\tau_+}} + (1-f_+)\frac{1}{\tau_{++}} e^{-\frac{t}{\tau_{++}}} \right) \right] \right\} * \frac{1}{\sqrt{2\pi}\sigma} e^{-\frac{t^2}{2\sigma^2}} \tag{6.11}$$

where f_g, f_- and f_+ are the relative fractions of the contributions and $\sigma = s_t\sigma_t$ is the event-by-event decay time uncertainty multiplied with the same scale factor as in the signal model.

The shape of the angular distributions of the background $P_b(\theta)$, $P_b(\psi)$ and $P_b(\phi)$ is not flat due to detector and kinematic sculpting. Two-dimensional histograms of the angles from mass sidebands are presented in figure 6.1 to visualize the correlations between the background angles. It can be seen that $\cos\psi$ is nearly uncorrelated to the $\cos\theta$ and ϕ. However, the middle plot shows a visible but small correlation between $\cos\theta$ and ϕ . In the fit model correlations between the background angles are assumed to be negligible, and thus the angular background PDF is modeled as a product of independent functions describing each of the three transversity angles. This factorization method was inspired by the CDF analysis [75]. The estimation of a systematic uncertainty due to the small correlations between $\cos\theta$ and ϕ is described in chapter 7. The following empirically determined functions were found to describe the data:

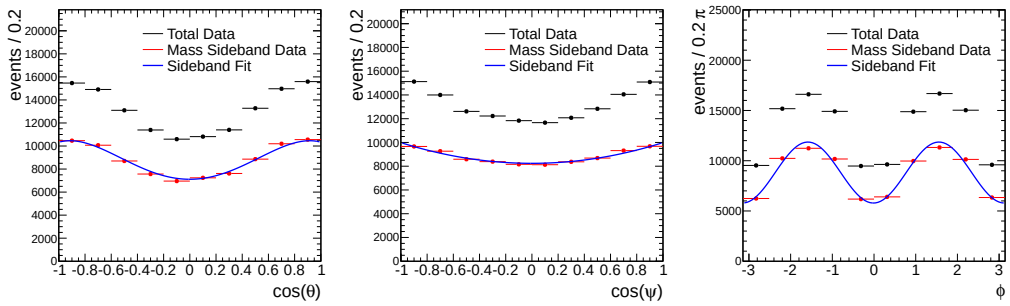

Figure 6.2: Distributions of the transversity angles $\cos\theta$, $\cos\psi$ and ϕ of the B_s^0 candidates. The total data is shown in black and the data from the mass sidebands $5.150\,\text{GeV} - 5.317\,\text{GeV}$ and $5.417\,\text{GeV} - 5.650\,\text{GeV}$ is shown in red. The blue curves represent the initial fits to the sideband distributions for each angle that was performed to determine reasonable starting values for the full likelihood fit.

$$\begin{aligned} P_b(\theta) &= \frac{1 - a_1\cos^2\theta + a_2\cos^4\theta}{2 - \frac{2}{3}a_1 + \frac{2}{5}a_2}, \\ P_b(\psi) &= \frac{1 - b_1\cos^2\psi}{2 - \frac{2}{3}b_1}, \\ P_b(\phi) &= \frac{1 + c_1\cos(2\phi + c_0)}{2\pi}. \end{aligned} \tag{6.12}$$

They are normalized for the angular ranges $-1 \leq \cos\theta \leq 1$, $-1 \leq \cos\psi \leq 1$ and $-\pi \leq \phi \leq \pi$. The initial parameters $a_{1,2}$,b_1 and $c_{0,1}$ are determined through a fit to B_s^0 mass sidebands to be used as reasonable starting values for the full likelihood fit. Figure 6.2 shows the initial fit to the angular distributions of the mass sidebands in the data sample. The parameters describing the background angles are allowed to float freely in the fit to allow for possible deviations between the background in the signal region and the background in the mass sidebands.

6.6 Time and Mass Uncertainties and p_T Dependence

Since the error distributions are different for signal and background, and the models describing the decay time and the signal mass make use of event-

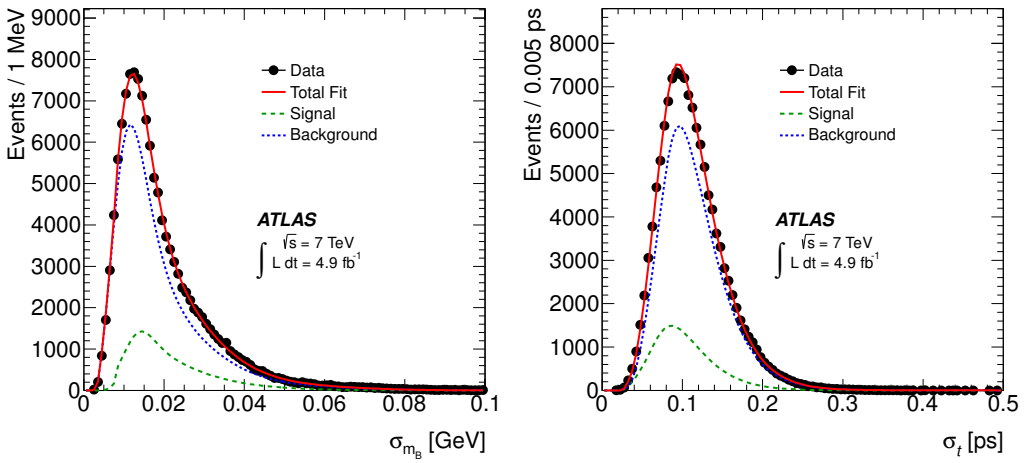

Figure 6.3: The plots show the mass (left) and lifetime (right) uncertainties. The green curve denotes the signal, the blue curve denotes the background and their sum, matching the black data points, is shown in red.

by-event errors, it is necessary to include them as separate PDFs [76]. The error PDFs, $P_s(\sigma_m)$, $P_s(\sigma_t)$, $P_b(\sigma_m)$ and $P_b(\sigma_t)$, are created in a fit to the signal and background uncertainty distributions using Gamma distribution functions

$$P(x) = \frac{x^a e^{-\frac{x}{b}}}{b^{a+1}\Gamma(a+1)}.$$

The background distributions are taken from B_s^0 mass sidebands and the signal distributions are obtained using a sideband subtraction method assuming that the mass background in the signal region can be approximated by the background in the mass sidebands of the data. Because the shape of the signal and background uncertainty distributions for the derivation of the $P_{s/b}(\sigma_{m/t})$ functions depends on the transverse momentum of the B_s^0 meson, they are determined in six p_T bins, that were chosen to reflect the p_T dependence of the detector resolution. Figure 6.3 shows the functions describing the distributions of the uncertainties of signal and background and their sum matching the data distribution in the full p_T range. As the uncertainty PDFs and the angular acceptance of the signal model depend on the B_s^0 transverse momentum, which as well shows different distributions for signal and background, additional PDFs, $P_s(p_T)$ and $P_b(p_T)$, for the p_T are included. The p_T distributions are also parameterized by Gamma functions, and the parameters are derived using the same method as for the PDFs describing the uncertainties.

6.7 Dedicated B_d^0 Background

A significant part of the background in the data sample is coming from B_d^0 reflections under the B_s^0 mass peak. As the ATLAS detector has no possibility to distinguish pions and kaons, the final state pion of the $B_d^0 \to J/\psi K^*(K\pi)$ decay and the non-resonant $B_d^0 \to J/\psi K\pi$ decay could be identified as a kaon. These misreconstructed events are called B_d^0 reflections, because if the B_d^0 is reconstructed as a B_s^0, assuming the kaon mass for both hadronic final state particles, its mass lies rather in the B_s^0 meson region than in the usual B_d^0 meson mass range. The contamination of the $B_s^0 \to J/\psi(\mu^+\mu^-)\phi(K^+K^-)$ sample with the B_d^0 reflections is treated in the likelihood function (equation 6.3) with a dedicated PDF $\mathcal{F}_{B_d^0}$. As their angular distributions differ, the two decays $B_d^0 \to J/\psi K^*(K\pi)$ and non-resonant $B_d^0 \to J/\psi K\pi$ are handled separately. Like the signal and background models, it is composed of individual PDF for the different variables:

$$\begin{aligned}\mathcal{F}_{B_d^0}(m_i, t_i, \Omega_i) =& P_{B_d^0}(m_i) \cdot P_s(\sigma_{m_i}) \cdot P_{B_d^0}(t_i|\sigma_{t_i}) \cdot P_s(\sigma_{t_i}) \\ & \cdot P_{B_d^0}(\theta) \cdot P_{B_d^0}(\psi) \cdot P_{B_d^0}(\phi) \cdot P_s(p_{\mathrm{T}i})\end{aligned} \tag{6.13}$$

The same PDFs as for the signal model are assumed for the mass and decay time uncertainties and the p_T of the B_d^0 background. Due to the incorrect mass assignment, the usually Gaussian distributed B_d^0 mass is transformed into a Landau distribution, which can be seen in figure C.1, and consequently a Landau distribution function is used as mass PDF $P_{B_d^0}(m_i)$. An exponential function smeared with event-by-event Gaussian errors models the B_d^0 decay time:

$$P_{B_d^0}(t_i|\sigma_{t_i}) = \frac{1}{\tau_d^*} e^{-\frac{t}{\tau_d^*}} * \frac{1}{\sqrt{2\pi}\sigma} e^{-\frac{(t)^2}{2\sigma^2}} \tag{6.14}$$

where $\sigma = s_t\sigma_t$ is the per-event decay time uncertainty multiplied with the same scale factor that is used in the signal model. τ_d^* is the lifetime of the incorrectly reconstructed B_d^0 mesons, calculated as $\tau_d^* = \tau_s \dfrac{m_{B_s^0}}{m_{B_d^0}} = 1.5441\,\mathrm{ps}$, with the values quoted in [21]. The PDFs describing the transversity angles of the B_d^0 background are using similar functions as used for the modeling of the general background (equation 6.12), but with different values for the

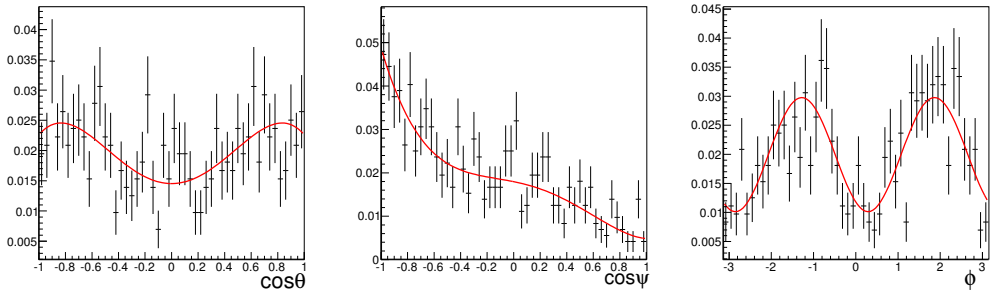

Figure 6.4: Normalized distributions of the transversity angles $\cos\theta$, $\cos\psi$ and ϕ of the B_s^0 candidates reconstructed in the $B_d^0 \to J/\psi K^*$ MC sample. The red curves represent the fits to the distributions using the functions defined in equation 6.15. The parameters of the functions are kept fix in the full likelihood fit.

parameters:

$$
\begin{aligned}
P_{B_d^0}(\theta) =& \frac{1 - a_1 \cos^2\theta + a_2 \cos^4\theta}{2 - \frac{2}{3}a_1 + \frac{2}{5}a_2} \\
P_{B_d^0}(\psi) =& \frac{1 - b_1 \cos\psi + b_2 \cos^2\psi + b_3 \cos^3\psi + b_4 \cos^4\psi}{2 + \frac{2}{3}b_2 + \frac{2}{5}p_4} \\
P_{B_d^0}(\phi) =& \frac{1 + c_1 \cos(2\phi + c_0) + c_2 \cos^2(2\phi + c_0)}{(2 + c_2)\pi}.
\end{aligned} \tag{6.15}
$$

All parameters used in the PDFs describing the mass, decay time and transversity angles of the B_d^0 reflections are determined in fits to MC simulated data and are kept fix in the full likelihood fit. Figure 6.4 shows the fits of the functions defined in equation 6.15 to the angular distributions of the $B_d^0 \to J/\psi K^*$ MC sample reconstructed as B_s^0 candidates.

The fractions of the B_d^0 background are calculated from the relative production fractions of the B_s^0 and B_d^0 mesons [21], their decay probabilities given in [21], and from their reconstruction and selection efficiencies determined from MC data. The obtained fractions relative to the signal fraction are $6.5 \pm 2.4\,\%$ for $B_d^0 \to J/\psi K^*(K\pi)$ and $4.5 \pm 2.8\,\%$ for non-resonant $B_d^0 \to J/\psi K\pi$. These fractions are fixed in the likelihood fit and the errors are used to determine possible systematic effects (see chapter 7).

6.8 Time-Dependent Muon Trigger Efficiency

The weighting factor w_i in the likelihood function is needed to account for a bias towards smaller values observed in the distribution of the muon transverse impact parameter d_0 that is caused by the muon triggers [77]. The bias affects also the B_s^0 lifetime, as the impact parameters of the muons are used in the determination of the B_s^0 decay vertex from which the lifetime is calculated. The following steps were performed to determine the weighting factor w_i:

- The tag-and-probe method is applied to J/ψ decays to calculate the trigger selection efficiency in data as a function of d_0.
- The angled $B_s^0 \to J/\psi\phi$ signal MC sample is reweighted to reproduce the observed d_0 bias.
- A single exponential lifetime fit is applied once to the initial MC sample, and once to the reweighted MC sample.
- The weighting factor is derived by comparing the two fits.

This leads to the weighting factor

$$w_i = \frac{e^{-\frac{|t_i|}{\tau_{sing}+\epsilon}}}{e^{-\frac{|t_i|}{\tau_{sing}}}} \tag{6.16}$$

where τ_{sing} is the single lifetime measured before the MC reweighting and $\epsilon = 0.013 \pm 0.004\,\text{ps}$ is the difference between the two exponential fits. The uncertainty of 0.004 ps is the precision of the tag-and-probe method and is used to assign a systematic uncertainty accounting for the time efficiency correction.

Chapter 7

Untagged $B_s^0 \to J/\psi\phi$ Analysis

In this chapter the untagged analysis, which was published in [24], is presented. Before the results of the untagged fit are shown, the specific likelihood function and the measured parameters are reviewed. Following a discussion about the considered sources of systematic uncertainty, the result is compared to measurements of the parameters by other particle physics experiments.

7.1 The Fit Model in the Untagged Analysis

In the untagged analysis each B_s^0 candidate has equal chances of being a particle or an antiparticle and consequently all terms containing the mass difference Δm_s cancel out. Therefore a simplified version of the differential decay rate is applied which is shown in appendix A.1. The simplified equations describing the untagged signal decay depend on nine physics parameters: $\Delta\Gamma_s$, Γ_s, ϕ_s, $|A_0(0)|^2$, $|A_\parallel(0)|^2$, $|A_\perp(0)|^2$, $\delta_\parallel$, $\delta_\perp$, $|A_S(0)|^2$ and δ_S. The strong phase δ_0 corresponding to the amplitude $|A_0(0)|$ has been chosen to equal zero, since only differences between the phases appear in the decay rate. Instead of the S-wave phase δ_S, the difference $\delta_\perp - \delta_S$ is used as parameter in the fit. The amplitudes are normalized to unity and thus three of the four amplitudes are fit parameters and $|A_\perp(0)|^2$ is determined using the constraint

$$|A_\perp(0)|^2 = 1 - \left(|A_0(0)|^2 + |A_\parallel(0)|^2 + |A_S(0)|^2\right).$$

In the fit the squares of the amplitudes are constrained to be positive.

In the equations of the of the untagged decay rate (table A.1), the strong phase $\delta_\perp$ appears in the terms five and six and both times it is multiplied with $\sin\phi_s$. As ϕ_s is supposed to be close to zero in the Standard Model, which was confirmed in previous measurements (see section 2.8), the untagged fit is not sensitive to $\delta_\perp$. To account for the insensitivity a constraint to the best measured value is applied by adding a term in form of a Gaussian function $P(\delta_\perp)$ to the likelihood function $\mathcal{L}$ (equation 6.3):

$$\begin{aligned}\ln\mathcal{L} = \sum_{i=1}^{N} \big\{ w_i \cdot \ln\{ f_s \cdot \mathcal{F}_s(m_i,t_i,\Omega_i) + f_s \cdot f_{B_d^0} \cdot \mathcal{F}_{B_d^0}(m_i,t_i,\Omega_i) \\ +(1 - f_s \cdot (1 + f_{B_d^0})) \cdot \mathcal{F}_{bkg}(m_i,t_i,\Omega_i)\}\big\} + \ln P(\delta_\perp)\end{aligned} \tag{7.1}$$

with

$$P(\delta_\perp) = e^{-\frac{1}{2}\frac{(\delta_\perp - \mu_{\delta_\perp})^2}{\sigma_{\delta_\perp}}}$$

At the time the untagged analysis was performed, the best measured value was [78] $\delta_\perp = \mu_{\delta_\perp} \pm \sigma_{\delta_\perp} = 2.95 \pm 0.39\,\text{rad}$.

A feature of the decay rate is, that it is invariant under certain simultaneous transformations of the parameters. In both, the tagged and untagged case, the equations are invariant under the combined parameter transformation

$$\{\phi_s, \Delta\Gamma_s, \delta_\perp, \delta_\parallel, \delta_S\} \to \{\pi - \phi_s, -\Delta\Gamma_s, \pi - \delta_\perp, -\delta_\parallel, -\delta_S\}, \tag{7.2}$$

and in addition, if there is no initial state flavor tagging, the decay rate is invariant under the transformation

$$\{\phi_s, \Delta\Gamma_s, \delta_\perp, \delta_\parallel, \delta_S\} \to \{-\phi_s, \Delta\Gamma_s, \pi - \delta_\perp, -\delta_\parallel, -\delta_S\}. \tag{7.3}$$

In combination, this leads to a fourfold ambiguity. Because a tagged measurement is performed to obtain the result in [78], which is used for the Gaussian constraint on $\delta_\perp$, only the two minima of the likelihood function, featuring a positive ϕ_s, are considered in the measurement presented here. In addition, $\Delta\Gamma_s$ was determined to be positive in another measurement by LHCb [79], and therefore out of the four ambiguous solutions, only one relevant solution remains.

In total, the maximum likelihood fit of the untagged measurement contains 24 free parameters. In addition to the already mentioned eight physics parameters, there are the parameters describing the mass distribution of the B_s^0 candidates, the parameters describing the decay time and angular distributions of the background, the B_s^0 signal fraction and the two scale factors for mass uncertainty and decay time uncertainty.

Table 7.1: Fitted values for the parameters of interest and their statistical uncertainties.

Parameter	Value	Statistical Uncertainty
ϕ_s [rad]	0.22	0.41
$\Delta\Gamma_s$ [ps^{-1}]	0.053	0.021
Γ_s [ps^{-1}]	0.677	0.007
$\lvert A_0(0)\rvert^2$	0.528	0.006
$\lvert A_\parallel(0)\rvert^2$	0.220	0.008
$\lvert A_S(0)\rvert^2$	0.02	0.02
$\delta_\parallel$ [rad]		[3.01 − 3.27]

7.2 Results of the Untagged Fit

The values determined for the parameters $\Delta\Gamma_s$, Γ_s, ϕ_s, $|A_0(0)|^2$, $|A_\parallel(0)|^2$ and $|A_S(0)|^2$ in the untagged fit are shown in table 7.1. The table also contains the statistical errors of the fit, while the systematic uncertainties are discussed in the next section. Taking into account the statistical error only, the obtained values are consistent with the Standard Model predictions and with previous measurements. The S-wave amplitude $|A_S(0)|^2$ is consistent with zero. The result for $\delta_\parallel$ is given as 1 σ confidence levels as its pull distribution does not exhibit Gaussian behavior around the fitted value as will be discussed later. The resulting fitted values of all varied parameters of the untagged fit can be found in appendix A.2. The correlations between the main physics parameters of the fit are shown in table 7.2. A large correlation between $\Delta\Gamma_s$ and Γ_s of -0.617 can be observed which is expected. The untagged fit also features a correlation of 0.38 between Γ_s and ϕ_s. Correlations between the other parameters are small. A total of $22\,690 \pm 160$ signal $B_s^0 \to J/\psi K^+K^-$ decays are extracted from the fit. Projections of the fitted mass and decay time are shown in figure 7.1 and figures 7.2 and 7.3 illustrate the projections of the transversity angles in the signal mass region and in the complete mass regions.

7.3 Estimation of Systematic Uncertainties

After obtaining values for the fit parameters and their statistical uncertainties, it is necessary to assess relevant systematic uncertainties of the fit procedure. Although every known aspect of the $B_s^0 \to J\psi\phi$ decay, the de-

Table 7.2: Correlations between the parameters of interest.

	ϕ_s	$\Delta\Gamma_s$	Γ_s	$\lvert A_0(0)\rvert^2$	$\lvert A_\parallel(0)\rvert^2$	$\lvert A_S(0)\rvert^2$
ϕ_s	1.00	-0.13	0.38	-0.03	-0.04	0.02
$\Delta\Gamma_s$		1.00	-0.60	0.12	0.11	0.10
Γ_s			1.00	-0.06	-0.10	0.04
$\lvert A_0(0)\rvert^2$				1.00	-0.30	0.35
$\lvert A_\parallel(0)\rvert^2$					1.00	0.09
$\lvert A_S\rvert^2$						1.00

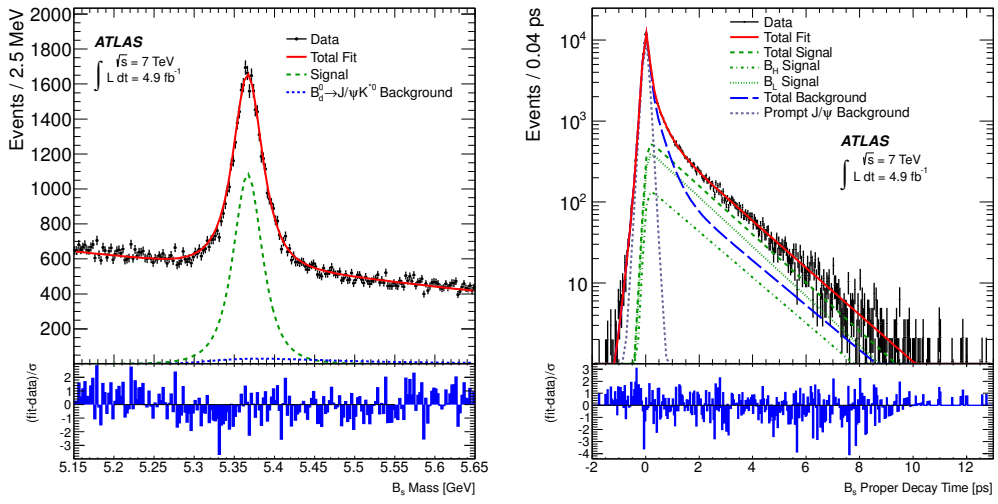

Figure 7.1: Mass (left) and proper decay time (right) projections of the B_s^0 fit. The signal components are shown in green, the background in blue, the red curves denote the total fit and the black points represent the data. The heavy and light components of the signal are shown as dotted and alternating dotted and dashed green curves in the proper decay time plot. The pull distributions at the bottom show the difference between the data and the fit value normalized to the data uncertainty.

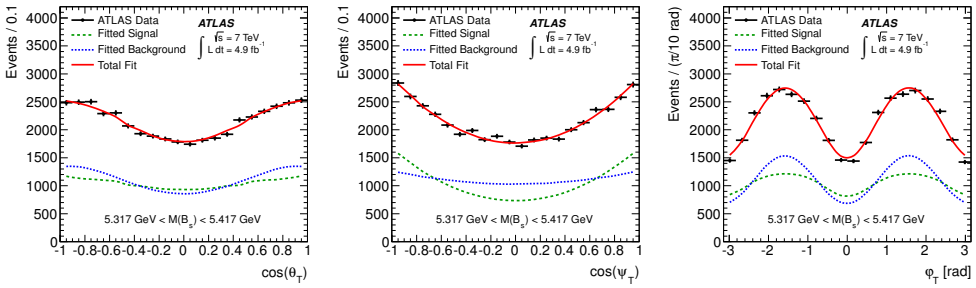

Figure 7.2: Fit projections of the transversity angles $\cos\theta$ (left), $\cos\psi$ (middle) and ϕ (right) for the B_s^0 candidates in the signal mass region $5.317\,\text{GeV} - 5.417\,\text{GeV}$.

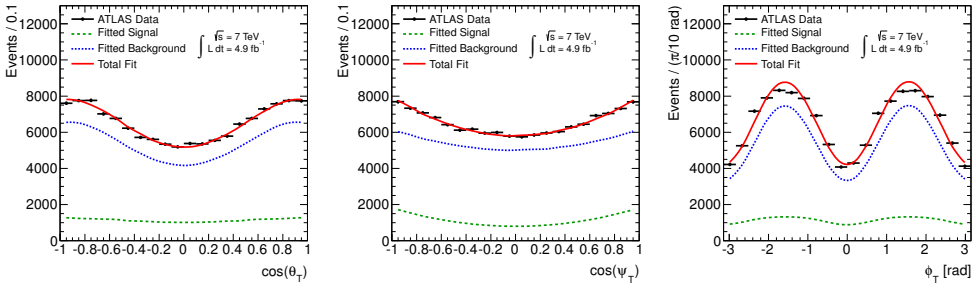

Figure 7.3: Fit projections of the transversity angles $\cos\theta$ (left), $\cos\psi$ (middle) and ϕ (right) for all B_s^0 candidates in the complete fit range $5.15\,\text{GeV} - 5.65\,\text{GeV}$.

tector and the data is included in the likelihood function, it is important to determine estimates of remaining uncertainties from assumptions made in the fit model and effects that might not be modeled perfectly. In the following sections sources of systematic uncertainties accounting for possible biases of the fit procedure are discussed.

7.3.1 Fit Model

To investigate a possible bias in the fit procedure via pull distributions and to estimate uncertainties of the fit model, pseudo-experiments are generated and fitted afterwards. For the generation of pseudo-experiments the rejection sampling method is applied. Rejection sampling is a technique to generate random numbers according to a given density function $f(x)$. It is based on the fact that sampling from the region below the graph of $f(x)$ is equivalent to sampling directly from $f(x)$. To do this another density $g(x)$ is considered that complies the condition $f(x) < M \cdot g(x)$ where $M > 1$ is an appropriate bound on $\frac{f(x)}{g(x)}$. The rejection sampling algorithm then works in the following way:

- sample x from $g(x)$,
- sample u from the uniform distribution over the interval $[0,\ 1]$,
- accept x as a realization of $f(x)$ if $u < \frac{f(x)}{M \cdot g(x)}$ holds,
- reject x and start from the beginning if the condition does not hold.

To produce pseudo-experiments for the $B_s^0 \to J/\psi\phi$ analysis, each of the variables is generated directly from the corresponding PDF in the fit model. For example to generate the mass of a signal event, $f(x)$ corresponds to $P_s(m|\sigma_m)$ (equation 6.6). For $g(x)$ a uniform distribution over the mass range of the real data is used. The product of $M \cdot g(x)$ corresponds to the maximum p_{max} of $P_s(m|\sigma_m)$ which is in this case the height of the Gaussian. In this case the mass uncertainty has to be generated before the mass, because the shape of $P_s(m|\sigma_m)$ depends on the mass uncertainty of the B_s^0 candidate. The mass for a signal B_s^0 candidate is generated as follows:

- randomly choose a mass m_i from the real data mass interval $[5.15\,\text{GeV},\ 5.65\,\text{GeV}]$,
- sample u from the uniform distribution over the interval $[0,\ 1]$,

- accept m_i as mass of a signal candidate if $u < \frac{P_s(m_i|\sigma_{m_i})}{p_{max}}$,
- if the condition does not hold, reject m_i and restart with the sampling steps.

The other variables of the B_s^0 candidates are generated in the same manner using the corresponding PDFs defined in chapter 6. 131×10^3 events are generated for each pseudo-experiment which is the same number as there are B_s^0 candidates in the real data sample. The parameters in the PDFs are set to the values that were obtained in the maximum likelihood fit. To correctly describe dependencies between the variables incorporated in the fit model, it is important to generate the variables in the proper order. This can be seen in the example above where the mass uncertainty needs to be generated before the mass. In the first step the fitted signal fraction is used to randomly decide whether a signal or background event is generated. The dedicated B_d^0 background, discussed in section 6.7, is not generated and consequently not included in the fit to pseudo-experiments. The reason for this is that the number of these background events in the data is very small and all parameters describing this background are not varied but kept fix in the fit. The first variable to be generated from the signal and background PDFs is the transverse momentum. Taking into account the generated p_T, the mass uncertainty and the time uncertainty are generated from the corresponding PDFs ($P_s(\sigma_m)$, $P_s(\sigma_t)$, $P_b(\sigma_m)$, $P_b(\sigma_t)$). Using the generated errors, the mass, the lifetime and the transversity angles of signal and background are generated according to their PDFs in the fit model. In case of the signal times and angles the normalized product of $P_s(\Omega_i, t_i|\sigma_{t_i})$ and $A(\Omega_i, p_{\mathrm{T}i})$ is used in the generation. As the maximum value of this function is not trivial to determine, the function was evaluated for all data events and 10^8 pseudo events. The maximum value obtained multiplied by two was used as p_{max} in the pseudo-experiment generation. Normalized distributions of the variables of an exemplary pseudo-experiment and the data sample are shown in figure 7.4.

To determine if the fit procedure is biased, 1000 pseudo-experiments are generated and fitted with the default fit model described in chapter 6. For each parameter and pseudo-experiment the pull is calculated as

$$\frac{fitted\ value - generated\ value}{fitted\ error} \tag{7.4}$$

and filled into a histogram. These distributions are fitted with a Gaussian as one can see in figure 7.5. An unbiased fit procedure would show Gaussian

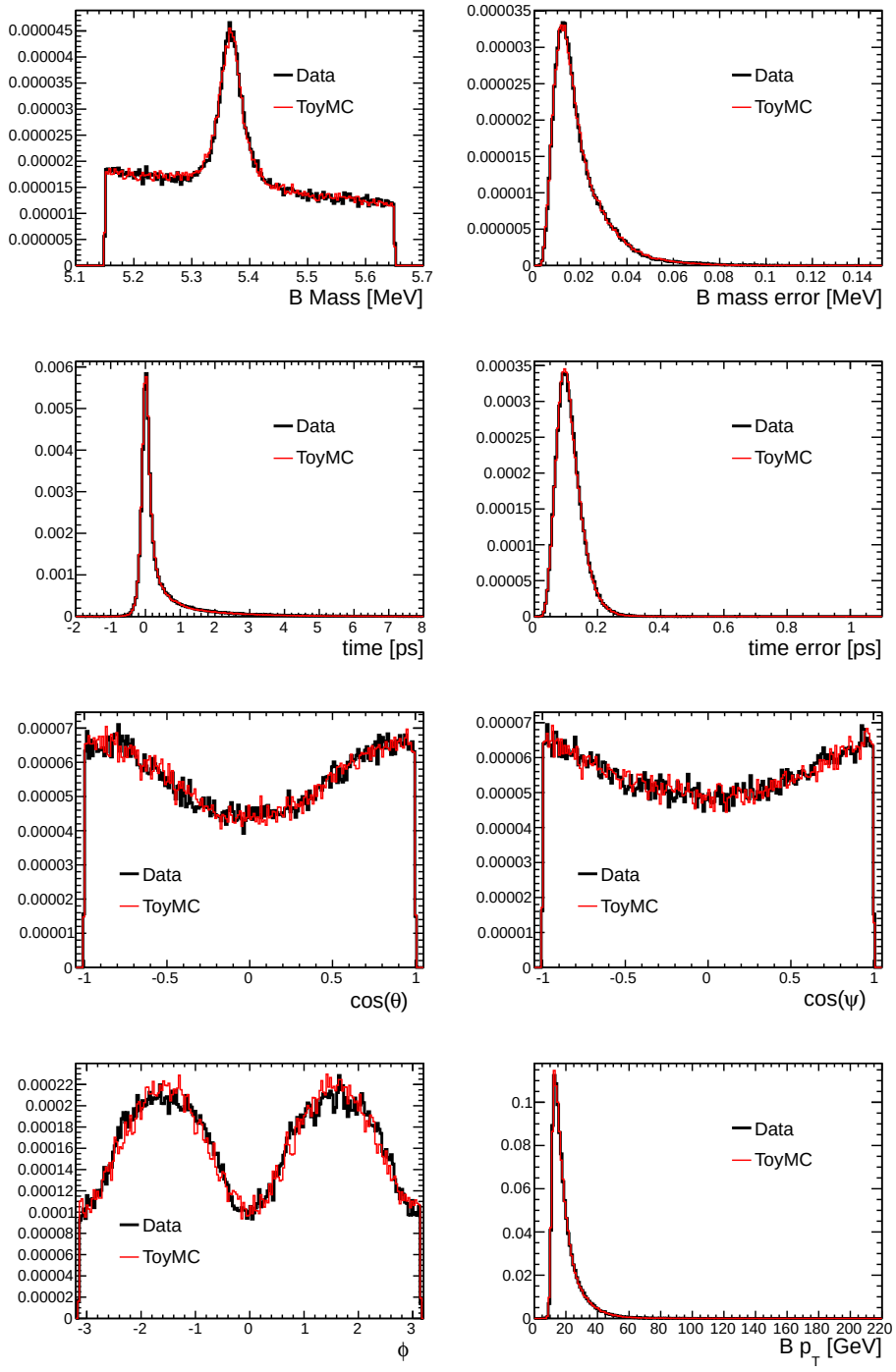

Figure 7.4: Normalized distributions of the B_s^0 candidate input variables for the fit: mass, mass uncertainty, decay time, decay time uncertainty, transversity angles $\cos\theta$, $\cos\psi$ and ϕ and the transverse momentum p_T. The real data is represented in black and an exemplary pseudo-experiment is shown in red.

distributed parameters around zero with a sigma of one and thus confirm that the statistical uncertainties are estimated correctly in the fit. The pull of $\Delta\Gamma_s$ has a bias of 0.32 and the $\delta_\perp - \delta_S$ pull distribution shows a shift of -0.26. For both parameters the residual distributions from the pseudo-experiment fits are shown in figure 7.6. The difference between the fitted and the generated value, without the normalization over the uncertainty, is called the residual. It can be seen that the residual distribution of $\Delta\Gamma_s$ shows the expected peak at zero and another peak that is shifted by ~ 0.015 and overlaps with the first peak. The bias could however not been tracked down to a problem in the fit model and it was included as systematic uncertainty of the default fit model by multiplying the bias with the statistical uncertainty of the corresponding fit value. The residual distribution of $\delta_\perp - \delta_S$ in figure 7.6 shows that the mean is shifted to the negative side from zero by approximately the generated fit value of ~ 0.03. The reason for this is that the generated value for $\delta_\perp - \delta_S$ is very close to the symmetry point at zero. This means that a mirrored second solution of the likelihood function would be $-(\delta_\perp - \delta_S)$. As the two solutions are very close to each other, the fit is not able to distinguish between them and as a consequence returns the value of the symmetry point. The plots showing the pull distributions for all other parameters in figure 7.5 are in agreement with an unbiased fit.

Figure 7.7 illustrates the pull distributions of the strong phases $\delta_\parallel$ and $\delta_\perp$. Because $\delta_\parallel$ shows non Gaussian behavior, the result for this parameter is expressed as a 1σ confidence interval of [3.01, 3.27]rad. The residual distribution of $\delta_\parallel$ presented in the right plot of figure 7.6 shows the same behavior. Most of the fits to pseudo-experiments find the generated value, but the residual distribution shows also a smaller peak at ~ -0.3. The generated value of $\delta_\parallel$ is 3.14 which coincides with the symmetry point at π. This does however not explain the second peak in the pull and residual distributions and therefore the result for $\delta_\parallel$ is given as 1 σ confidence interval. The pull distribution of $\delta_\perp$ has the form of a very narrow Gaussian which is a result of the applied Gaussian constraint (see section 7.1) in the likelihood function.

To estimate systematic uncertainties of possible incorrect or imprecise parameterizations used in the likelihood function, pseudo-experiments are generated using a variation of the PDFs and are afterwards fitted with the default fit model. The systematic uncertainty is given by the difference between the mean fit result of 1000 pseudo-experiments generated with the default fit model and the mean fit result of 1000 pseudo-experiments generated with an alternative PDF. The mean is determined in a Gaussian fit to the fit result distribution of the pseudo-experiments which is shown in figure 7.8 for the default fit model. To deal with the ambiguities of $\Delta\Gamma$

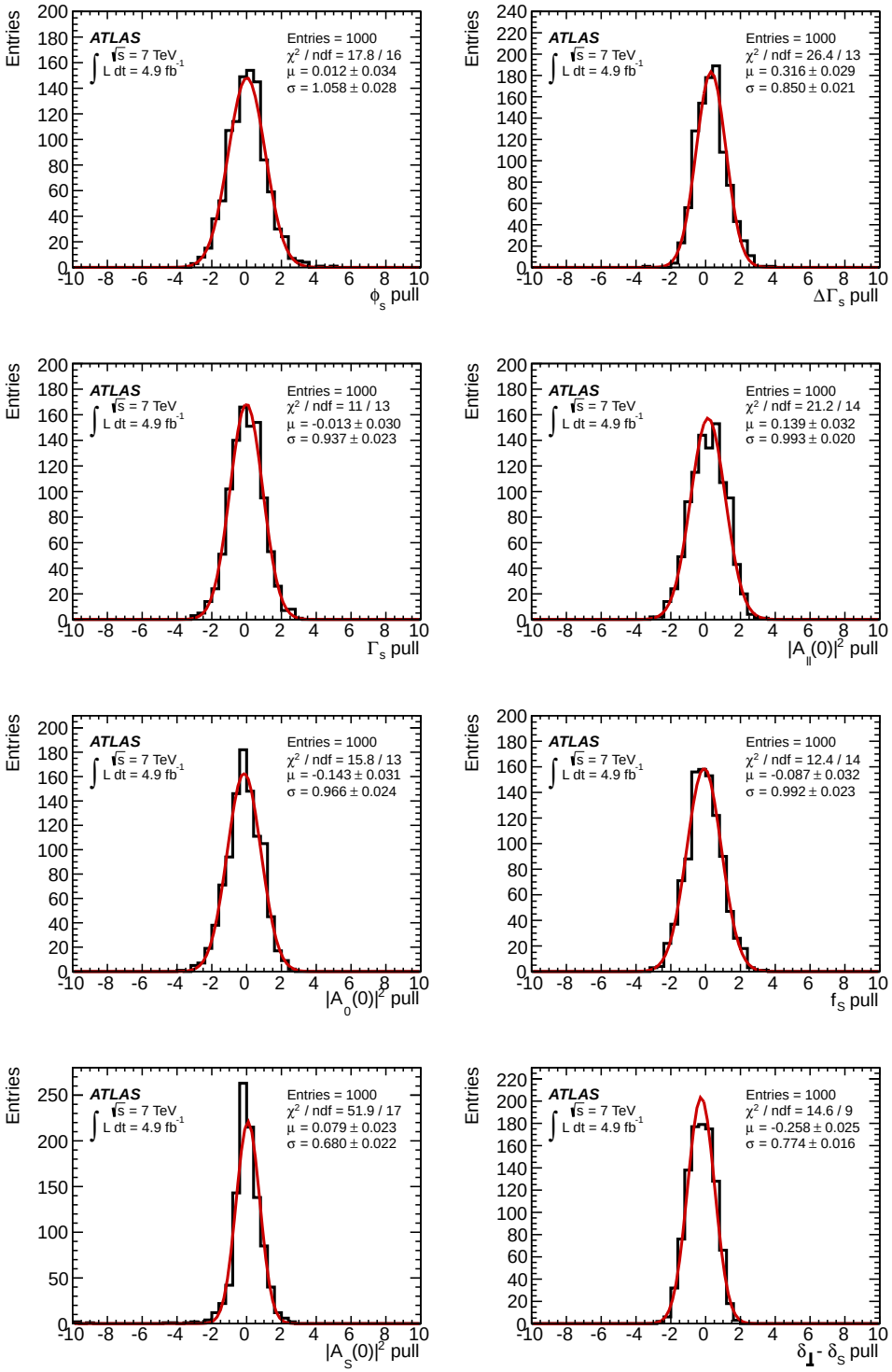

Figure 7.5: Pull distributions of the untagged fit for the of the main parameters are shown in black. They are fitted with Gaussian functions (red).

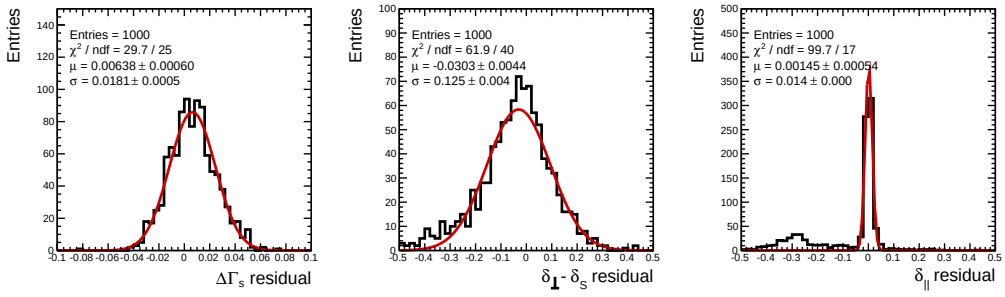

Figure 7.6: Residuals of $\Delta\Gamma_s$ (left), $\delta_\perp - \delta_S$ (middle) and $\delta_\parallel$ (right) from fits to 1000 pseudo-experiments generated with the untagged fit model.

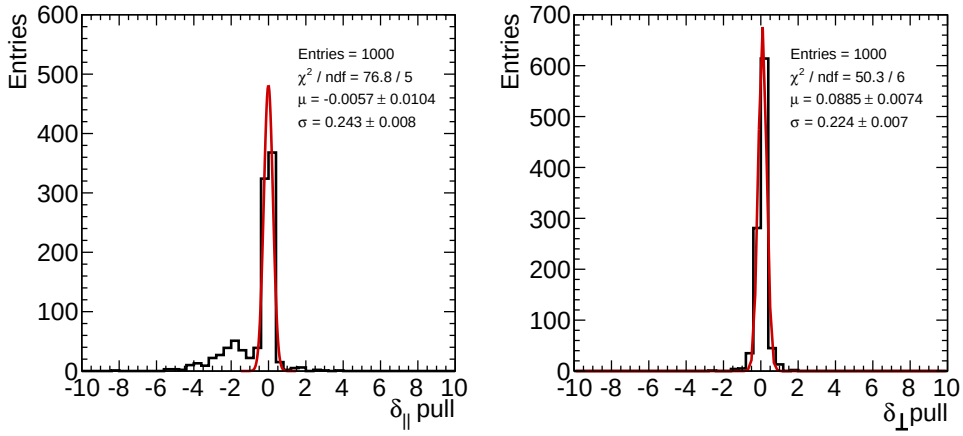

Figure 7.7: Pull distributions of 1000 pseudo-experiments generated with the untagged fit model for the strong phases $\delta_\parallel$ (left) and $\delta_\perp$ (right). Gaussian fits to the distributions are shown in red.

Table 7.3: Summary of the mean fit values for the parameters of interest fitted in 1000 pseudo-experiments that were generated using different fit models.

Model	ϕ_s[rad]	$\Delta\Gamma_s$[ps^{-1}]	Γ_s[ps^{-1}]	$\lvert A_\parallel(0)\rvert^2$	$\lvert A_0(0)\rvert^2$	$\lvert A_S(0)\rvert^2$
Default model	0.226	0.0572	0.677	0.221	0.528	0.0202
Signal mass model	0.242	0.0565	0.677	0.221	0.527	0.0186
Background mass model	0.249	0.0579	0.675	0.222	0.528	0.021
Resolution model	0.224	0.0585	0.677	0.221	0.528	0.0203
Background lifetime model	0.236	0.0586	0.676	0.222	0.528	0.0207
Background angles model	0.165	0.0633	0.678	0.215	0.535	0.0342

which is symmetric about zero, the fitted $\Delta\Gamma$ value as well as $(-1) \times \Delta\Gamma$ is filled into the histogram and the distribution is fitted with a function consisting of two symmetric Gaussians. The S-wave amplitude $|A_S(0)|^2$ is expected to be close to zero but, since it is also constrained to be larger than zero in the fit, the negative tail of the distribution is transformed into a spike at exactly zero. The spike can be seen in the $|A_S(0)|^2$ distribution of the pseudo-experiments in all the models. As the systematic uncertainty is determined by the difference of the Gaussian mean between the default fit model and the other models, a possible effect of the constraint cancels out.

To determine systematic uncertainties of possible mis-parameterizations in the fit, five different variations of the default fit model are considered which are discussed in the following. The mean fit result for each parameter and model is summarized in table 7.3. The difference between each variation and the default fit model yields the corresponding systematic uncertainty.

Signal Mass

The default fit uses a single mass scale factor to describe the B_s^0 mass. The size of the effect of this parameterization, in case it does not truly describe the data, is tested by generating pseudo-experiments with a mass model that is composed of two Gaussian functions with the same mean but different widths. The alternative mass model is parametrized by the function:

$$f(m) = f_{\sigma_1} \frac{1}{\sigma_1\sqrt{2\pi}} e^{-\frac{(m-M)^2}{2\sigma_1^2}} + (1 - f_{\sigma_1}) \frac{1}{\sigma_2\sqrt{2\pi}} e^{-\frac{(m-M)^2}{2\sigma_2^2}}. \qquad (7.5)$$

The parameters of the alternative mass model are obtained in a mass fit to the data with the function defined above as signal mass model and a linear

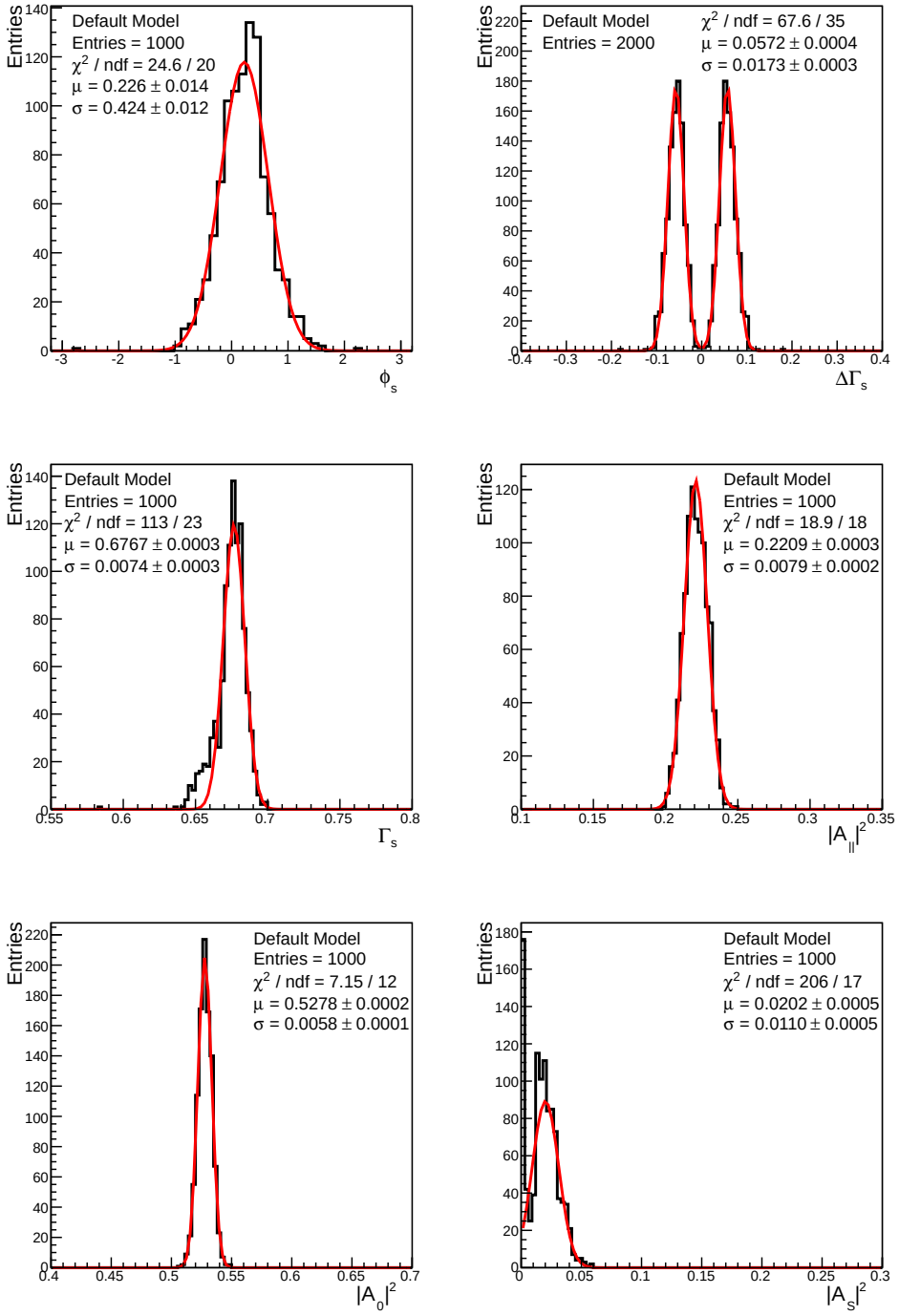

Figure 7.8: Distributions of the results from fits to 1000 pseudo-experiments generated with the default fit model (blue), fitted with Gaussian functions (red).

function describing the background mass. The values of the parameters are: $M = 5.367\,\text{GeV}$, $\sigma_{m_1} = 0.0201\,\text{GeV}$, $\sigma_2 = 0.0697\,\text{GeV}$ and $f_{\sigma_1} = 0.7528$. After the generation, each pseudo-experiment is fitted with the default model to simulate the effect of a mis-parameterization of the signal mass in the fit model. Figure 7.9 shows the distributions of fit values of the 1000 pseudo-experiments for each parameter of interest for the signal mass model variation and a Gaussian fit to each distribution.

Background Mass

The default fit uses a first order polynomial model for the background mass shape. The systematic effect of this parameterization is assessed by generating pseudo-experiments with an exponential function as alternative background mass model and fitting them using the default fit model. The alternative background mass model is described by the function

$$f(m) = \frac{\frac{1}{M_{max}-M_{min}}(1 + a \cdot e^{-\frac{m-M_c}{b}})}{1 - \frac{ab}{M_{max}-M_{min}}(e^{-\frac{M_{max}-M_{min}}{2b}} - e^{\frac{M_{max}-M_{min}}{2b}})} \tag{7.6}$$

with $M_{max} = 5.65\,\text{GeV}$, $M_{min} = 5.15\,\text{GeV}$ and $M_c = \frac{1}{2}(M_{max} + M_{min}) = 5.40\,\text{GeV}$. The parameters a and b of the function are obtained by fitting the data with a mass-lifetime fit using this exponential function as background mass model. The fitted values for the parameters are: $a = 0.6329$ and $b = 0.4387$. Figure 7.10 shows the distributions of fit values for the physics parameters of interest for pseudo-experiments generated with the alternative background mass model and fitted with the default fit model.

Lifetime Resolution

The lifetime resolution for signal events is modeled in the likelihood function by convolving each lifetime exponential term with a single Gaussian function, making use of event-by-event errors scaled by a single scale factor. For the pseudo-experiments the lifetime is generated from the decay rate without the convolution, but the generated lifetime is smeared with a Gaussian resolution function to simulate the detector resolution. The alternative lifetime resolution model uses two Gaussians with two separate scale factors:

$$R(t|\sigma_t) = f_{s_{m_1}} \cdot \frac{1}{s_{m_1}\sigma_t\sqrt{2\pi}} e^{-\frac{t^2}{2(s_{m_1}\sigma_t)^2}} + (1 - f_{s_{m_1}}) \cdot \frac{1}{s_{m_2}\sigma_t\sqrt{2\pi}} e^{-\frac{t^2}{2(s_{m_2}\sigma_t)^2}} \tag{7.7}$$

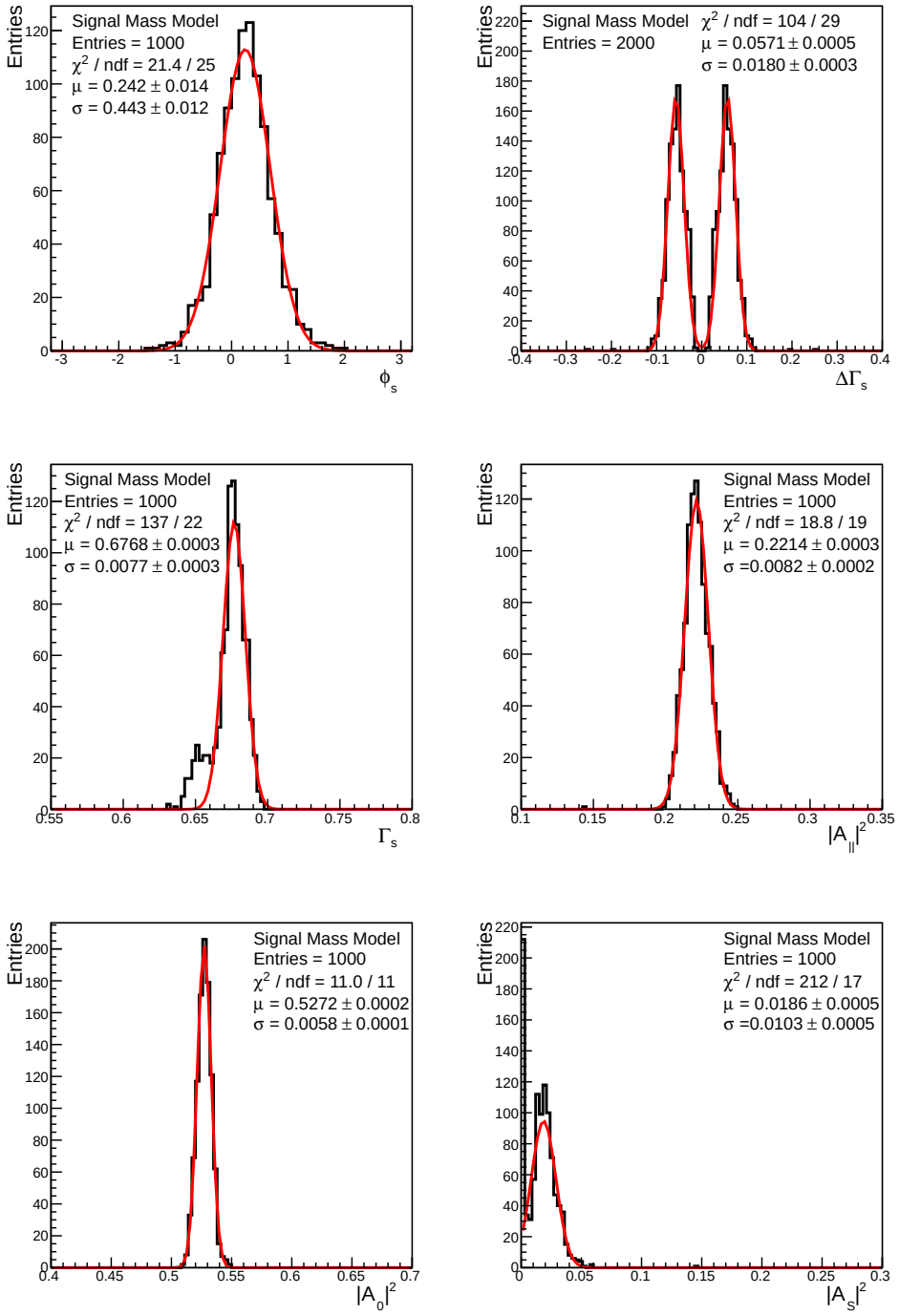

Figure 7.9: Distributions of fit values from fits to 1000 pseudo-experiments generated with an alternative signal mass model including a Gaussian fit (red).

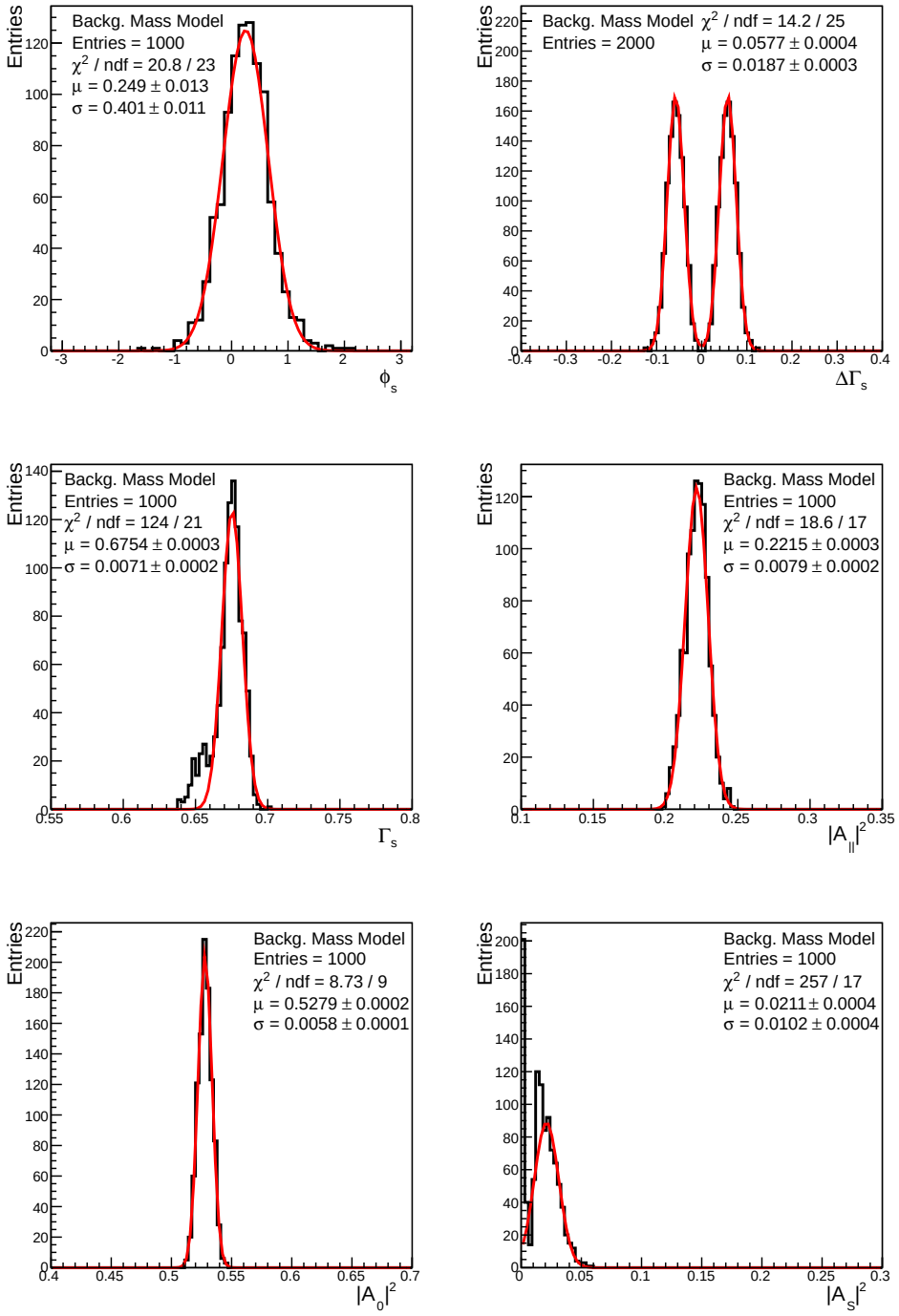

Figure 7.10: Distributions of fit values from fits to 1000 pseudo-experiments generated with an alternative background mass model, fitted with a Gaussian function (red).

The values for the alternative model are estimated from data: $f_{s_{m_1}} = 0.8$, $s_{m_1} = 0.96$ and $s_{m_2} = 1.1$. Figure 7.11 shows the distributions of fit values to pseudo-experiments generated with the alternative signal resolution model and fitted with the default model.

Background Lifetime

A data driven method is used to test the validity of the background lifetime description in the fit. Pseudo-experiments are generated using a background lifetime histogram from mass sideband data, instead of using the PDF of the default fit model, to assess the systematic uncertainty of the life time parameterization. Figure 7.12 shows the sideband lifetime histogram. The results of the fits to 1000 pseudo-experiments generated with systematically altered background lifetime and fitted with the default model are illustrated in 7.13.

Background Angles

Pseudo-experiments are generated with background angles taken from histograms from sideband data and are fitted with the default fit model to assess the systematic uncertainty to the parameterization of the background angles in the fit. To account for untreated correlations in the background angles, first the angle θ is generated, then based on this value, ϕ is selected from one of four sideband data ϕ histograms binned in θ which can be seen in figure 7.14. Figure 7.15 shows the distributions of fit values for each parameter of interest for pseudo-experiments with background angles from sideband data.

7.3.2 Trigger Efficiency

As discussed in section 6.8 the events are weighted according to equation 6.16 to correct for a lifetime bias caused by the muon triggers. The uncertainty in the parameter ϵ is used to estimate the systematic error due to this efficiency correction. The likelihood fit is performed using the value for $\epsilon \pm$ the uncertainty to calculate the weighting factor for each event. The larger deviation to the default fit result for each parameter is taken as systematic uncertainty.

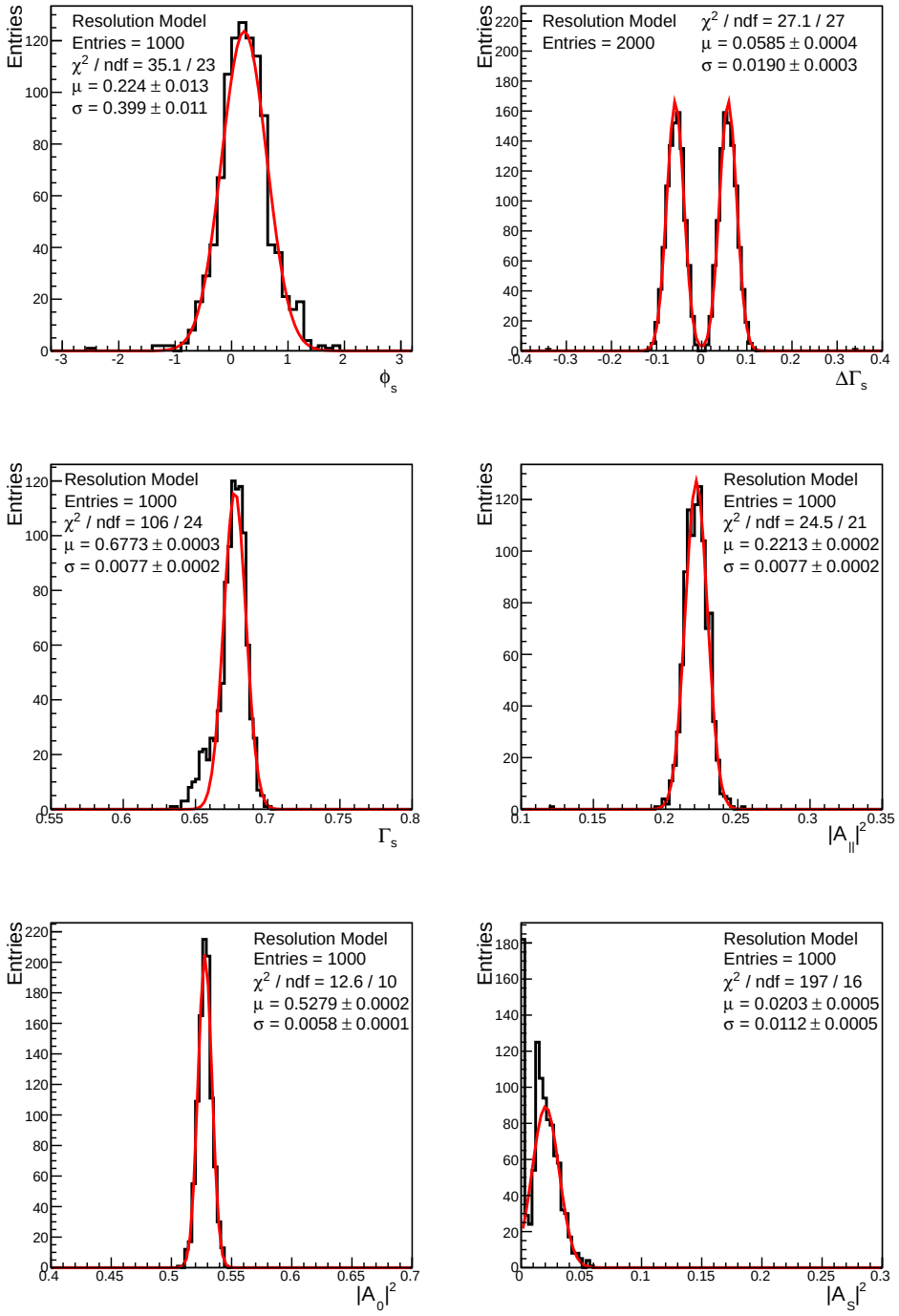

Figure 7.11: Distributions of fit values from fits to 1000 pseudo-experiments generated with an alternative signal decay time model, fitted with a Gaussian function (red).

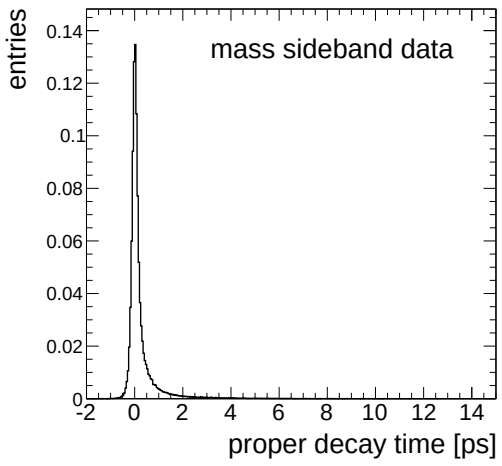

Figure 7.12: Background lifetime histogram of mass sideband data used to generate pseudo-experiments with alternative background lifetime model. The sidebands are defined as 5.150 GeV − 5.317 GeV and 5.417 GeV − 5.650 GeV.

7.3.3 Inner Detector Alignment

For the measurement described in this thesis the knowledge of the exact position of the sensitive detector elements is crucial. In order to estimate the impact on the measurement originating from residual misalignment, the effect is studied using simulated MC signal events. The most important piece of information of the particle tracks, used in the reconstruction of the decay, is the transverse impact parameter d_0. It is needed in the vertexing procedure to determine the decay and production vertex of the B_s^0 mesons and consequently in the calculation of the proper decay time. To assess the effect of residual misalignment, the d_0 performance measured in data is reflected into the MC simulation of signal $B_s^0 \to J/\psi\phi$ events.

In a first step, the impact parameter d_0 of tracks with respect to the primary vertex as a function of η and ϕ is measured in a grid with 25×25 entries. The d_0-distribution of each $\eta - \phi$ bin is fitted with a Gaussian function. The mean value of the Gaussian represents the offset and is stored in a separate histogram. For a perfectly aligned detector the d_0 distribution in each coordinate bin is expected to be centered around zero and any observed offset is a consequence of residual misalignment effects. The left 2D-histogram in figure 7.16 shows the mean value of the d_0 value obtained with data for bins in η and ϕ. This histogram is obtained during different

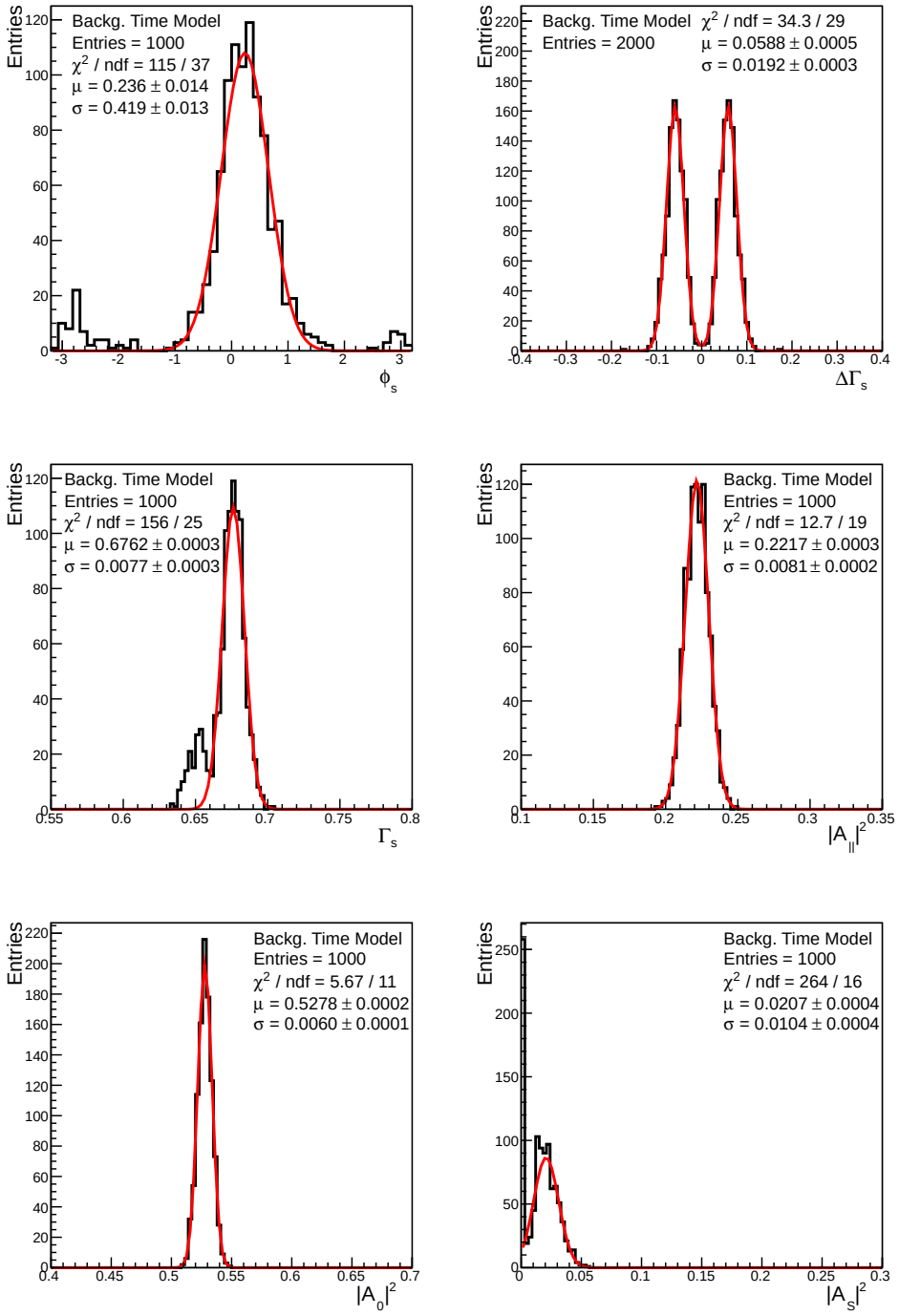

Figure 7.13: Distributions of fit values from fits to 1000 pseudo-experiments generated with an alternative background time model, fitted with a Gaussian function (red).

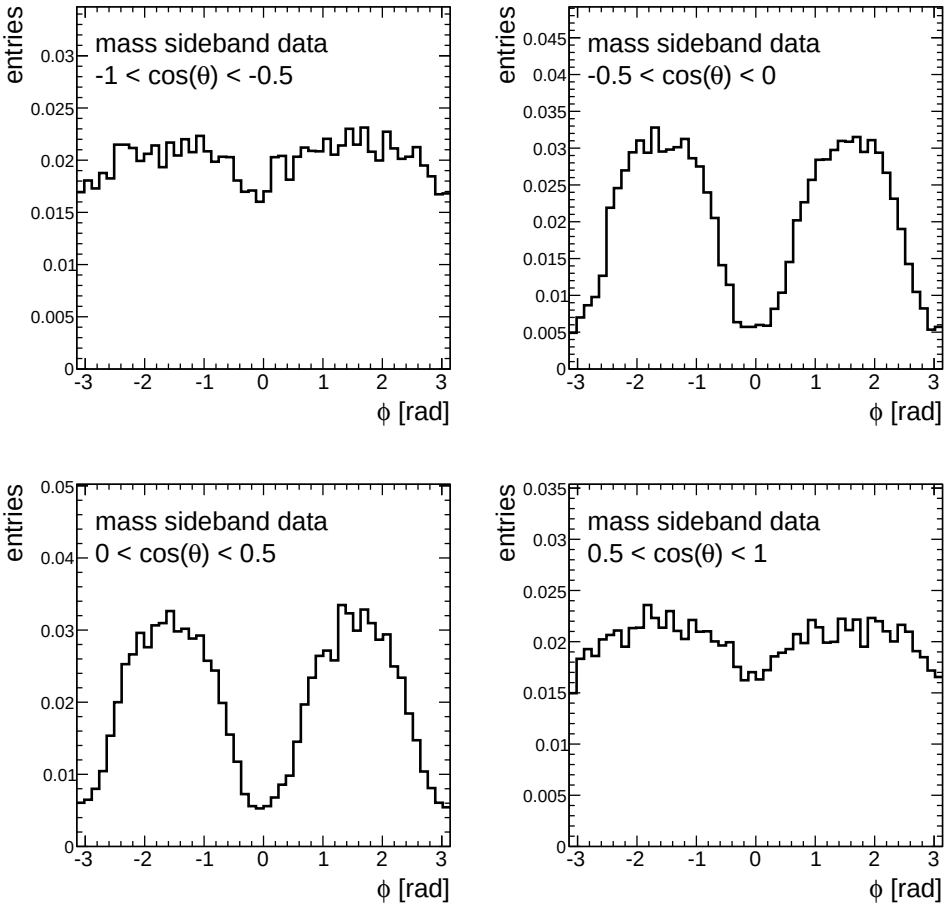

Figure 7.14: Normalized distribution of the transversity angle ϕ from mass sideband data for different intervals of $\cos\theta$. To estimate the systematic effect of not treating the correlation between $\cos\theta$ and ϕ of the background angles, pseudo-experiments are produced using these four histograms for the generation of ϕ for the background events. The mass regions $5.150\,\mathrm{GeV} - 5.317\,\mathrm{GeV}$ and $5.417\,\mathrm{GeV} - 5.650\,\mathrm{GeV}$ are used as sidebands.

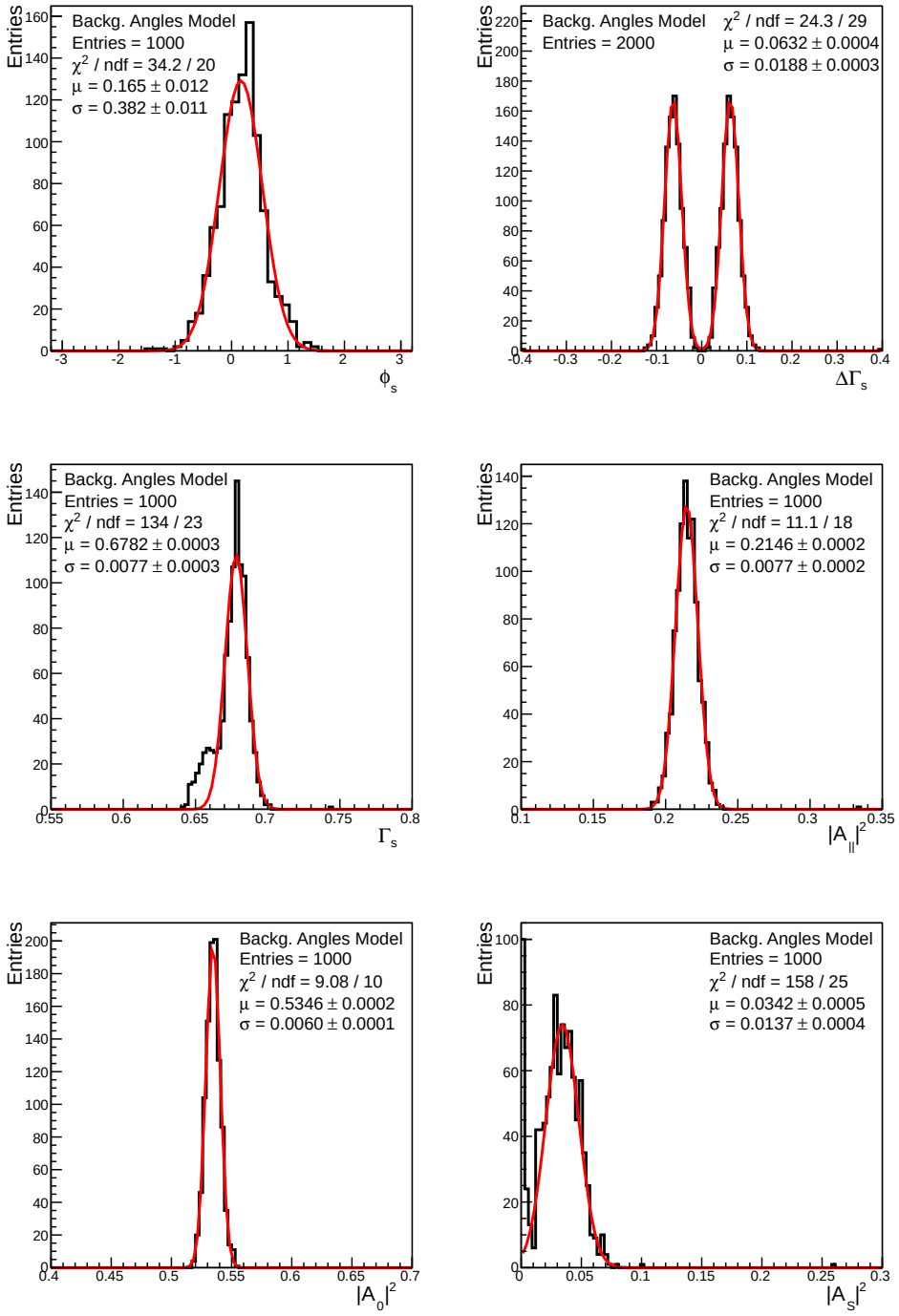

Figure 7.15: Distributions of fit values from fits to 1000 pseudo-experiments generated with an alternative model for the transversity angles, fitted with a Gaussian function (red).

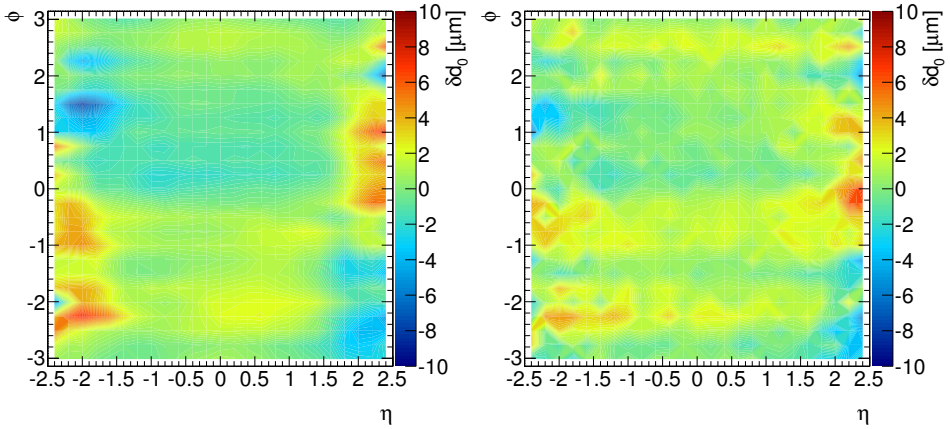

Figure 7.16: The two figures show the average d_0 offset as a function of η and ϕ measured with data reconstructed (left) and from simulated events (right). The geometry used to reconstruct the simulated events is distorted using the information obtained from data.

data taking periods, but no significant changes between the periods can be asserted, which is consistent with the stability of the inner detector during data taking.

In a second step the obtained histogram is used to introduce the d_0 offset observed in data to simulated events. This is accomplished by running the track based alignment algorithm [80], as used for the alignment of the ATLAS inner detector. In this manner the simulated tracks, constituting the input for the alignment algorithm, are distorted using the information of the d_0 histogram from data. The d_0 value of each track as a function of η and ϕ is forced to the corresponding value in the histogram. The track based alignment algorithm automatically changes the detector geometry in order to minimize the residuals obtained from the d_0 distorted track. The alignment algorithm is configured in a way to only change the geometry of the pixel detector which dominates the d_0 measurement. Each individual pixel sensor is aligned with six degrees of freedom which means that shifts and rotations in all possible directions are allowed. The right plot in figure 7.16 shows the mean d_0 value obtained from simulated events after the alignment algorithm with d_0 distorted tracks is performed. The plot of the distorted simulated events reproduces nicely the shape and size of the d_0 offset as observed in data. A detailed and complete description of this procedure is presented in [27].

The alignment algorithm produces a geometry file containing the position

and orientation of each individual inner detector module. The uncertainty quantifying residual misalignment effects is determined using the geometry file produced during the d_0 distortion in the reconstruction of simulated B_s^0 events. Two MC datasets are created: the first is reconstructed with perfect detector geometry and the second with the misaligned geometry. Both are based on the identical simulated events at generator level and thus any measured difference is originating from residual misalignment effects. The two MC datasets are fitted with the unbinned maximum likelihood fit and the difference between the obtained parameters gives the systematic uncertainty regarding residual misalignment. The fits make use of about 43000 reconstructed $B_s \to J/\psi\phi$ signal events out of a sample of 10^5 simulated signal events. The statistical uncertainties returned from the fit are therefore strongly correlated. This assumption is tested by repeating the measurement using 100 subsamples with events randomly chosen. The differences in the mean value of this distribution, obtained from the 100 subsamples, is consistent with the offset measured with the complete set of simulated events.

7.3.4 B_d^0 Reflections

The background coming from the $B_d^0 \to J/\psi K^*(K\pi)$ decay and the non-resonant $B_d^0 \to J/\psi K\pi$ decay is included in the fit model with dedicated PDFs as discussed in section 6.7. The corresponding parameters describing the mass, lifetime and angles are fixed in the fit as well as the relative fractions defining the number of these events. A systematic uncertainty for the inclusion of the B_d^0 background is determined by varying the relative fractions with their error. The value of the fractions relative to the number of signal B_s^0 events are $6.5 \pm 2.4\,\%$ for $B_d^0 \to J/\psi K^*(K\pi)$ and $4.5 \pm 2.8\,\%$ for non-resonant $B_d^0 \to J/\psi K\pi$. The maximum likelihood fit is performed with both fractions shifted up and both fractions shifted down by their error. The larger difference to the default fit with the central fraction values is used as systematic uncertainty.

7.3.5 Angular Acceptance Method

The signal model of the maximum likelihood fit makes use of a four dimensional binned acceptance correction, described in section 6.4, that is calculated using simulated events. Due to the large MC data sample, in any bin of the acceptance map the statistical error is smaller than 1 % and data

Table 7.4: Summary of systematic uncertainties assigned to physics parameters of interest.

Systematic	ϕ_s[rad]	$\Delta\Gamma_s$[ps^{-1}]	Γ_s[ps^{-1}]	$\lvert A_{\parallel}(0)\rvert^2$	$\lvert A_0(0)\rvert^2$	$\lvert A_S(0)\rvert^2$
Inner Detector alignment	0.04	< 0.001	0.001	< 0.001	< 0.001	< 0.01
Trigger efficiency	< 0.01	< 0.001	0.002	< 0.001	< 0.001	< 0.01
Default fit model	< 0.01	0.006	< 0.001	< 0.001	0.001	< 0.01
Signal mass model	0.02	0.001	0.001	0.001	0.001	< 0.01
Background mass model	0.02	0.001	0.001	0.001	0.001	< 0.01
Resolution model	< 0.01	0.001	0.001	0.001	0.001	< 0.01
Background lifetime model	0.01	0.001	0.001	0.001	< 0.001	< 0.01
Background angles model	0.06	0.006	0.002	0.006	0.007	0.02
B_d^0 contribution	0.05	< 0.001	< 0.001	< 0.001	0.005	< 0.01
Total	0.09	0.009	0.004	0.006	0.009	0.02

driven analyses show that systematic uncertainties resulting from the modeling of the detector in simulation and event reconstruction are also at the level of 1 % [81,82]. To test a possible dependence of the results on the choice of the binning, acceptance maps with various bin widths and central values were created. However a fit using these different angular acceptance maps did not have a measurable impact on the fit results. Considering all these arguments, the systematic uncertainty due to detector acceptance are found to be negligible.

7.3.6 Summary of Systematics Uncertainties

The sources of systematic uncertainties discussed above and their contribution to the uncertainty of the different fit parameter are summarized in table 7.4. It can be seen that the dominant systematic error for most of the parameters is the parameterization of the background angles. The value of the total systematic uncertainty for each parameter is calculated as the squareroot of the square sum of the individual uncertainty.

7.4 Summary of the Untagged Result and Comparison to other Experiments

The results of the untagged fit for the parameters of interest with their statistical and systematic uncertainties are shown in table 7.5. A breakdown

Table 7.5: Result of the untagged fit with statistical and systematic uncertainties.

Parameter	Value	Statistical Uncertainty	Systematic Uncertainty
ϕ_s [rad]	0.22	0.41	0.09
$\Delta\Gamma_s$ [ps^{-1}]	0.053	0.021	0.009
Γ_s [ps^{-1}]	0.677	0.007	0.004
$\lvert A_0(0)\rvert^2$	0.528	0.006	0.009
$\lvert A_\parallel(0)\rvert^2$	0.220	0.008	0.006
$\lvert A_S(0)\rvert^2$	0.02	0.02	0.02

of the fit results for all parameters can be found in appendix A.2. ϕ_s is within the errors consistent with the Standard Model value of -0.037 ± 0.002 rad. The fitted value for $\Delta\Gamma_s$ is a little bit lower than the Standard Model prediction ($\Delta\Gamma_s = 0.087 \pm 0.021\,\text{ps}^{-1}$) but also agrees within 1.5 σ, where $\sigma = \sqrt{\sigma_{stat}^2 + \sigma_{syst}^2}$. The value for Γ_s extracted from the fit corresponds to a mean B_s^0 meson lifetime of $\tau_{B_s} = 1.477 \pm 0.015(stat.) \pm 0.009(syst.)$ps which is in agreement with the world average value of 1.466 ± 0.031 ps [21]. The contribution of the S-wave decays $B_s^0 \to J/\psi f_0$ and $B_s^0 \to J/\psi K^+K^-$ is $|A_S(0)|^2 = 0.02 \pm 0.02(stat.) \pm 0.02(syst.)$ and thus consistent with zero.

Figure 7.17 shows the contour plot in the $\phi_s - \Delta\Gamma_s$ plane for the solution not excluded by LHCb [78, 79]. The contours are calculated by performing the maximum likelihood fit for a grid of fixed ϕ_s and $\Delta\Gamma_s$ values while all other parameters are allowed to vary within their physical ranges. The plot takes only the statistical uncertainties into account but as shown in table 7.5 the systematic uncertainties are small in comparison.

A plot showing the $\Delta\Gamma_s - \Gamma_s$ plane summarizing measurements constraining the decay width difference $\Delta\Gamma_s$ and decay width Γ_s of the neutral B_s^0 system is presented in figure 7.18 [83]. Results of measurements of the $B_s \to J/\psi\phi$ decay are shown from four different experiments and overlayed with constraints from analyses of the decay channels $B_s \to J/\psi f_0$, $B_s \to K^+K^-$, $B_s \to D_s\pi$ and $B_s \to D_s\mu X$. The ellipses illustrating the results of $B_s \to J/\psi\phi$ are constructed, following the method described in [21], by summing the statistical and systematic errors in quadrature and using the correlation coefficient from the multidimensional fit, when available. All measurements are represented with 68 % confidence level in the plot. The figure illustrates that the measurements in the different channels all yield results in the same region of the phase space, which coincides quite well with

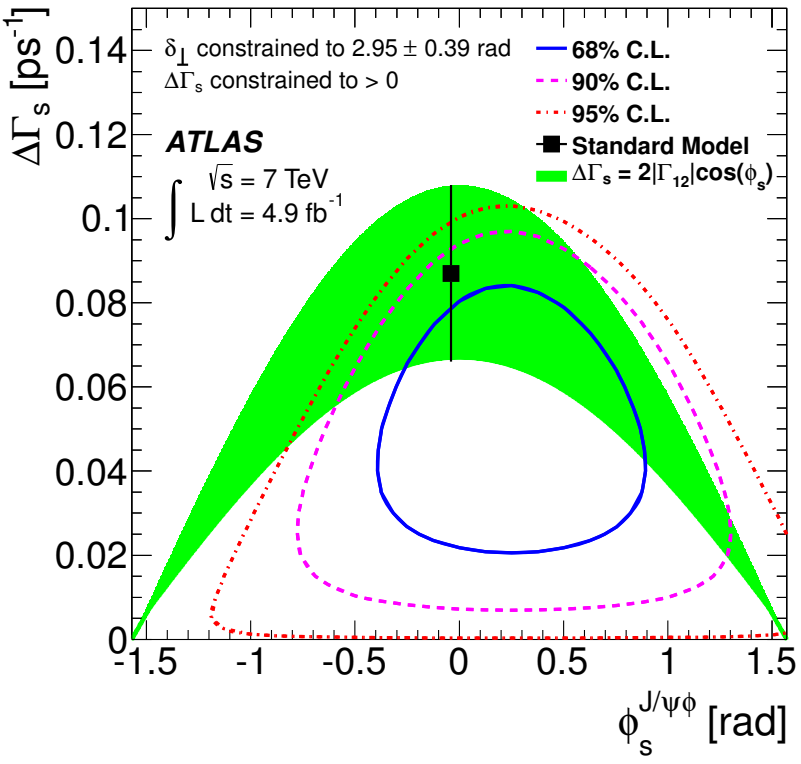

Figure 7.17: Likelihood contours in the $\phi_s - \Delta\Gamma_s$ plane. Three contours are shown for the 68 % (blue), 90 % (dashed magenta) and 95 % (red dotted) confidence intervals which are calculated taking only the statistical errors into account. The green band is the theoretical prediction for mixing induced CP violation (equation 2.32). The black point marks the Standard Model value [22, 55]. Only one of the four ambiguous solutions is shown because the other three are excluded by LHCb measurements [78, 79].

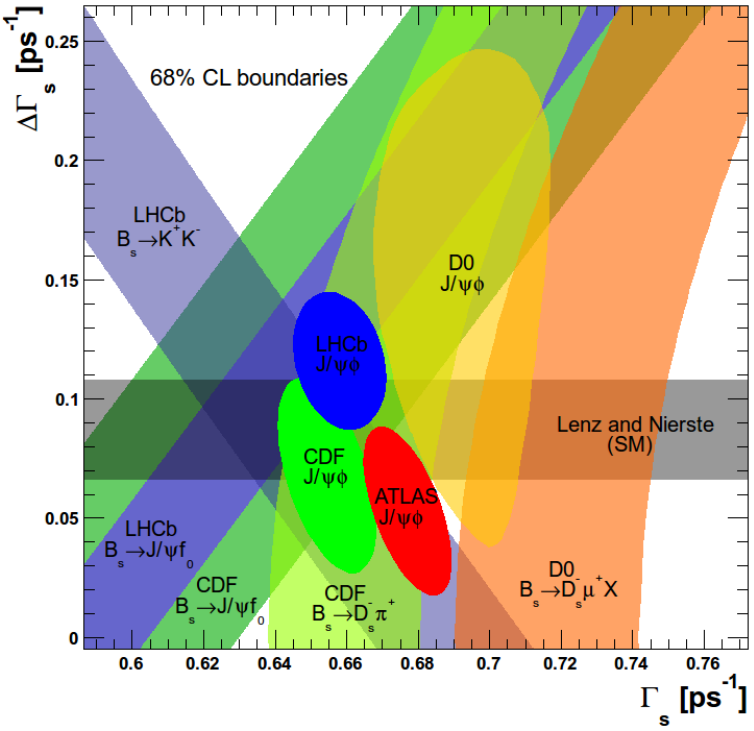

Figure 7.18: Experimental measurements and SM prediction for $\Delta\Gamma_s$ vs. Γ_s, with 68% CL boundaries. The ellipses are from $B_s \to J/\psi\phi$ studies: ATLAS [24] (red), LHCb [84] (blue), CDF [56] (green) and D0 [57] (yellow). The bands are from: $B_s \to J/\psi f_0$ studies by LHCb [85] and CDF [86] (assuming $\phi_s = 0$); $B_s \to K^+K^-$ study by LHCB [87] (assuming $A_{\Delta\Gamma_s} = -0.972$ [88]); $B_s \to D_s\pi$ study by CDF [89]; $B_s \to D_s\mu X$ study by D0 [90]. The grey band represents the Standard Model value predicted by Lenz and Nierste [55].

the Standard Model prediction for $\Delta\Gamma_s$. A plot showing the same results in the $\Delta\Gamma_s - \tau_s$ plane can be found in appendix C.2.

Chapter 8

Tagged Analysis

In this chapter the tagged analysis of the $B_s^0 \to J/\psi\phi$ decay with the ATLAS detector is presented [25]. The changes in the likelihood function compared to the untagged fit are discussed, the flavor tagging methods are described and in the end, the results of the tagged fit are presented.

The likelihood function has the form of equation 6.3 as a combination of signal and background. The Gaussian constraint applied on $\delta_\perp$ in the untagged analysis (see 7) is obsolete and thus the strong phases are allowed to float freely in the fit. The signal PDF is described by

$$\begin{aligned}\mathcal{F}_s(m_i, t_i, \Omega_i, P(B|Q)) =& P_s(m_i|\sigma_{m_i}) \cdot P_s(\sigma_{m_i}) \cdot P_s(\Omega_i, t_i, P(B|Q)|\sigma_{t_i}) \\ & \cdot P_s(\sigma_{t_i}) \cdot P_s(P(B|Q)) \cdot A(\Omega_i, p_{\mathrm{T}i}) \cdot P_s(p_{\mathrm{T}i})\end{aligned} \tag{8.1}$$

where the time and angular PDF additionally depends on the tag probability $P(B|Q)$. $P(B|Q)$ is the probability that a B_s^0 candidate is a particle (and not an antiparticle) which depends on the quantity Q. Q is either the muon cone charge or the jet charge depending on which flavor tagging method is used. Both quantities will be defined later in this chapter. The tag probability enters the fit as a multiplication factor to the differential decay rate of particle and antiparticle:

$$P_s(\Omega_i, t_i, P(B|Q)|\sigma_{t_i}) \sim P(B|Q)\frac{\Gamma(B_s^0 \to J/\psi\phi)}{dt\,d\Omega} + (1 - P(B|Q))\frac{\Gamma(\bar{B}_s^0 \to J/\psi\phi)}{dt\,d\Omega} \tag{8.2}$$

The differential decay rate of B_s^0 and $\bar{B}_s^0$ are given in equations 2.55 to 2.64 and table 2.3. In the fit the tag probability is used as a conditional variable. This means that the normalization of $P_s(\Omega_i, t_i, P(B|Q)|\sigma_{t_i}) \cdot A(\Omega_i, p_{\mathrm{T}i})$ over the time and transversity angles is performed for each event with respect to the tag probability.

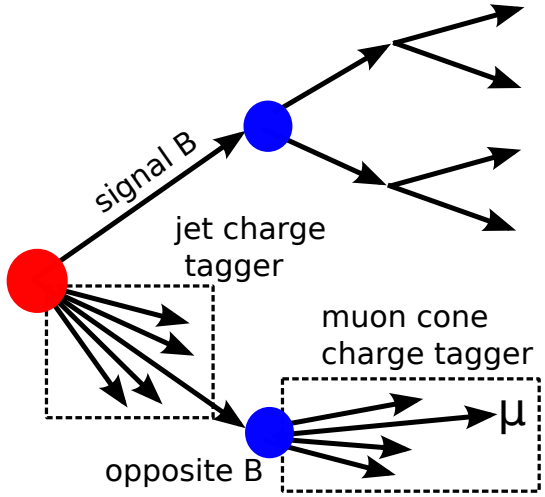

Figure 8.1: Illustration of the two opposite side tagging methods applied in the analysis: jet charge tagger and muon cone charge tagger.

Since the tag probability distributions differ for signal and background, additional terms $P_s(P(B|Q))$ and $P_b(P(B|Q))$ parameterizing the distributions are included in the likelihood function. They are constructed in the same way as it was done for the time and mass uncertainty PDFs (see section 6.6) by using the sideband subtraction method. In the following section the procedure to obtain a tag probability for the B_s^0 candidates is discussed.

8.1 Flavor Tagging

In the analysis presented here, two opposite side tagging methods are utilized. While the first method is based on semi-leptonic B decays containing a muon, the second method determines the flavor through the calculation of a jet charge. The functionality of the two methods is illustrated in figure 8.1.

The performance of a flavor tagger is characterized by two quantities: the tag efficiency ϵ_{tag} and the dilution D_{tag}. They are defined as

$$\epsilon_{tag} = \frac{N_r + N_w}{N_t} \qquad \text{and} \qquad D_{tag} = \frac{N_r - N_w}{N_r + N_w}$$

where N_r is the number or correct tagged, N_w is the number of wrong tagged and N_t is the total number of reconstructed B mesons. The dilution is related to the wrong tag fraction $w_{tag} = \frac{N_w}{N_r+N_w}$ with $D_{tag} = 1 - 2w_{tag}$. A

flavor tagger that assigns randomly decisions with a probability of 0.5, has a dilution of 0. Consequently a good flavor tagger features a high efficiency and a dilution close to 1. The two quantities are combined into the *tagging power*, also called *effective tagging efficiency*, which is defined as $\epsilon_{tag}^{eff} = \epsilon_{tag} D_{tag}^2$ and determines the statistical power of the data sample. Instead of the theoretical time-dependent CP asymmetry $\mathcal{A}_{CP}(t)$ defined in equation 2.31 the diluted asymmetry $\mathcal{A}_{obs}(t)$ for the decay into the CP final state $f = J/\psi\phi$ is observed:

$$\mathcal{A}_{obs}(t) = \frac{(1-w_{tag})d\bar{\Gamma}/dt + w_{tag}d\Gamma/dt - (1-w_{tag})d\Gamma/dt - w_{tag}d\bar{\Gamma}/dt}{(1-w_{tag})d\bar{\Gamma}/dt + w_{tag}d\Gamma/dt + (1-w_{tag})d\Gamma/dt + w_{tag}d\bar{\Gamma}/dt} \quad (8.3)$$

where Γ denotes the decay of the particle $B_s^0 \to f$ and $\bar{\Gamma}$ the decay of the antiparticle $\bar{B}_s^0 \to f$. Summing the corresponding terms leads to

$$\mathcal{A}_{obs}(t) = D_{tag}\mathcal{A}_{CP}(t). \quad (8.4)$$

For a data sample with N signal events the sensitivity to the observed CP asymmetry, and thus also to ϕ_s, is

$$\sigma(\mathcal{A}_{CP}) = \frac{1}{D_{tag}}\sigma(\mathcal{A}_{obs}) \propto \frac{1}{D_{tag}}\frac{1}{\sqrt{\epsilon_{tag}N}} = \frac{1}{\sqrt{D_{tag}^2\epsilon_{tag}N}} = \frac{1}{\sqrt{\epsilon_{tag}^{eff}N}}. \quad (8.5)$$

This means that the statistical power of the data sample scales with $\epsilon_{tag}^{eff} \cdot N$. Thus, a data sample with N signal events and tagging power ϵ_{tag}^{eff} has the same statistical power as a data sample with $\epsilon_{tag}^{eff} \cdot N$ signal events and perfect knowledge of the B_s^0 production flavor.

The performance of a flavor tagger is determined in a calibration channel, that allows the extraction of the tag from the final state particles. For the B_s^0 analysis the tagging methods are calibrated using the decay $B^\pm \to J/\psi K^\pm$ where the charge of the kaon inherits the flavor of the initial B meson. Since only opposite side tagging methods are applied, the performance of the taggers in the $B^\pm \to J/\psi K^\pm$ control channel is expected to be the same as in the $B_s^0 \to J/\psi\phi$ channel.

8.1.1 Calibration Channel $B^\pm \to J/\psi K^\pm$

The events used for the study of the flavor tagging methods, are selected from the data collected in 2011 with the ATLAS detector and they fulfill the same data quality selections as the events for the B_s^0 analysis. A detailed description of reconstruction and selection of $B^\pm$ candidates in ATLAS can

be found in [91]. The $B^{\pm}$ candidates are reconstructed from a di-muon pair forming the J/ψ meson and an additional hadronic track, assumed to be $K^{\pm}$, in the event. The subsequent criteria have to be met:

- The event contains two muons with $p_T(\mu) > 4\,\text{GeV}$ and $|\eta| < 2.5$.
- The invariant mass of the di-muon pair is in the range $2.8 < m(\mu\mu) < 3.4\,\text{GeV}$ and the χ^2 probability of the common vertex fit is at least 0.001.
- There is an additional track with $p_T > 1\,\text{GeV}$ and $|\eta| < 2.5$ in the event.
- The χ^2 probability of the B candidate vertex fit from the three tracks, with the di-muon mass constrained to the world average J/ψ mass, is at least 0.001.
- The $B^{\pm}$ candidates fulfill $L_{xy} > 0.1\,\text{mm}$ to reduce the majority of the prompt component of the combinatorial background.

The flavor tagging methods need to be studied only on the signal component of the selected $B^{\pm} \to J/\psi K^{\pm}$ data sample and therefore a sideband subtraction method is performed. The sideband subtraction removes the background contribution of the parameter distributions in the signal region using a mass fit. It assumes that the parameter distributions of the background in the signal region can be approximated by the corresponding distributions in pre-defined sideband regions. Since the momentum resolution of the inner detector varies depending on $|\eta|$, the mass fits for the sideband subtraction are performed in different bins of absolute rapidity $|y(B^{\pm})|$ of the $B^{\pm}$ mesons. The rapidity of a particle is defined as $y = \frac{1}{2}\ln\left(\frac{E+p_L}{E-p_L}\right)$ where E is the energy and p_L the longitudinal momentum component of the particle. A binned extended likelihood fit is performed in each rapidity bin. The combinatorial background is modeled by an exponential function and a hyperbolic tangent function describes the low-mass contribution from partially reconstructed $B^{\pm}$ decays. The signal peak is modeled by a Gaussian function with mean mass μ and width σ. The signal region for the sideband subtraction is defined around the fitted mean mass position with $\mu \pm 2\sigma$, while the sidebands are defined as $[\mu - 5\sigma, \mu - 3\sigma]$ and $[\mu + 3\sigma, \mu + 5\sigma]$. For each parameter distribution the sum of the two sideband areas is normalized to the corresponding background area under the signal peak. Figure 8.2 shows the $B^{\pm}$ mass including a fit in the total rapidity range. The fit yields $(194 \pm 1) \cdot 10^3$ signal decays.

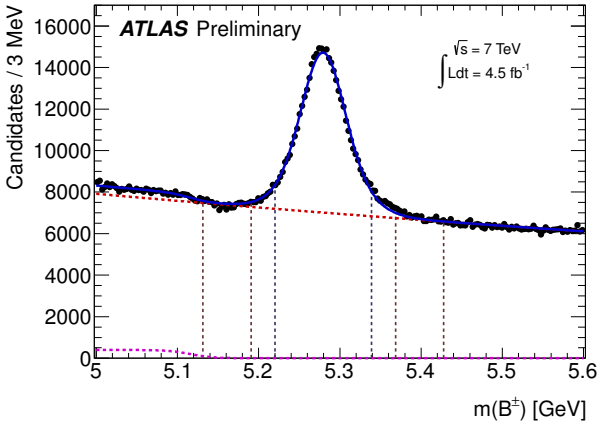

Figure 8.2: The invariant mass distribution for $B^{\pm} \to J/\psi K^{\pm}$ candidates. Included in this plot are all events passing the selection criteria. The data are shown by points, the overall result of the fit is given by the blue curve. The combinatorial background component is given by the dashed red line, and the contribution of the background from partially reconstructed decays is shown in the dotted curve. The red vertical dashed lines indicate the left and right sidebands while the blue vertical dashed lines indicate the signal region.

8.1.2 Muon Cone Charge Tagger

Using the charge of the muon of semi-leptonic B meson decays ($b \to \mu$ transition) constitutes a clean method for flavor tagging. It suffers however from a low efficiency because the probability for a B meson to decay semi-leptonically is only 10 % [21]. The power to correctly tag the signal with a muon tagger is diminished if oscillations of neutral B mesons occur on the opposite side, and it can lead to a wrong tag decision in case of a $b \to c \to \mu$ transition.

For the muon based tagger, all events passing the reconstruction and selection criteria discussed in the previous section, are searched for an additional muon that fulfills the following requirements:

- $p_T(\mu) > 2.5\,\text{GeV}$,
- $|\eta| < 2.5$,
- muon has to be a segment tagged or combined muon (see section 5.2.3),

- muon has an inner detector track that is not associated with any of the B_s^0 signal tracks,
- muon passes within longitudinal distance of $\Delta z < 5\,\text{mm}$ to the selected primary vertex.

If there is more than one muon that meets the requirements, the one with the highest transverse momentum is selected. One could now just use the charge of the muon to get a tag decision. But in the analysis presented in this thesis, a muon cone charge tagger is used to improve the tagging performance. The quantity giving the tag decision is called muon cone charge. It is a momentum-weighted charge of the muon and the tracks in a cone around the muon momentum axis. All tracks complying the following criteria are considered:

- $p_T > 0.5\,\text{GeV}$,
- $|\eta| < 2.5$,
- longitudinal distance to the selected primary vertex $\Delta z < 5\,\text{mm}$,
- tracks have to be within the cone defined by $\Delta R = \sqrt{(\Delta\eta)^2 + (\Delta\phi)^2} < 0.5$ where $\Delta\eta$ and $\Delta\phi$ is the difference between the angles of the track momentum and muon momentum.

The muon cone charge is calculated as

$$Q_\mu = \frac{\sum_i^N q_i \cdot (p_T^i)^\kappa}{\sum_i^N (p_T^i)^\kappa} \tag{8.6}$$

where q_i is the charge and p_T^i the transverse momentum of a track and N is the total number of tracks in the cone including the muon. κ is a parameter determined to optimize the tagging performance. The best performance is achieved with $\kappa = 1.1$. Since the performance of the muon cone charge tagger is different depending on the type of muon reconstruction algorithm, the muon cone charge tagger was calibrated separately for combined and segment tagged muons. Figure 8.3 shows the muon cone charge distribution for combined and segment tagged muons. The muon cone charge tagger has a tagging power of $0.15 \pm 0.02\,\%$ for segment tagged muons and $0.86 \pm 0.04\,\%$ for combined muons. The bins in the distirbutions at $Q_\mu = \pm 1$ correspond to the events where all particles in the muon cone have the same charge. For the combined muons the muon cone charge distributions of B^+ and B^- are

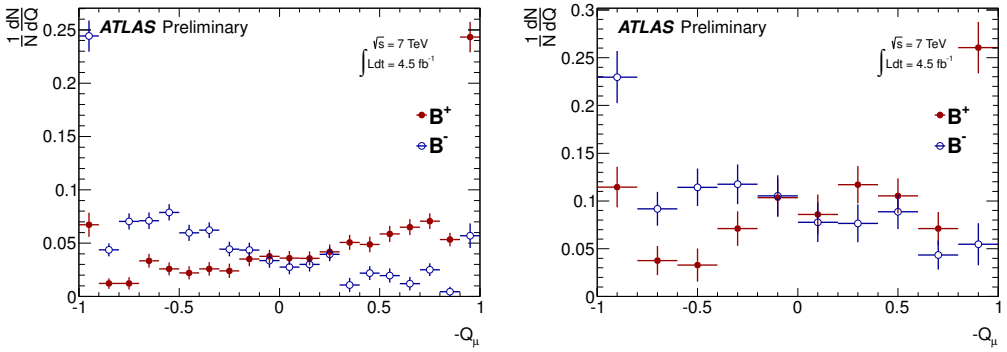

Figure 8.3: Muon cone charge distribution for $B\pm$ signal candidates for combined (left) and segment tagged (right) muons.

almost mirror images of each other. Due to the low p_T of the segment tagged muons and the lower statistics the muon cone charge distribution for B^+ is not an exact mirroring of the B^- distribution. This is also caused by the fact that the interaction of particles with the matter of the detector material is different than the one of antiparticles which results in different detection efficiencies.

8.1.3 Jet Charge Tagger

If it is not possible to derive a muon tag, due to the absence of an additional muon in the event, a jet charge tagger algorithm is used to infer a tag probability for the B_s^0 candidate. The basis for the algorithm is a b-tagged jet [92] in the event, that is composed of tracks that are originating from the same primary vertex as the signal decay. Naturally all tracks used in the reconstruction of the signal B_s^0 meson are excluded. b-jets are particle jets that arise in the formation of b-hadrons in contrast to jets produced in the hadronization process of lighter quarks. B-tagging algorithms exploit the characteristic long lifetime of b-hadrons and identify b-jets by measuring the impact parameter of the tracks in the jet or by explicit reconstruction of the secondary vertex. The jets are reconstructed using the anti-k_T jet clustering algorithm [93] with a cone size of 0.6. In the case that there is more than one jet in the event, the jet with the highest b-tag weight is used. The b-tag weight gives the probability that the jet originates from a b quark. From the tracks associated to the selected jet a jet charge is calculated as

$$Q_{jet} = \frac{\sum_i^N q_i \cdot (p_T^i)^\kappa}{\sum_i^N (p_T^i)^\kappa} \tag{8.7}$$

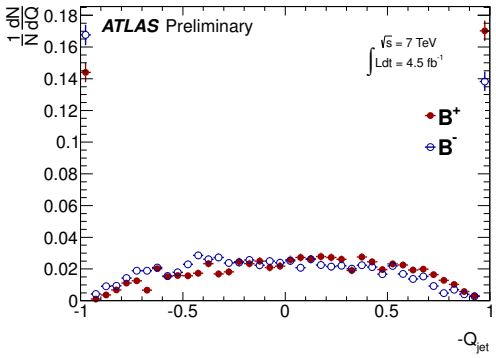

Figure 8.4: Jet charge charge distribution for $B\pm$ signal candidates.

where N is the number of tracks and q_i and p_T^i are the charge and the transverse momentum of the tracks. $\kappa = 1.1$ yields the best flavor tagging performance. The distributions of the jet charge for the b-tagged anti-k_T jets in the $B^\pm$ data sample is presented in figure 8.4. The peaks of the jet charge distributions at $Q_{jet} = \pm 1$ correspond to events where all particles in the jet have the same charge. The distributions in between the peaks are very similar for B^+ and B^- but still show a tendency to the correct tag decision.

8.1.4 Tagging in the Fit

The tagging enters the fit in form of a probability that the B_s^0 candidate is a particle or an antiparticle. The tag probability is derived from $Q_{\mu/jet}$ in the $B^\pm$ sample. The probability that the B_s^0 candidate is a particle and thus contains a $\bar{b}$ quark, given the computed muon cone or jet charge, is

$$P(B|Q) = P(\bar{b}|Q) = \frac{P(Q|\bar{b})}{P(Q|\bar{b}) + P(Q|b)} = \frac{P(Q|B^+)}{P(Q|B^+) + P(Q|B^-)}. \quad (8.8)$$

The probability for being a $\bar{B}_s^0$ is $P(\bar{B}|Q) = 1 - P(B|Q)$. The probability is calculated for each bin of figures 8.3 and 8.4 and the tagging power is defined as a sum over the bins

$$\epsilon D_{tag}^2 = \sum_i \epsilon_i (2P_i(B|Q_i) - 1)^2. \quad (8.9)$$

From the tagging power and the efficiency an effective dilution is calculated. The performance of the flavor tagging methods is shown in table 8.1.

If more than one tagging method gives a probability for a candidate, a single tag is chosen according to the hierarchy of performance: combined muon cone charge, segment tagged muon cone charge, jet charge. If none of the methods succeeds in deriving a tag, a tag probability of 0.5 is assigned to the B_s^0 candidate.

Table 8.1: Performance of the flavor tagging methods. The effective dilution is calculated from efficiency and tagging power which are determined by summing over the individual bins of the charge distribution.

Tagger	Efficiency [%]	Dilution [%]	Tagging Power [%]
segment tagged μ	1.08 ± 0.02	36.7 ± 0.7	0.15 ± 0.02
combined μ	3.37 ± 0.04	50.6 ± 0.5	0.86 ± 0.04
jet charge	27.7 ± 0.1	12.68 ± 0.06	0.45 ± 0.05
Total	32.1 ± 0.1	21.3 ± 0.08	1.45 ± 0.05

In addition to the tag probability for each B_s^0 candidate, the tagging enters the fit in form of the PDFs $P_s(P(B|Q))$ and $P_b(P(B|Q))$. The PDFs include the relative population of the tagging methods, which is shown in table 8.2, and describe the distributions of the tag probability in the B_s^0 data sample for signal and background.

The distributions consist of a continuous part and two discrete spikes for each tagging method. The spikes are caused by events where the tag charge is calculated only from tracks with the same charge resulting in $Q_{\mu/jet} = \pm 1$. For the background the shape of the distributions is determined from sidebands and for signal the sideband subtraction method is used. The relative fractions of the spikes $f_{\pm 1}$ for the three tag methods are given in table 8.3 for signal and background.

Table 8.2: the table summarizes the relative population of the tag-methods in the background and signal events. Only statistical errors are given.

Tag method	Signal	Background
combined μ	0.0372 ± 0.0023	0.0272 ± 0.0005
segment tagged μ	0.0111 ± 0.0014	0.0121 ± 0.0003
jet-charge	0.277 ± 0.007	0.254 ± 0.002
untagged	0.675 ± 0.011	0.707 ± 0.003

Table 8.3: The relative fractions of events with $Q_{\mu/jet} = \pm 1$ for signal and background and for all tag-methods. The values are given with their statistical errors.

Tag method	Signal		Background	
	f_{+1}	f_{-1}	f_{+1}	f_{-1}
combined μ	0.106 ± 0.019	0.187 ± 0.022	0.098 ± 0.006	0.108 ± 0.006
segment tagged μ	0.152 ± 0.043	0.153 ± 0.043	0.098 ± 0.009	0.095 ± 0.008
jet-charge	0.167 ± 0.010	0.164 ± 0.010	0.176 ± 0.003	0.180 ± 0.003

The continuous part is described by fourth order Chebychev polynomials for the combined muon cone charge tagger and the jet charge tagger. For the segment tagged muon cone charge tagger it is modeled by a third order polynomial. Figure 8.5 shows the data distribution and the parameterizing functions for the three tagging methods.

8.1.5 Crosscheck with $B_d^0 \to J/\psi K^*$

To validate the flavor tagging methods the oscillation frequency Δm_d of the B_d^0 system is measured using the decay $B_d^0 \to J/\psi K^*$. Unlike the B_s^0 system, the decay width difference of the B_d^0 meson and its antiparticle, the $\bar{B}_d^0$ meson, is negligible. Therefore, they decay with the same lifetime of $1.519 \pm 0.007\,\mathrm{ps}$ [21]. The world average of the mixing frequency of the oscillation between the two particles is $\Delta m_d = 0.507 \pm 0.004\,\mathrm{ps}^{-1}$ [21] and thus much smaller than in the B_s^0 system where it is $\Delta m_s = 17.69 \pm 0.08\,\mathrm{ps}^{-1}$ [21]. The reason for testing the flavor tagging in this decay channel is that although the decaying meson and the final state have no electrical charge, the flavor at decay time can be inferred from the decay products of the subsequent $K^*/\bar{K}^*$ decay. The reconstruction of the B_d^0 candidates is described in [94] and follows the same steps as for the B_s^0 candidates (see chapter 5). The only difference is that a K^* decaying to a kaon and a pion replaces the $\phi \to K^+K^-$. The invariant mass of the two tracks forming the K^* is requested to be in the interval $846\,\mathrm{MeV} - 946\,\mathrm{MeV}$ and the transverse momentum of the K^* has to be greater than $2.5\,\mathrm{GeV}$. The B_d^0 candidates are required to be in the mass interval $5.05\,\mathrm{GeV} < m(B_d^0) < 5.55\,\mathrm{GeV}$. The flavor tagging methods described in sections 8.1.2 and 8.1.3, are used to determine the flavor at production time of the B_d^0 meson. Unlike in the B_s^0 analysis, the tag probability is not needed, but only the decision if the B_d^0 candidate is tagged as a particle or an antiparticle. In the $B_d^0 \to J/\psi K^*$ decay the flavor

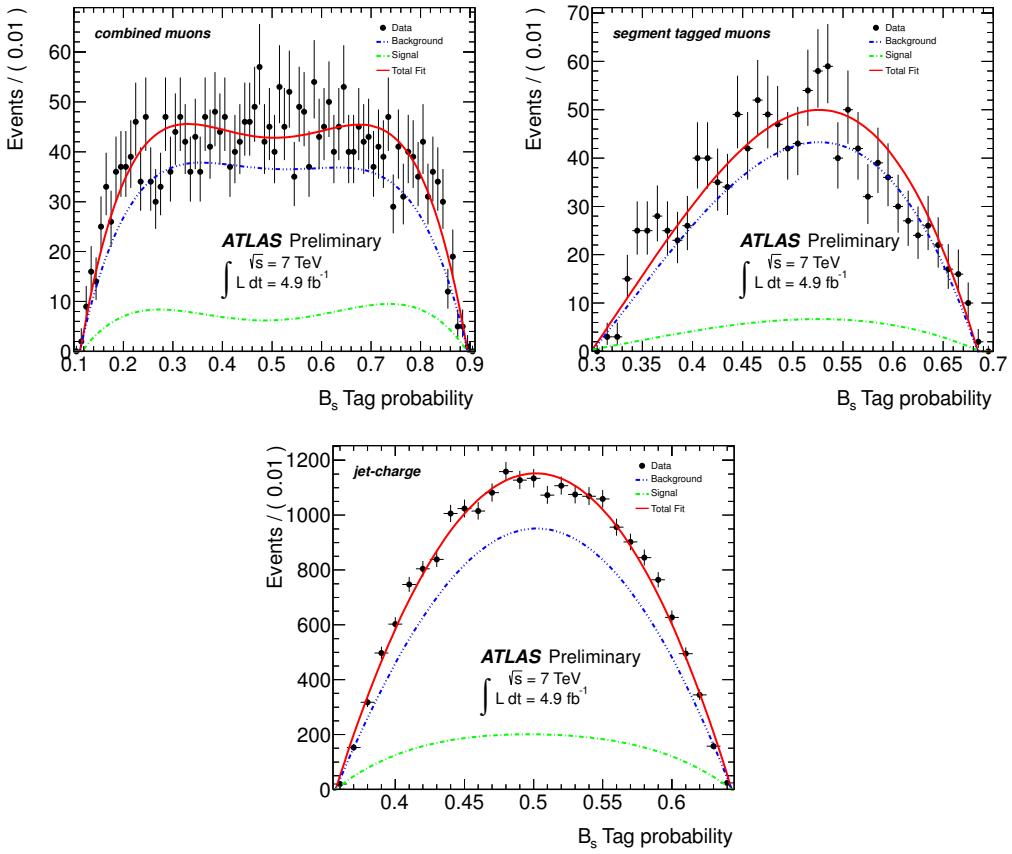

Figure 8.5: Continuous part of the tag probability for the three tagging methods: combined muons (top left), segment tagged muons (top right) and jet-charge (bottom). Black dots are data after removing spikes, blue is a fit to the sidebands, green to the signal and red is the sum of both fits.

of the B_d^0 meson at decay is derived from the combination of charged π and K in the final state: K^* decays to $K^+\pi^-$ and $\bar{K}^*$ decays to $K^-\pi^+$. As there is no possibility to distinguish between kaons and pions in ATLAS, the invariant mass of the K^* is calculated with the assumption that one particle is a kaon and the other a pion using the corresponding mass hypothesis. The calculation of the invariant mass is performed for both combinations and the one which lies in the K^* mass window is taken as the correct one. If both of the computed values for the invariant mass are in the defined K^* mass window, the flavor of the B_d^0 candidate at decay time cannot be designated. Taking also the production flavor into account, that is determined using the muon cone charge and the jet charge tagging method, the B_d^0 candidates can be divided into three types:

- **Mixed**: flavor at decay is different from production flavor.
- **Not mixed**: flavor at decay and production flavor are the same.
- **No tag**: none of the flavor tagging methods derived a tag or the flavor at decay could not be determined because $K^+\pi^-$ as well as $K^-\pi^+$ satisfy the K^* mass criteria.

To extract the oscillation frequency an unbinned maximum likelihood fit to the reconstructed B_d^0 mass and the proper decay time is performed. The signal decay time is modeled by the following function:

$$\begin{aligned} T_s(t_i|\sigma_{t_i}) =& e^{-\frac{t_i}{\tau_d}} \left(1 + k \cdot A_{B_d} \sin(\Delta m_d t_i) * \cos\delta_{B_d} - k \cdot A_{B_d} \cos(\Delta m_d t_i) \cdot \sin\delta_{B_d}\right) \\ & * \frac{1}{\sqrt{2\pi} s_t \sigma_{t_i}} e^{-\frac{t_i^2}{2(s_t\sigma_{t_i})^2}} \end{aligned} \tag{8.10}$$

where t_i and σ_{t_i} are the measured decay time and its uncertainty. A_{B_d} determines the fraction of the oscillatory term relative to the pure exponential term and δ_{B_d} is a phase offset. The factor k is given by the B_d^0 candidate type and thus k is $+1$ if the candidate is not mixed, -1 if it is mixed and zero in the case that the flavor at production or decay could not be assessed. To model the background decay time and the signal mass the same functions as for the B_s^0 analysis are used (see chapter 6). The background mass is modeled by the sum of an exponential and a constant (equation 7.6) and the PDFs parameterizing the mass and decay time uncertainties and the p_T distribution of the B_d^0 mesons are constructed in the same way as described in chapter 6.6 for the B_s^0 fit. To account for the muon trigger induced d_0

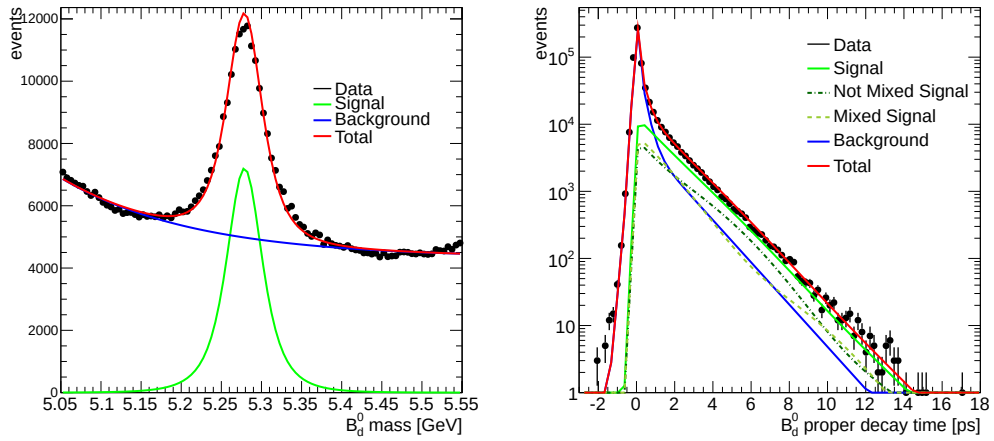

Figure 8.6: Mass (left) and proper decay time (right) projection of the mass lifetime fit to B_d^0 events using the information from the muon based flavor taggers only. Black points denote the data, the signal is shown in green, the background in blue and the total fit is shown in red. The dashed green curve denotes the mixed portion and the dotted-dashed green curve denotes the unmixed portion of the signal component.

bias, events are weighted with the same weighting factor as in the B_s^0 fit, which was discussed in section 6.8.

The fit is performed separately for the muon based taggers and the jet charge tagger. The relevant parameters extracted from the fit are the oscillation frequency Δm_d, the lifetime τ_d and the mass $m(B_d^0)$. Fit projections of mass and proper decay time are presented in figure 8.6 for the fit using the muon based tagging methods. The corresponding plots for the fit using the jet charge tagger is shown in appendix B.1.

The Oscillation of the B_d^0 mesons is visualized for the fit that uses the tag decision from the muon cone charge tagger in figure 8.7. In this figure the y axis denotes the difference between the number of mixed and unmixed decays normalized by their sum. The resulting function is calculated from the two curves of mixed and unmixed decays in figure 8.6. Table 8.4 shows the fitted values and the world average values for the parameters from [21]. In total 606 974 B_d^0 candidates were used in the fit. The number of candidates with muon tag is 24 233 and 167 939 candidates had a jet charge tag. Within the uncertainties the obtained value for Δm_d agrees with the world average which shows that the tagging methods work as intended. The measured lifetime τ_d

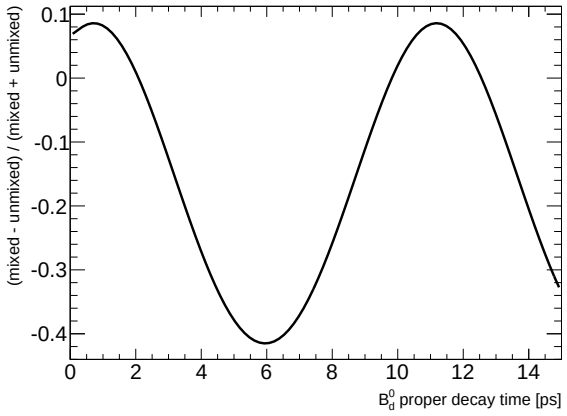

Figure 8.7: Visualization of the B_d^0 oscillation. The y axis denotes the difference between the number of mixed and unmixed decays normalized by the total number of decays at a proper decay time specified on the x axis.

Table 8.4: Fitted values for the parameters along with their statistical uncertainties. The fit was performed using the decisions of the muon based taggers and the jet charge tagger separately. The world average values are taken from [21].

Parameter	μ cone tag	Jet charge tag	World Average
Δm_d [ps^{-1}]	0.600 ± 0.097	0.58 ± 0.10	0.507 ± 0.004
τ_d [ps]	1.499 ± 0.006	1.499 ± 0.006	1.519 ± 0.007
Mass [MeV]	5278.81 ± 0.11	5278.81 ± 0.11	5279.58 ± 0.17

shows a $\sim 3.3\sigma$ shift from the world average value, and the measured mass is even $\sim 7\sigma$ away from the world average value. A possible reason for the shifts could be the that the weighting factor to correct for the d_0 bias was determined for the B_s^0 dataset and not explicitly for the B_d^0 data sample. To show that also the derived dilution and tagging power are understood a more detailed study, with a signal lifetime model taking the per-event wrong tag fraction into account, is necessary.

8.2 Systematic Uncertainties

For the tagged fit the same sources of systematic uncertainties as for the untagged analysis are considered plus an additional uncertainty arising from flavor tagging. To determine uncertainties due to inner detector alignment, trigger efficiency, B_d^0 contributions and modeling, the same methods are applied as described in chapter 7. Pseudo-experiments are used to create pull distributions and determine the systematic uncertainties due to parameterization in the fit model. A comparison between an exemplary pseudo-experiment and the data, and the fit results for the model systematics can be found in appendix B.2 and B.3.

Pull distributions for the relevant physics parameters are presented in figure 8.8. They are necessary to determine possible biases in the fit model. The pull of $\Delta\Gamma_s$ shows a small offset of 0.112 which corresponds to an uncertainty of $0.002\,\mathrm{ps}^{-1}$. Compared to the untagged analysis the bias of the $\Delta\Gamma_s$ pull has decreased by more than $\sim 60\,\%$ which is a result of the adding the flavor tagging to the fit. The pulls of the amplitudes show larger biases of up to ~ 0.4 which are caused by the normalization constraint and the fact that $|A_S(0)|^2$ is very close to zero.

While the pulls of $\delta_\perp$ show a small bias, the pull distribution of $\delta_\parallel$ is not Gaussian which can be seen in figure 8.9. The residual distribution is also shown in this figure. Similar as in the untagged analysis, a large fraction of the fits to pseudo-experiments finds the generated value of $\sim 3.136\,\mathrm{rad}$, which approximately coincides with the symmetry point at π. The residual distribution shows two more solutions with shifts of $\sim -0.3\,\mathrm{rad}$ and $\sim 0.2\,\mathrm{rad}$. Apparently, the proximity of the true value to the symmetry point causes the fit to find exactly the symmetry point or a value shifted by a little bit to the left or to the right. In comparison, LHCb quotes a value of $3.30^{+0.13}_{-0.21}\mathrm{rad(stat.)} \pm 0.08\,\mathrm{rad(syst.)}$ for $\delta_\parallel$ [59], which is within its errors in agreement with the value of 3.136 obtained in the tagged fit of the ATLAS

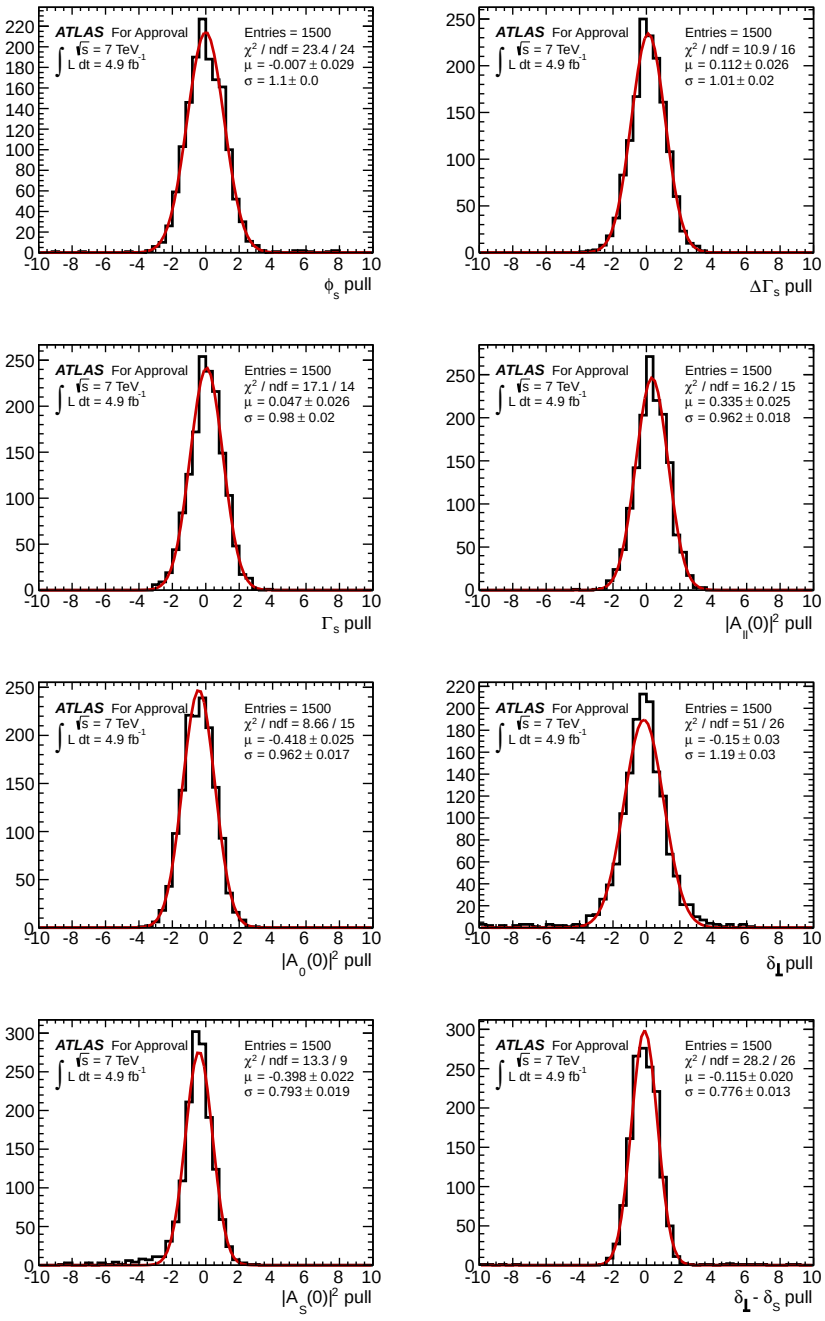

Figure 8.8: Pull distributions for parameters of interest produced in 1500 pseudo-experiments for the tagged analysis. Each distribution is fitted with a Gaussian to show possible biases in the fit and determine whether the statistical errors are correctly estimated.

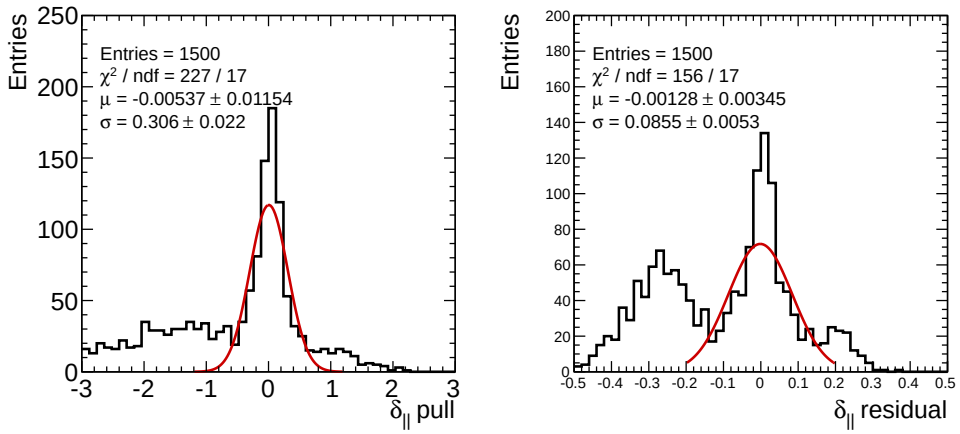

Figure 8.9: The pull distribution (left) for the strong phase $\delta_{\parallel}$ produced in 1500 pseudo-experiments for the tagged analysis does not have a Gaussian shape. The residual distribution is illustrated in the right plot. It shows a large central peak at zero that corresponds to the generated value of 3.136, and one additional smaller peak on each side of the central peak.

analysis. Due to the non-Gaussian behavior of the pull distribution the result for $\delta_{\parallel}$ is given as a 1 σ confidence interval around the value obtained from the fit.

To estimate a systematic effect from the usage of flavor tagging in the fit, the result of the default fit is compared to fits with altered tag probabilities. Varying the tag probability with its statistical uncertainty coherently up and down in each bin of the distributions yields two alternative tag probabilities for each candidate. The largest difference between the fit result with the altered tag probabilities and the default fit result is taken as systematic uncertainty for each parameter. A complete break down of the considered systematic uncertainties and their magnitude is shown in table 8.5. Flavor tagging constitutes the dominant systematic uncertainty for ϕ_s while the systematic error of all other parameters is dominated by the parameterization of the model describing the transversity angles of the background. As discussed in chapter 6 the background angles are parameterized by functions determined in fits to data from the mass sidebands. A possible alternative would be to describe the angular shape of the background in terms of spherical harmonics [95], which could reduce the corresponding systematic error in a future update of the analysis. As the systematic of the flavor tagging is related to the statistics of the $B^{\pm}$ calibration channel, the usage of the data

Table 8.5: Summary of systematic uncertainties assigned to parameters of interest.

	ϕ_s (rad)	$\Delta\Gamma_s$ (ps^{-1})	Γ_s (ps^{-1})	$\lvert A_\parallel(0)\rvert^2$	$\lvert A_0(0)\rvert^2$	$\lvert A_S(0)\rvert^2$	$\delta_\perp$ (rad)	$\delta_\parallel$ (rad)	$\delta_\perp - \delta_S$ (rad)
ID alignment	$< 10^{-2}$	$< 10^{-3}$	$< 10^{-3}$	$< 10^{-3}$	$< 10^{-3}$	-	$< 10^{-2}$	$< 10^{-2}$	-
Trigger efficiency	$< 10^{-2}$	$< 10^{-3}$	0.002	$< 10^{-3}$	$< 10^{-3}$	$< 10^{-3}$	$< 10^{-2}$	$< 10^{-2}$	$< 10^{-2}$
B_d^0 contribution	0.03	0.001	$< 10^{-3}$	$< 10^{-3}$	0.005	0.001	0.02	$< 10^{-2}$	$< 10^{-2}$
Tagging	0.10	0.001	$< 10^{-3}$	$< 10^{-3}$	$< 10^{-3}$	0.002	0.05	$< 10^{-2}$	$< 10^{-2}$
Models:									
default fit	$< 10^{-2}$	0.002	$< 10^{-3}$	0.003	0.002	0.006	0.07	0.01	0.01
signal mass	$< 10^{-2}$	0.001	$< 10^{-3}$	$< 10^{-3}$	0.001	$< 10^{-3}$	0.03	0.04	0.01
background mass	$< 10^{-2}$	0.001	0.001	$< 10^{-3}$	$< 10^{-3}$	0.002	0.06	0.02	0.02
resolution	0.02	$< 10^{-3}$	0.001	0.001	$< 10^{-3}$	0.002	0.04	0.02	0.01
background time	0.01	0.001	$< 10^{-3}$	0.001	$< 10^{-3}$	0.002	0.01	0.02	0.02
background angles	0.02	0.008	0.002	0.008	0.009	0.027	0.06	0.07	0.03
Total	0.11	0.009	0.003	0.009	0.011	0.028	0.13	0.09	0.04

collected in 2012 could reduce the systematic uncertainty of ϕ_s.

8.3 Results of the Tagged $B_s^0 \to J/\psi\phi$ Analysis

The simultaneous maximum likelihood fit of the untagged analysis contains 25 free parameters including the nine parameters of interest $\Delta\Gamma_s$, Γ_s, ϕ_s, $|A_0(0)|^2$, $|A_\parallel(0)|^2$, $\delta_\parallel$, $\delta_\perp$, $|A_s(0)|^2$ and δ_s. The result of the tagged fit is shown in table 8.6. Improvement in comparison to the untagged fit (see chapter 7) is achieved in the reduction of the statistical uncertainty of ϕ_s by $\sim 39\,\%$. For $\delta_\perp - \delta_S$ the tagged fit yields a value of 3.14 ± 0.11 which corresponds to one of the two solutions that were obtained in the untagged fit (see appendix A.2). For all other parameters the central values and uncertainties of the untagged fit have been reproduced.

The correlations between the fit parameters are shown in table 8.7. As the tagged decay rate includes additional terms that depend on ϕ_s and Γ_s the correlation between the two parameters decreased to 0.026 in comparison to the untagged fit where it was 0.38 (see table 7.2). In addition, the correlation between ϕ_s and $\Delta\Gamma_s$ has changed its sign from -0.13 in the untagged fit to 0.107 in the tagged fit which is also caused by the additional tagging terms in the likelihood function. All other numbers in the table stayed approximately the same.

Table 8.6: Fit result of the tagged fit with statistical and systematic uncertainties. $\delta_\parallel$ and $\delta_\perp - \delta_S$ are given as 1 σ confidence regions.

Parameter	Value	Statistical uncertainty	Systematic uncertainty
ϕ_s [rad]	0.12	0.25	0.11
$\Delta\Gamma_s$ [ps^{-1}]	0.053	0.021	0.009
Γ_s [ps^{-1}]	0.677	0.007	0.003
$\lvert A_0(0)\rvert^2$	0.529	0.006	0.011
$\lvert A_\parallel(0)\rvert^2$	0.220	0.008	0.009
$\lvert A_S(0)\rvert^2$	0.024	0.014	0.028
$\delta_\perp$ [rad]	3.89	0.46	0.13
$\delta_\parallel$ [rad]	[3.04-3.23]		0.09
$\delta_\perp - \delta_S$ [rad]	[3.02-3.25]		0.04

Table 8.7: Correlations between the physics parameters of the tagged fit.

	ϕ_s	$\Delta\Gamma$	Γ_s	$\lvert A_\parallel(0)\rvert^2$	$\lvert A_0(0)\rvert^2$	$\lvert A_S(0)\rvert^2$	$\delta_\parallel$	$\delta_\perp$	$\delta_\perp - \delta_S$
ϕ_s	1.000	0.107	0.026	0.010	0.002	0.029	0.021	−0.043	−0.003
$\Delta\Gamma$		1.000	−0.617	0.105	0.103	0.069	0.006	−0.017	0.001
Γ_s			1.000	−0.093	−0.063	0.034	−0.003	0.001	−0.09
$\lvert A_\parallel(0)\rvert^2$				1.000	−0.316	0.077	0.008	0.005	−0.010
$\lvert A_0(0)\rvert^2$					1.000	0.283	−0.003	−0.016	−0.025
$\lvert A_S(0)\rvert^2$						1.000	−0.011	−0.054	−0.098
$\delta_\parallel$							1.000	0.038	0.007
$\delta_\perp$								1.000	0.081
$\delta_\perp - \delta_S$									1.000

For individual parameters one-dimensional likelihood scans are produced to ensure Gaussian behavior of the likelihood function around the central values. The selected parameter is stepwise increased from the minimal to the maximum value of the allowed range and the fit is performed for each value with this parameter fixed. Figure 8.10 illustrates the scans for $\Delta\Gamma_s$ and ϕ_s which show the expected Gaussian shape around the central value. The corresponding plots for the strong phases are shown in figure 8.11. While the plots for $\delta_\parallel$ and $\delta_\perp$ confirm the obtained values and uncertainty, the scan of $\delta_\perp - \delta_S$ shows a minimum at about $\sim \pi$ but the fit is insensitive at a level of ~ 2 σ over the rest of the range. Therefore the result is given as the 1 σ confidence interval $[3.02 - 3.25]$rad.

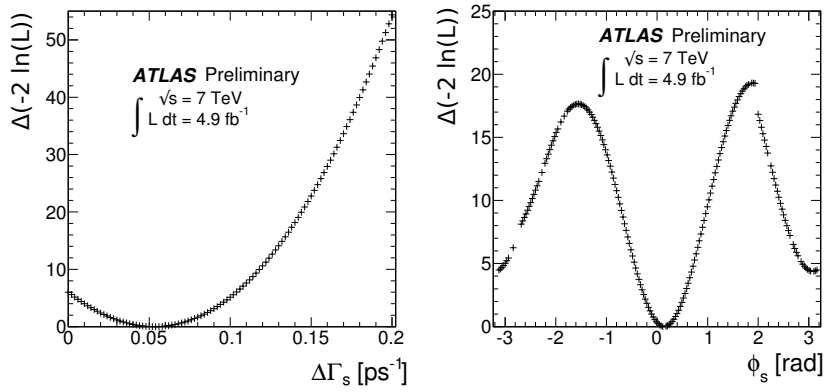

Figure 8.10: 1D likelihood scans for $\Delta\Gamma_s$ (left) and ϕ_s (right).

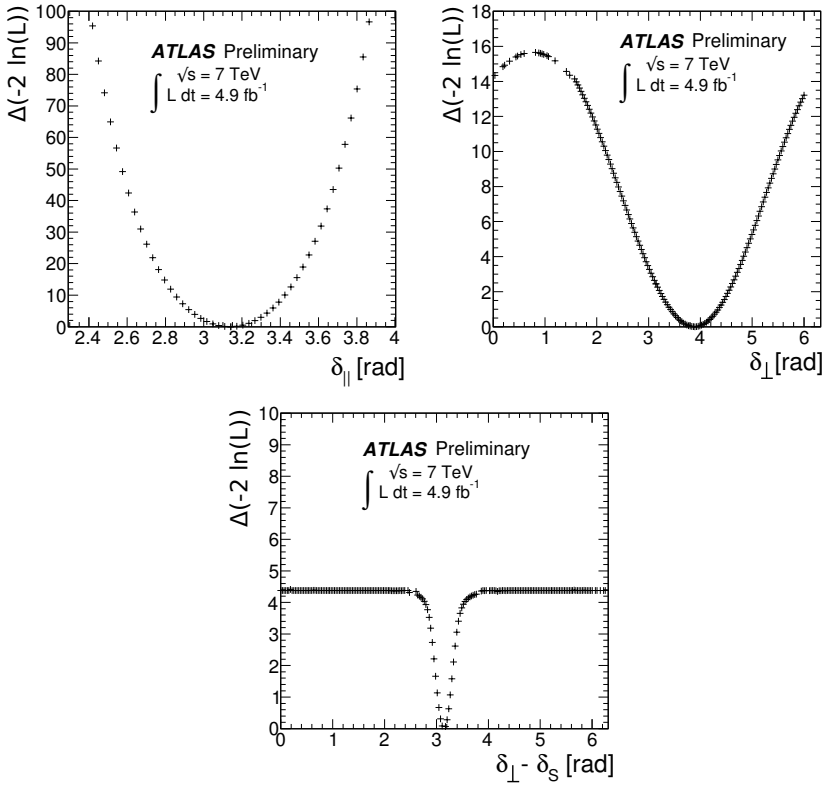

Figure 8.11: 1D likelihood scans for $\delta_{\parallel}$ (top left), $\delta_{\perp}$ (top right) and $\delta_{\perp} - \delta_S$ (bottom).

As already mentioned in chapter 7.1, the differential decay rate of the tagged fit is invariant under the parameter transformation described by equation 7.2. In this analysis $\Delta\Gamma_s$ is constrained to be positive, as the negative value was excluded in a measurement performed by LHCb [79]. The obtained value for ϕ_s is close to zero and the the fitted value for $\delta_\perp - \delta_S$ is close to π. This combination contradicts the result of [59], where the solution with positive $\Delta\Gamma_s$ and ϕ_s close to zero is accompanied by a value for $\delta_\perp - \delta_S$ at about zero and not at about π. An explanation for this discrepancy between the two measurements could be that the sensitivity to the strong phase of the S-wave contribution, as shown in the bottom plot of 8.11, is very weak.

The values measured in the tagged $B_s^0 \to J/\psi\phi$ analysis for ϕ_s, $\Delta\Gamma_s$, $\Delta\Gamma_s$ and the amplitudes $|A_0(0)|^2$ and $|A_\parallel(0)|^2$ are within their errors consistent with the measurements performed by CDF, DO, CMS and LHCb (see section 2.8). The two-dimensional likelihood contour in the $\phi_s - \Delta\Gamma_s$ plane, with the reduced uncertainty of ϕ_s compared to the untagged analysis, presented in figure 8.12 shows the agreement of the result with the values predicted by the Standard Model.

An overview of the results of the $B_s^0 \to J/\psi\phi$ analyses from different experiments is shown in figure 8.13 (*O. Schneider, personal communication, June 6, 2013*). This figure shows the results measured by CDF [56], D0 [57] and LHCb [59] as likelihood contours in the $\phi_s - \Delta\Gamma_s$ plane. The ATLAS results [25] is represented as an ellipse centered at the fitted value with the uncertainties as semi-axis and tilted by the angle that corresponds to the correlation of 0.107 between ϕ_s and $\Delta\Gamma_s$ obtained from the fit. Figure 8.13 also shows the combined average of the four results which is in very good agreement with the Standard Model prediction [22, 55]. However, the possibility of a New Physics induced contribution to ϕ_s is not yet excluded. With the prospect of analyzing the data collected at the LHC in 2012, the still statistical dominated uncertainties of ϕ_s measured by ATLAS and LHCb will further decrease during the next years.

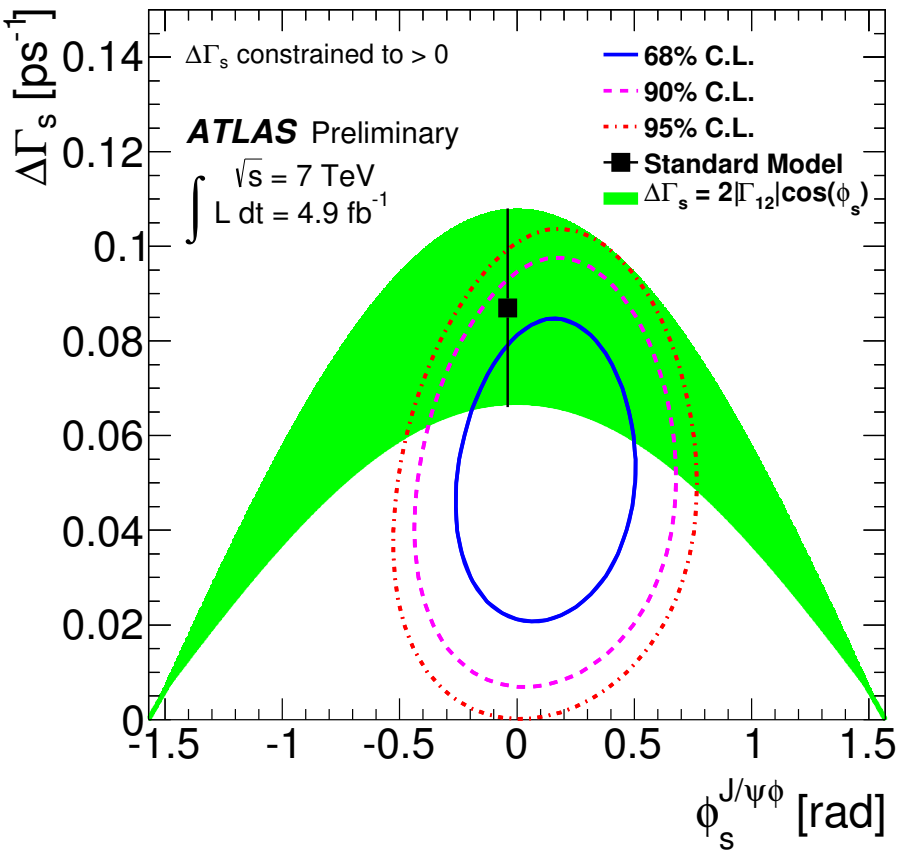

Figure 8.12: Likelihood contour in the $\phi_s - \Delta\Gamma_s$ plane. The likelihood contours are shown for 68 % in blue, 90 % in magenta and 95 % in red. Only statistical errors are taken into account. The Standard Model value is depicted by the black point [22,55] and the green band represents the theoretical prediction for mixing induced CP violation (equation 2.32).

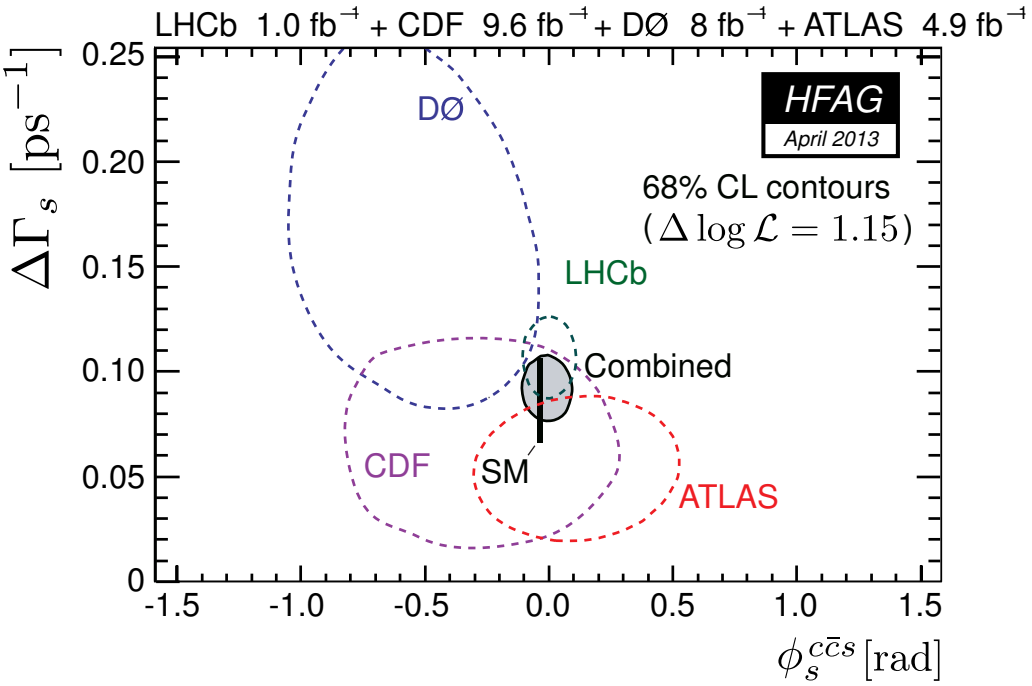

Figure 8.13: Overview of the $\phi_s - \Delta\Gamma_s$ plane with the results of the $B_s^0 \to J/\psi\phi$ analyses performed by CDF (purple), D0 (blue), ATLAS (red) and LHCb (green). The measurements of CDF, D0 and LHCb are represented as 68 % confidence level likelihood contours. The ATLAS result is shown as an ellipse tilted according to the correlation between ϕ_s and $\Delta\Gamma_s$ that was obtained in the fit. The ellipse represents the 68 % confidence level contour. The black bar denotes the Standard Model predictions for the two parameters including their theoretical uncertainties [22, 55]. The grey colored area with the black border depicts the combined average result of the four experiments which takes into account the correlations between ϕ_s and $\Delta\Gamma_s$, but not the one between $\Delta\Gamma_s$ and Γ_s.

Chapter 9

Conclusion

In this thesis the angular analysis of the $B_s^0 \to J/\psi\phi$ decay using the ATLAS detector at the LHC has been presented. The CP violating phase ϕ_s as well as the decay width Γ_s and the decay width difference $\Delta\Gamma_s$ characterizing the neutral B_s^0 system are measured using an unbinned maximum likelihood fit. The fit is applied to B_s^0 candidates reconstructed in the dataset collected by the ATLAS detector in 2011. The data corresponds to an integrated luminosity of $4.9\,\text{fb}^{-1}$ recorded in $p-p$ collisions at a center-of mass energy of $\sqrt{s} = 7\,\text{TeV}$ produced by the LHC.
The first step of the analysis is the reconstruction and selection of B_s^0 candidates using the information gathered by the inner tracking detectors and muon spectrometer. After that a simultaneous fit to the mass, lifetime and angular distributions of the selected data is performed, where the final state is described in terms of the transversity basis. The purpose of the mass fit is to discriminate between signal and background events, the angular fit is used to disentangle CP even and CP odd components of the final state. A possible S-wave contribution to the data sample from $B_s^0 \to J/\psi f_0$ decays and non resonant $B_s^0 \to J/\psi K^+K^-$ decays are accounted for in the fit and its size is measured. In addition to a general background component, contamination of the data sample from B_d^0 reflections is incorporated with dedicated terms in the likelihood function.
Initially an untagged analysis was performed without using knowledge about the production flavor of the decaying B_s^0 candidate. With the application of two opposite side flavor tagging methods the sensitivity of the measurement to the CP violating phase ϕ_s improved. A total of $22\,670 \pm 150$ signal B_s^0 mesons are observed in the full fit. In addition to ϕ_s, Γ_s and $\Delta\Gamma_s$ the transversity amplitudes $|A_0(0)|^2$ and $|A_\parallel(0)|^2$, the strong phase $\delta_\perp$ and the size of the S-wave contribution $|A_S(0)|^2$ are measured. The obtained values

are:

$$\begin{aligned}
\phi_s &= 0.12 \pm 0.25(\text{stat.}) \pm 0.11(\text{syst.})\,\text{rad},\\
\Delta\Gamma_s &= 0.058 \pm 0.021(\text{stat.}) \pm 0.009(\text{syst.})\,\text{ps}^{-1},\\
\Gamma_s &= 0.677 \pm 0.007(\text{stat.}) \pm 0.003(\text{syst.})\,\text{ps}^{-1},\\
|A_0(0)|^2 &= 0.529 \pm 0.006(\text{stat.}) \pm 0.011(\text{syst.}),\\
|A_\parallel(0)|^2 &= 0.220 \pm 0.008(\text{stat.}) \pm 0.009(\text{syst.}),\\
|A_S(0)|^2 &= 0.024 \pm 0.014(\text{stat.}) \pm 0.028(\text{syst.}),\\
\delta_\perp &= 3.89 \pm 0.46(\text{stat.}) \pm 0.13(\text{syst.})\,\text{rad}.
\end{aligned}$$

Systematic uncertainties from residual inner detector alignment, modeling of signal and background components in the fit, size of the B_d^0 reflections in the data sample, trigger and detector efficiency and flavor tagging were evaluated. For all parameters the largest uncertainty comes from the modeling of the background angles in the fit, except for ϕ_s where the systematic uncertainty due to flavor tagging dominates. The results are in agreement with previous measurements of this decay channel at other experiments. An overview of measurements constraining the values of Γ_s and $\Delta\Gamma_s$ is shown in figure 7.18. The measured values for ϕ_s and $\Delta\Gamma_s$ are within their uncertainties in agreement with the Standard Model prediction which is illustrated in figure 8.12. The determined magnitude of the S-wave contribution in the data sample is very small and within the errors consistent with zero.
The presented result of the measurement is still statistically dominated for the physical interesting parameters ϕ_s, Γ_s and $\Delta\Gamma_s$. Thus an update of the measurement using the $\sim 4-5$ times larger dataset collected with the ATLAS detector in 2012, will presumably increase the precision of the result. From the technical side improvement could be achieved through the development and usage of further flavor tagging methods and enhancement of the angular model of the background.

Appendix A

Appendices of the Untagged Analysis

A.1 Differential Decay Rate for the Untagged Fit

In the case of an untagged $B_s^0 \to J/\psi\phi$ analysis the differential decay rate can be simplified. Each B_s^0 candidate is assumed to have equal probability to be a particle or antiparticle and consequently all terms containing Δm_s cancel out. The differential decay rate used in the untagged analysis presented in chapter 7 and published in [24] is:

$$\frac{d\Gamma}{dt\,d\Omega} = \sum_{k=1}^{10} h^k(t) g^k(\theta, \psi, \phi) \tag{A.1}$$

where $h^k(t)$ and $g^k(\theta, \psi, \phi)$ are defined in table A.1.

Table A.1: Table showing the ten time-dependent amplitudes, $h^{(k)}(t)$ and the functions of the transversity angles $g^{(k)}(\theta, \psi, \phi)$ of the untagged analysis. The amplitudes $|A_0(0)|^2$ and $|A\|(0)|^2$ describe the CP even components of the $B_s^0 \to J/\psi\phi$ decay, $|A(0)_\perp|^2$ is the CP odd amplitude. The amplitudes have corresponding strong phases δ_0, $\delta_\|$ and $\delta_\perp$, by convention δ_0 is set to zero. The S-wave amplitude $|A_S(0)|^2$ gives the fraction of $B_s^0 \to J/\psi f_0$ and non-resonant $B_s^0 \to J/\psi K^+K^-$ decays and has a related strong phase δ_S.

k	$h^{(k)}(t)$	$g^{(k)}(\theta, \psi, \phi)$
1	$\frac{1}{2}\lvert A_0(0)\rvert^2 \left[(1+\cos\phi_s)\, e^{-\Gamma_L t} + (1-\cos\phi_s)\, e^{-\Gamma_H t}\right]$	$2\cos^2\psi(1-\sin^2\theta\cos^2\phi)$
2	$\frac{1}{2}\lvert A_\|(0)\rvert^2 \left[(1+\cos\phi_s)\, e^{-\Gamma_L t} + (1-\cos\phi_s)\, e^{-\Gamma_H t}\right]$	$\sin^2\psi(1-\sin^2\theta\sin^2\phi)$
3	$\frac{1}{2}\lvert A_\perp(0)\rvert^2 \left[(1-\cos\phi_s)\, e^{-\Gamma_L t} + (1+\cos\phi_s)\, e^{-\Gamma_H t}\right]$	$\sin^2\psi\sin^2\theta$
4	$\frac{1}{2}\lvert A_0(0)\rvert\lvert A_\|(0)\rvert\cos\delta_\|$ $\left[(1+\cos\phi_s)\, e^{-\Gamma_L t} + (1-\cos\phi_s)\, e^{-\Gamma_H t}\right]$	$-\frac{1}{\sqrt{2}}\sin 2\psi\sin^2\theta\sin 2\phi$
5	$\lvert A_\|(0)\rvert\lvert A_\perp(0)\rvert[\frac{1}{2}(e^{-\Gamma_L t} - e^{-\Gamma_H t})\cos(\delta_\perp - \delta_\|)\sin\phi_s]$	$\sin^2\psi\sin 2\theta\sin\phi$
6	$\lvert A_0(0)\rvert\lvert A_\perp(0)\rvert[\frac{1}{2}(e^{-\Gamma_L t} - e^{-\Gamma_H t})\cos\delta_\perp\sin\phi_s]$	$\frac{1}{\sqrt{2}}\sin 2\psi\sin 2\theta\cos\phi$
7	$\frac{1}{2}\lvert A_S(0)\rvert^2 \left[(1-\cos\phi_s)\, e^{-\Gamma_L t} + (1+\cos\phi_s)\, e^{-\Gamma_H t}\right]$	$\frac{2}{3}\left(1-\sin\theta\cos^2\phi\right)$
8	$\lvert A_S\rvert\lvert A_\|(0)\rvert[\frac{1}{2}(e^{-\Gamma_L t} - e^{-\Gamma_H t})\sin(\delta_\| - \delta_S)\sin\phi_s]$	$\frac{1}{3}\sqrt{6}\sin\psi\sin^2\theta\sin 2\phi$
9	$\frac{1}{2}\lvert A_S\rvert\lvert A_\perp(0)\rvert\sin(\delta_\perp - \delta_S)$ $\left[(1-\cos\phi_s)\, e^{-\Gamma_L t} + (1+\cos\phi_s)\, e^{-\Gamma_H t}\right]$	$\frac{1}{3}\sqrt{6}\sin\psi\sin 2\theta\cos\phi$
10	$\lvert A_0(0)\rvert\lvert A_S(0)\rvert[\frac{1}{2}(e^{-\Gamma_H t} - e^{-\Gamma_L t})\sin\delta_S\sin\phi_s]$	$\frac{4}{3}\sqrt{3}\cos\psi\left(1-\sin^2\theta\cos^2\phi\right)$

A.2 Full Fit Result of the Untagged Fit

In this section the full results of the maximum likelihood fit are tabulated. When starting the fit with a value close to π for $\delta_\perp - \delta_S$, the π minus the value shown in the table.

Table A.2: All parameters and their fitted values in the untagged fit.

Parameter	Definition	Fitted Value
$\|A_0(0)\|^2$	transversity amplitude for longitudinal polarization	0.5282 ± 0.0061
$\|A_\parallel(0)\|^2$	transversity amplitude for transverse and parallel polarization	0.2198 ± 0.0076
$\Delta\Gamma_s$	decay width difference [ps^{-1}]	0.053 ± 0.021
Γ_s	average decay width [ps^{-1}]	0.6772 ± 0.0072
ϕ_s	CP violating phase [rad]	0.22 ± 0.41
$\delta_\parallel$	strong phase of $A_\parallel$ [rad]	3.14 ± 0.10
$\delta_\perp$	strong phase of $A_\perp$ [rad]	2.88 ± 0.36
$\|A_S(0)\|^2$	S-wave amplitude	0.020 ± 0.017
$\delta_\perp - \delta_S$	strong phase of A_S relative to $\delta_\perp$ [rad]	0.029 ± 0.13
s_t	time uncertainty scale factor	1.0200 ± 0.0052
M	mean mass of B_s^0 [GeV]	5.36700 ± 0.00016
s_m	mass uncertainty scale factor	1.1900 ± 0.0087
f_s	signal fraction	0.1738 ± 0.0012
τ_-	negative bkg lifetime [ps]	0.1582 ± 0.0062
τ_+	short-lived positive bkg lifetime [ps]	0.3358 ± 0.0063
τ_{++}	long lived positive bkg lifetime [ps]	1.593 ± 0.041
f_g	Gaussian fraction of bkg time	0.6329 ± 0.0050
f_-	fraction of bkg that decays with τ_-	0.100 ± 0.007
f_+	fraction of bkg that decays with τ_+	0.801 ± 0.022
a	background mass slope	-0.2198 ± 0.0061
a_1	first parameter for bkg θ	-1.38 ± 0.23
a_2	second parameter for bkg θ	-0.82 ± 0.15
b_1	parameter for bkg ψ	-0.230 ± 0.062
c_0	first parameter for bkg ϕ	-3.128 ± 0.011
c_1	second parameter for bkg ϕ	0.3902 ± 0.0043

Appendix B

Appendices of the Tagged Analysis

B.1 Mass Lifetime Fit of B_d^0 Events Using the Information of the Jet Charge Tagger

Figure B.1 shows the mass and proper decay time projection of the mass lifetime fit to $B_d^0 \to J/\psi K^*$ events making use of the jet charge tagger.

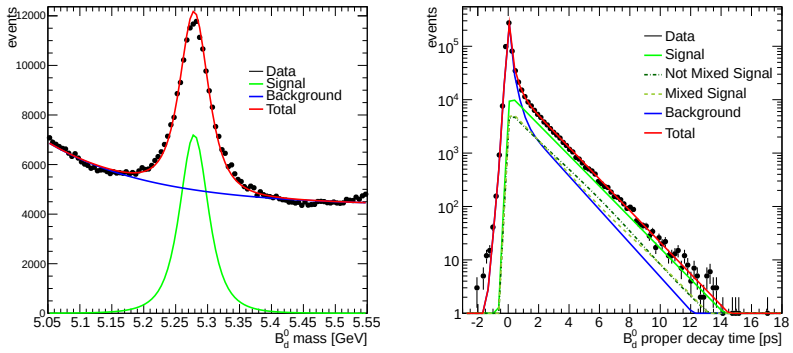

Figure B.1: Mass (left) and proper decay time (right) projection of the mass lifetime fit to B_d^0 events using the information from the jet charge flavor tagger only. Black points denote the data, the signal is shown in green, the background in blue and the total fit is shown in red. The dashed green line denotes the mixed portion and the dotted-dashed green line denotes the not mixed portion of the signal component.

B.2 Exemplary Pseudo-experiment for the Tagged Analysis

To determine possible biases and estimate systematic uncertainties due to parameterization of the different components in the fit model of the tagged fit, pseudo-experiments are generated. They are generated using the result of the fit to data and the fit function. The procedure is the same as for the untagged analysis, except that the tag probability is generated in addition. The tag probabilities for each tagger are generated using histograms from sideband data for the background. To generate the tag probabilities for signal events, the sideband subtraction method is used to create the corresponding histograms. The distributions of the tagging variables for an exemplary pseudo-experiment are shown in figure B.2 and the kinematic variables are shown in 7.4.

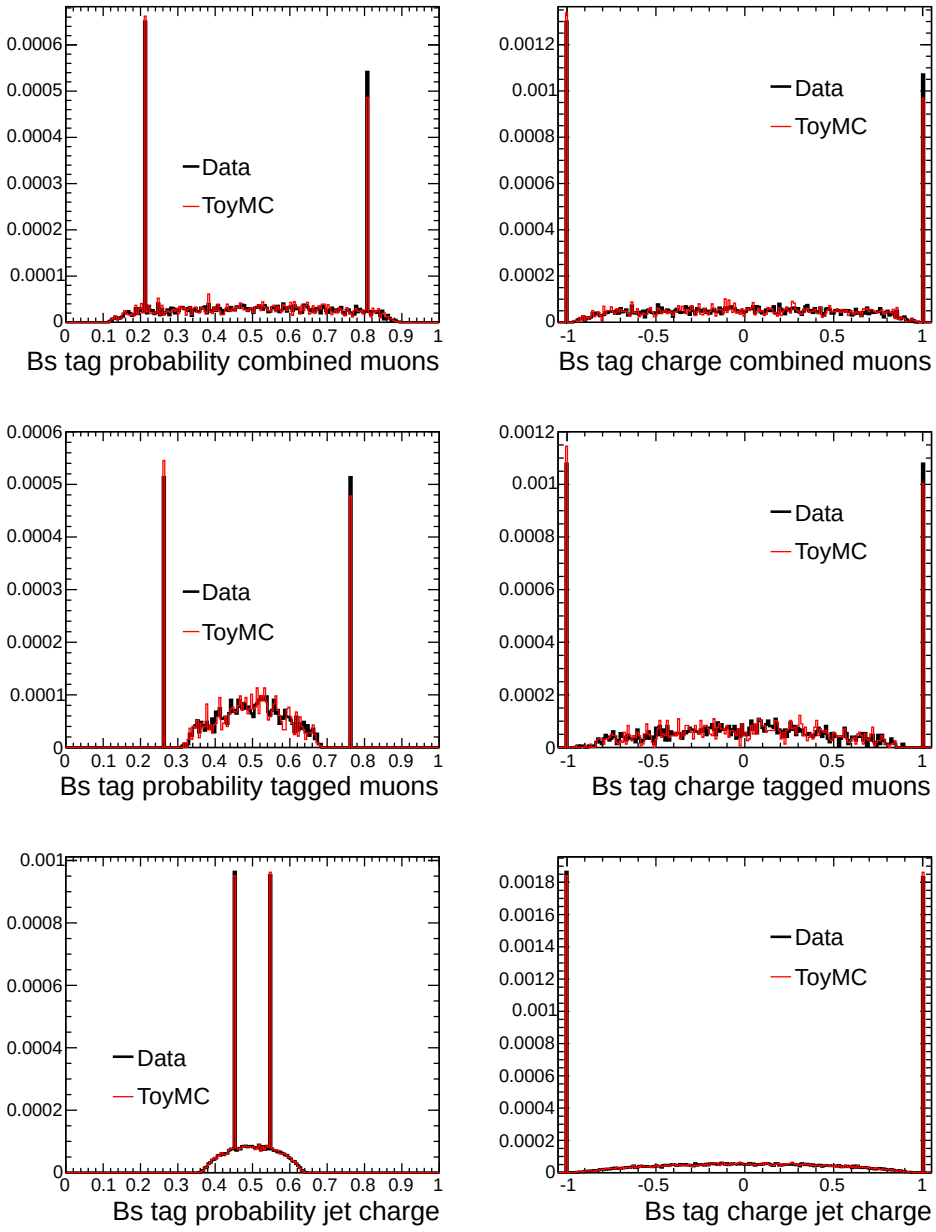

Figure B.2: Comparison of tag charge and tag probability for the different flavor tagging methods of an exemplary pseudo-experiment (red) with the reconstructed B_s^0 candidates in data (black).

B.3 Fit to Pseudo-experiments for the Estimation of Fit Model Systematics in the Tagged Analysis

To estimate the systematic uncertainties due to parameterization of the different components in the fit model of the tagged, pseudo-experiments are generated with alternative parameterizations and fitted with the default fit. The same altered models as for the untagged fit are used which are described in section 7.3.1. The fit results to 1000 pseudo-experiments for each model are presented in figures B.3 to B.13. Each distribution is fitted with a Gaussian to determine the mean value.

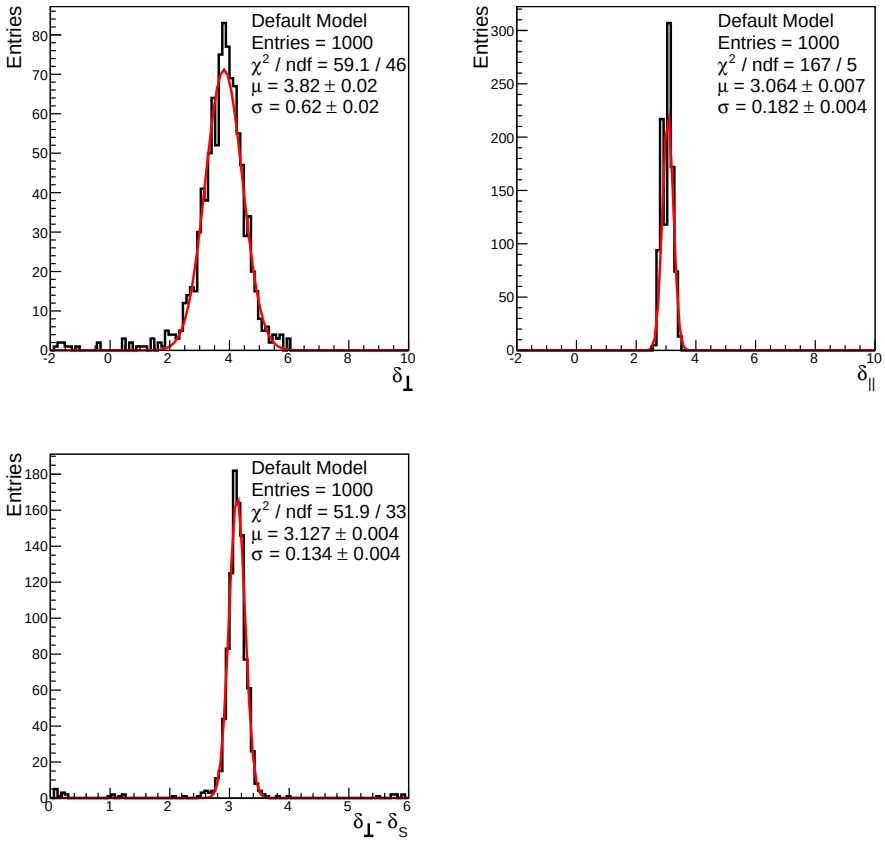

Figure B.3: Distributions of fitted values of the strong phases from tagged fits to 1000 pseudo-experiments generated with the default fit model. The red curve is a Gaussian fit to the distribution.

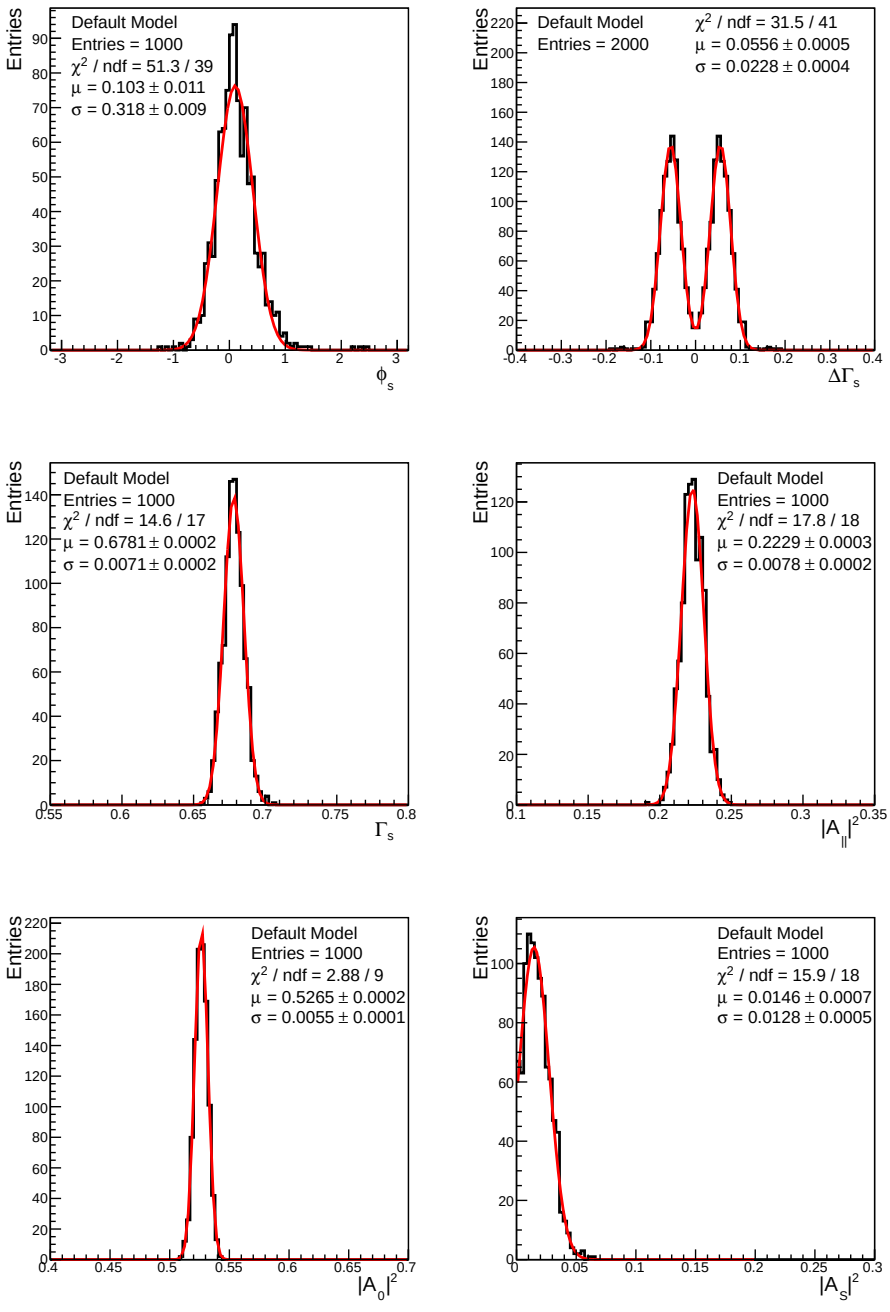

Figure B.4: Distributions of fit values from tagged fits to 1000 pseudo-experiments generated with the default fit model. The red curve is a Gaussian fit to the distribution.

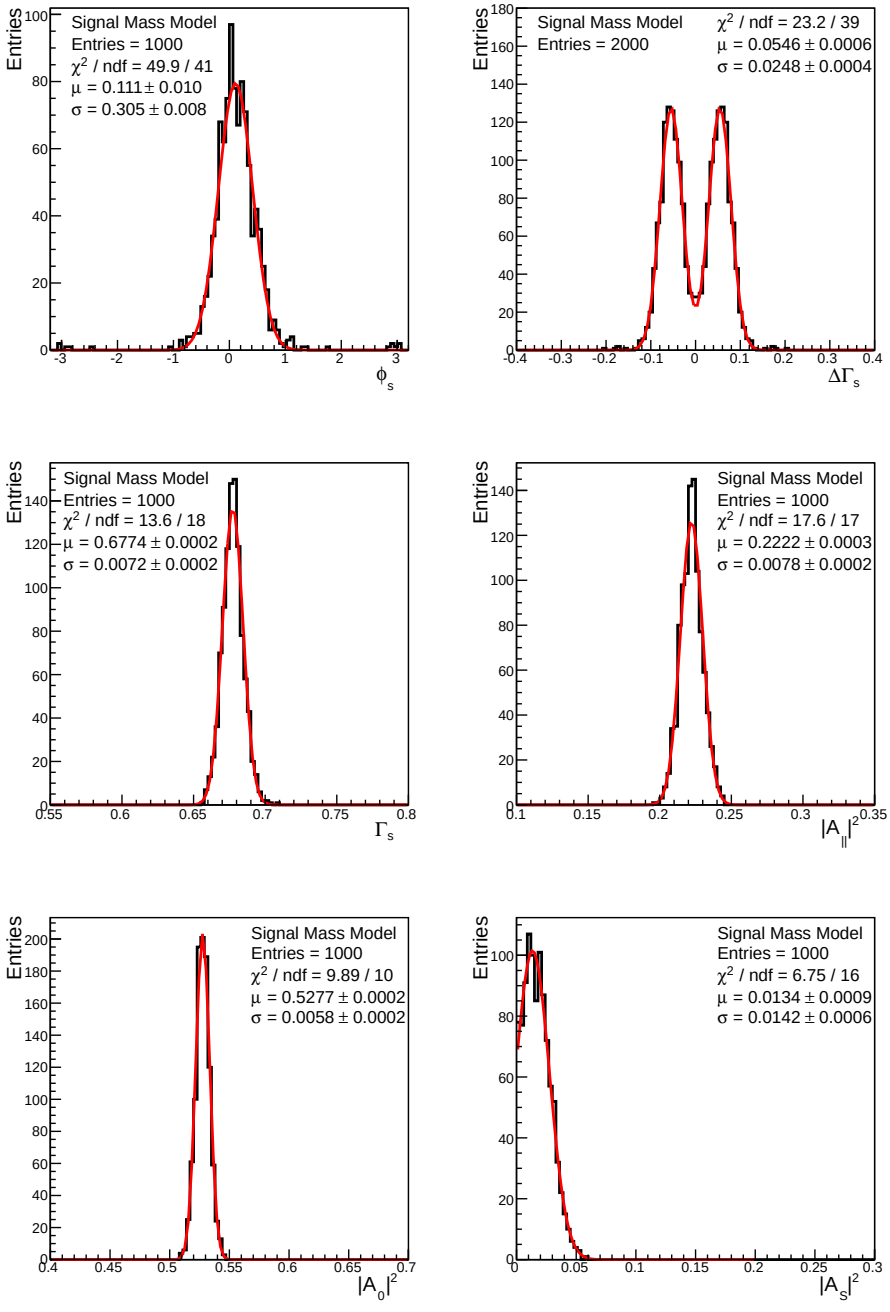

Figure B.5: Distributions of fit values from fits to 1000 pseudo-experiments generated with an alternative signal mass model. The red curve is a Gaussian fit to the distribution.

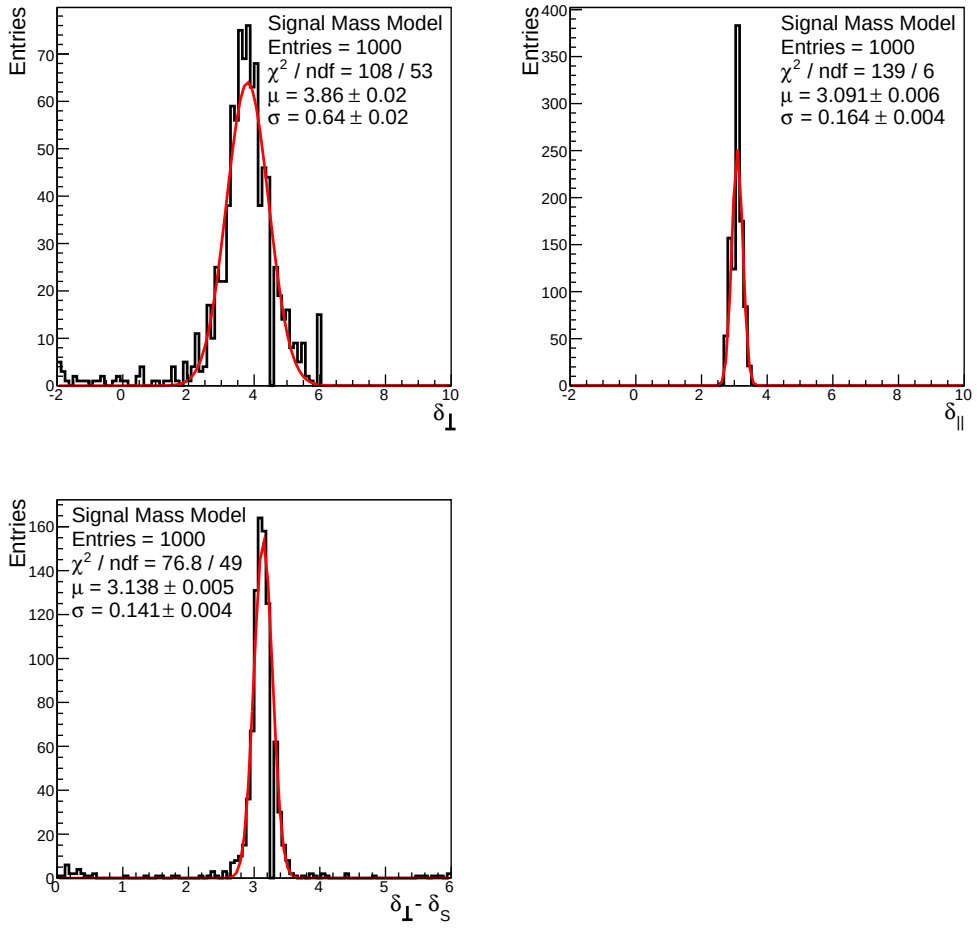

Figure B.6: Distributions of fitted values of the strong phases from fits to 1000 pseudo-experiments generated with an alternative signal mass model. The red curve is a Gaussian fit to the distribution.

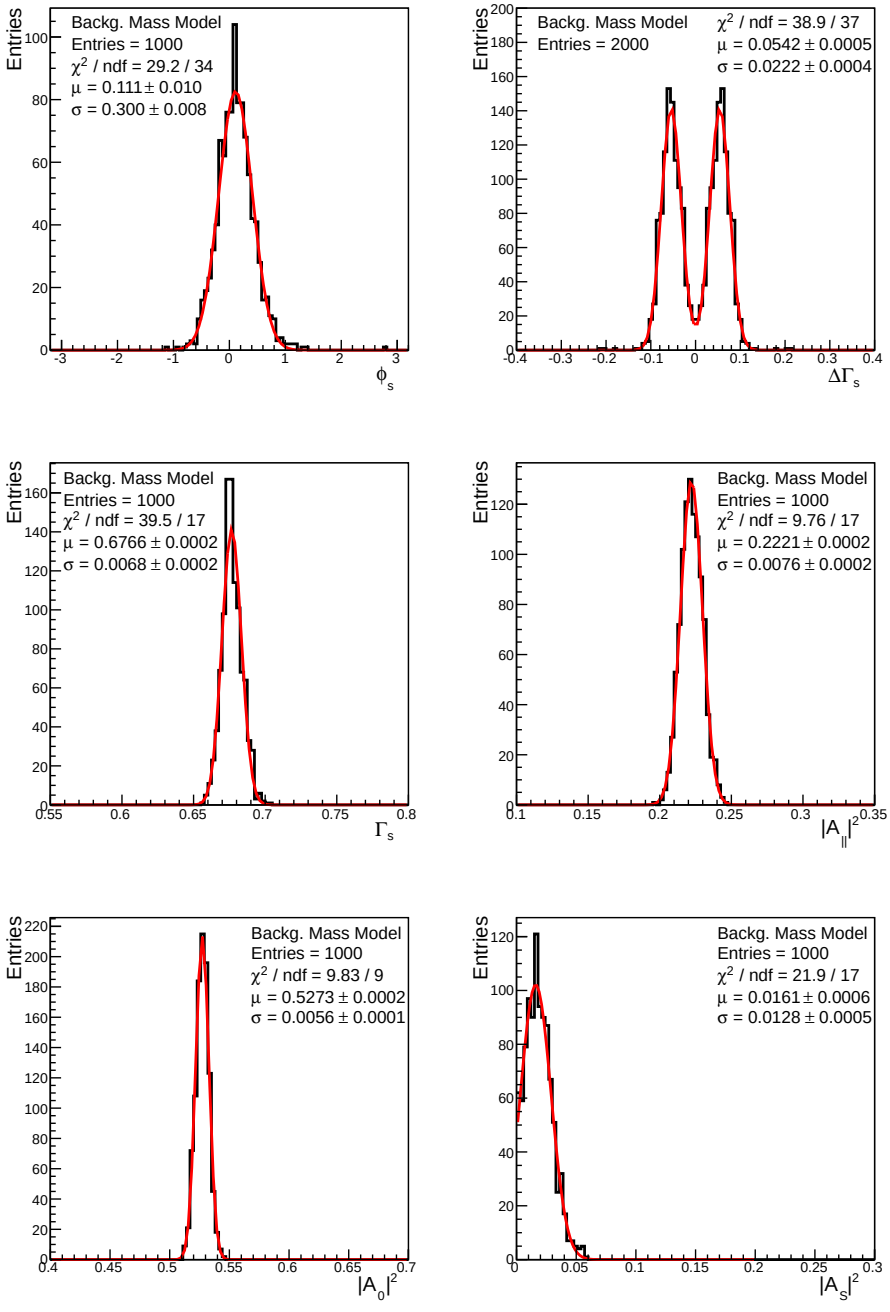

Figure B.7: Distributions of fit values from fits to 1000 pseudo-experiments generated with an alternative background mass model. The red curve is a Gaussian fit to the distribution.

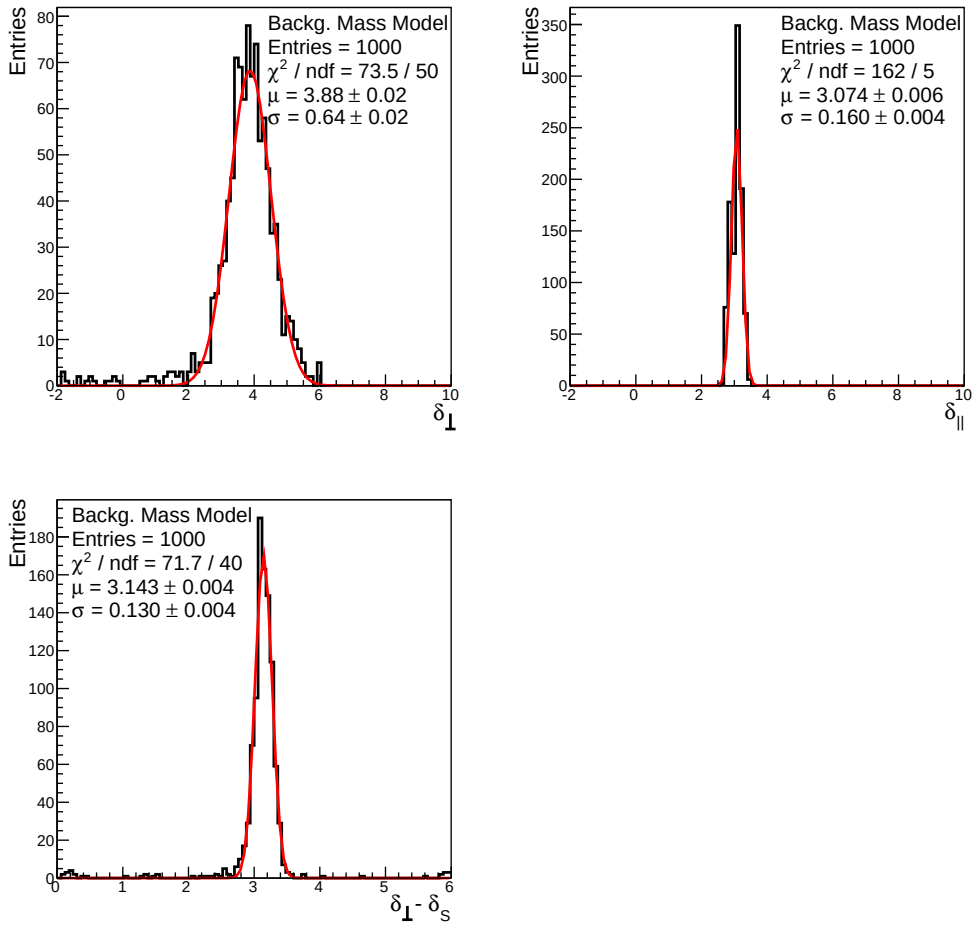

Figure B.8: Distributions of fitted values of the strong phases from fits to 1000 pseudo-experiments generated with an alternative background mass model. The red curve is a Gaussian fit to the distribution.

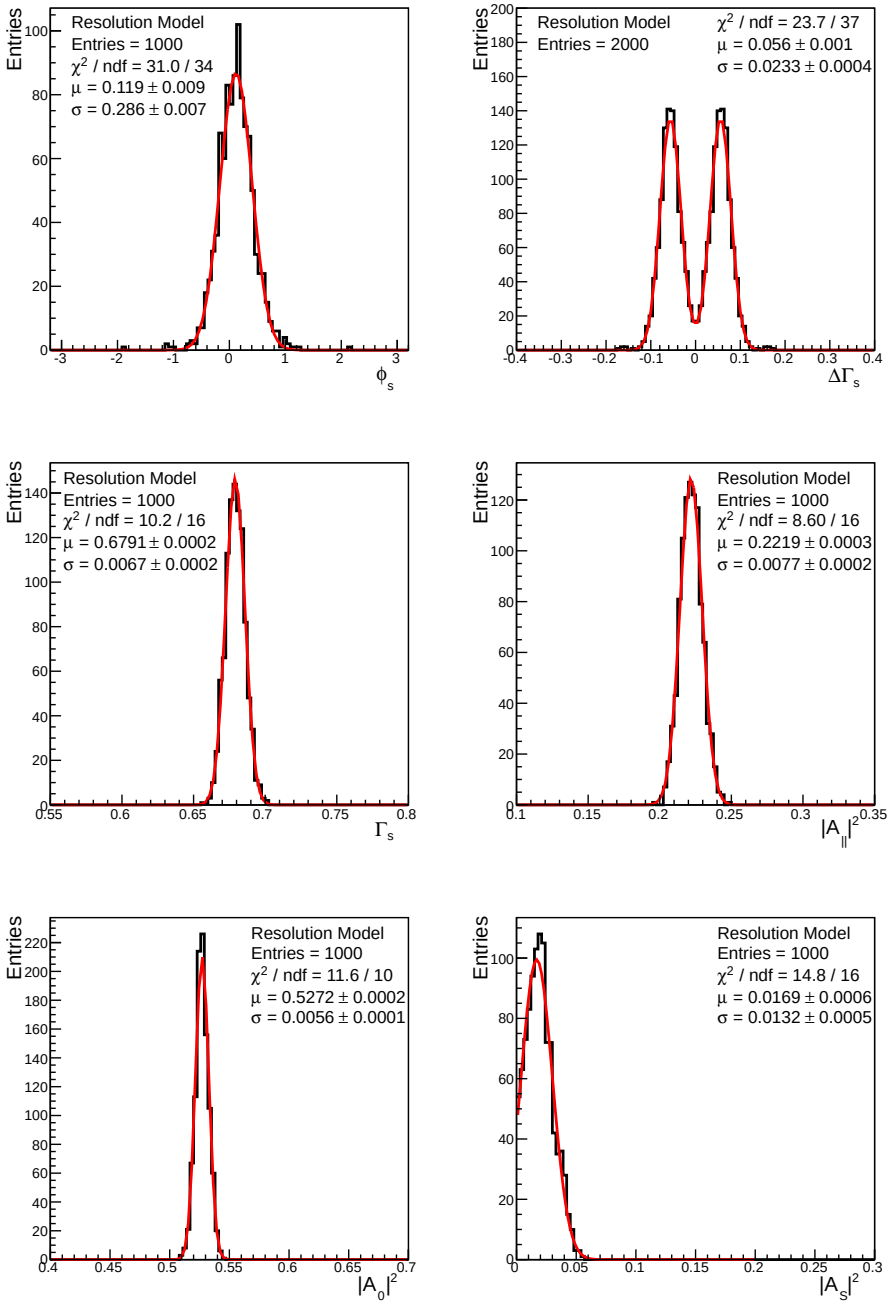

Figure B.9: Distributions of fit values from fits to 1000 pseudo-experiments generated with an alternative signal decay time model. The red curve is a Gaussian fit to the distribution.

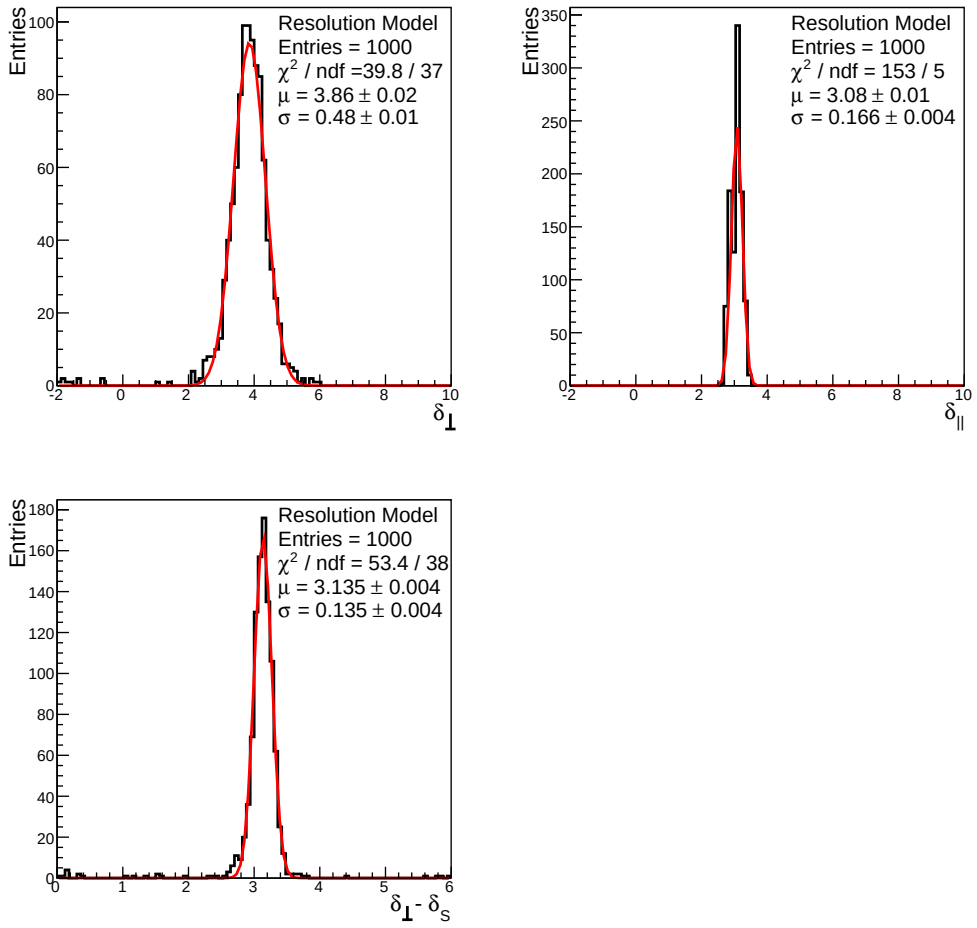

Figure B.10: Distributions of fitted values of the strong phases from fits to 1000 pseudo-experiments generated with an alternative signal decay time model. The red curve is a Gaussian fit to the distribution.

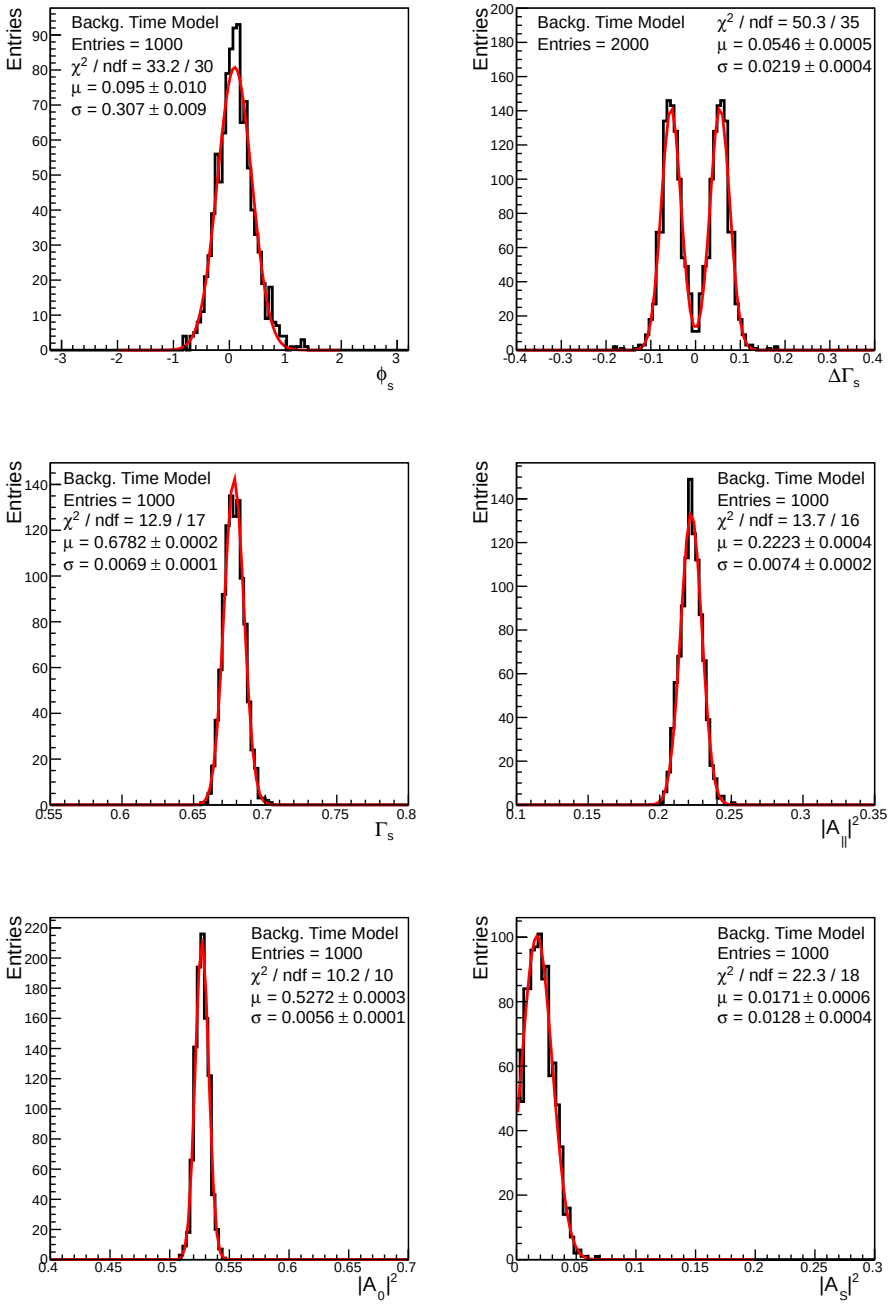

Figure B.11: Distributions of fit values from fits to 1000 pseudo-experiments generated with an alternative background time model. The red curve is a Gaussian fit to the distribution.

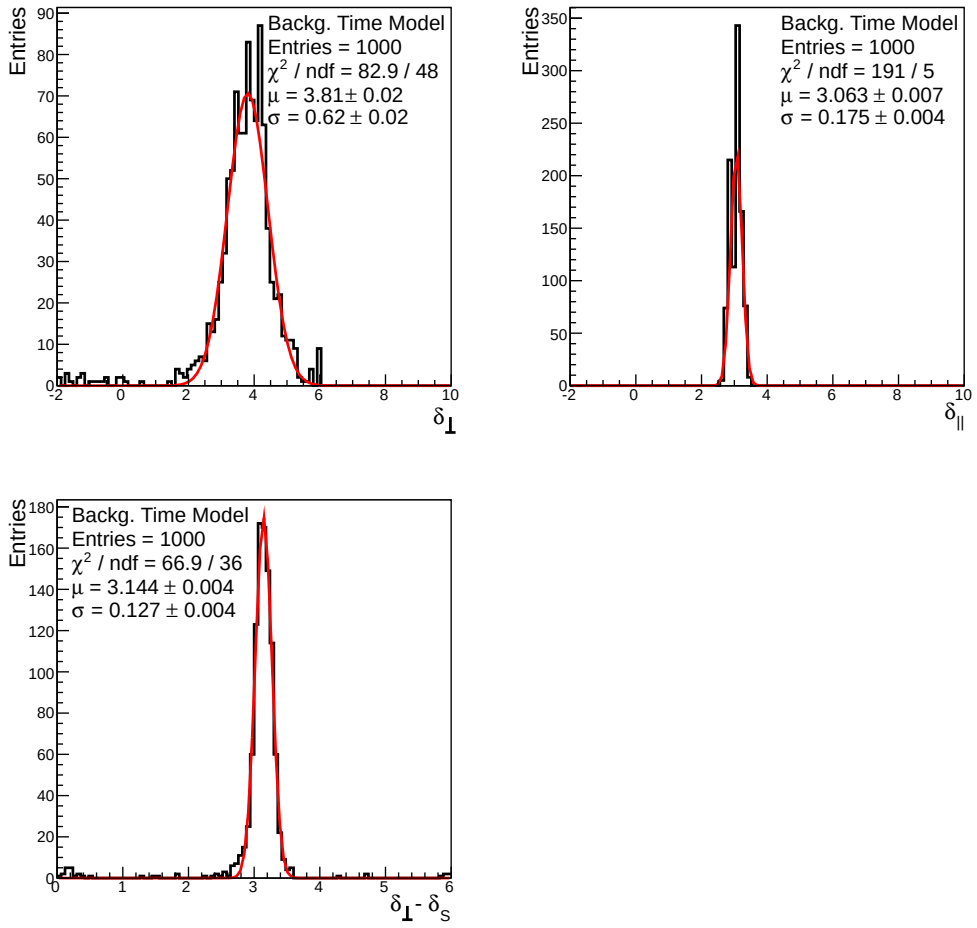

Figure B.12: Distributions of fitted values of the strong phases from fits to 1000 pseudo-experiments generated with an alternative background time model. The red curve is a Gaussian fit to the distribution.

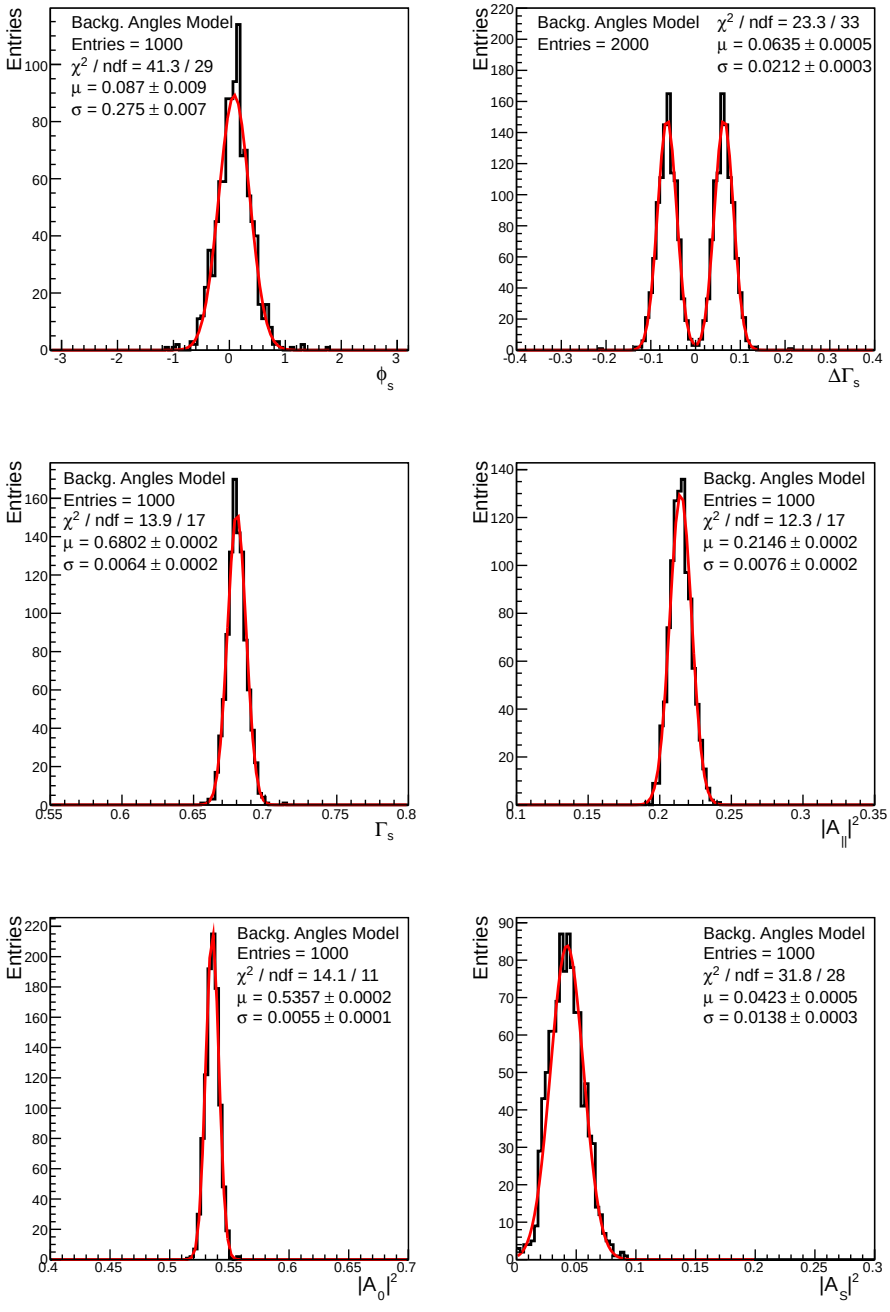

Figure B.13: Distributions of fit values from fits to 1000 pseudo-experiments generated with an alternative model for the transversity angles. The red curve is a Gaussian fit to the distribution.

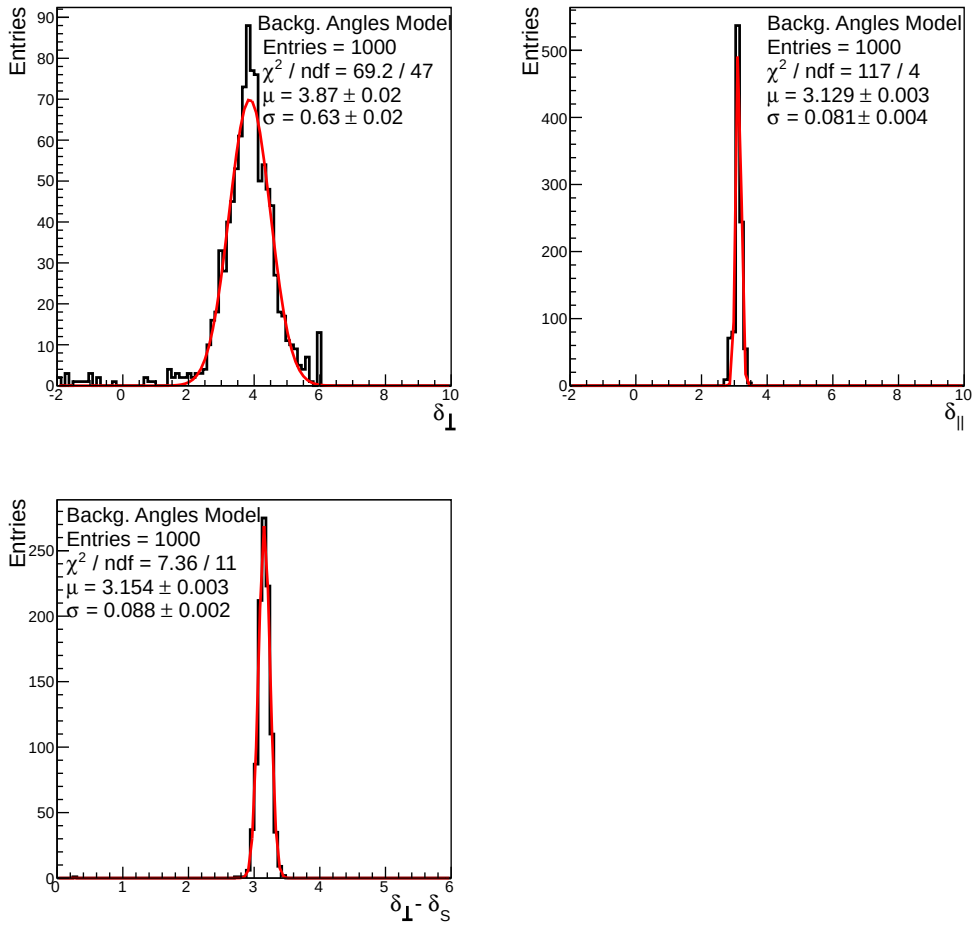

Figure B.14: Distributions of fitted values of the strong phases from fits to 1000 pseudo-experiments generated with an alternative model for the transversity angles. The red curve is a Gaussian fit to the distribution.

B.4 Full Fit Result of the Tagged Fit

In this section the full results of the tagged maximum likelihood fit are tabulated.

Table B.1: All parameters and their fitted values in the tagged fit.

Parameter	Definition	Fitted Value
$\|A_0(0)\|^2$	transversity amplitude for longitudinal polarization	0.5286 ± 0.0059
$\|A_\parallel(0)\|^2$	transversity amplitude for transverse and parallel polarization	0.2202 ± 0.0075
$\Delta\Gamma_s$	decay width difference [ps^{-1}]	0.053 ± 0.021
Γ_s	average decay width [ps^{-1}]	0.6774 ± 0.0068
ϕ_s	CP violating phase [rad]	0.12 ± 0.25
$\delta_\parallel$	strong phase of $A_\parallel$ [rad]	3.136 ± 0.095
$\delta_\perp$	strong phase of $A_\perp$ [rad]	3.89 ± 0.46
$\|A_S(0)\|^2$	S-wave amplitude	0.024 ± 0.014
$\delta_\perp - \delta_S$	strong phase of A_S relative to $\delta_\perp$ [rad]	3.14 ± 0.11
s_t	time uncertainty scale factor	1.0206 ± 0.0052
M	mean mass of B_s^0 [GeV]	5.36681 ± 0.00016
s_m	mass uncertainty scale factor	1.1933 ± 0.0088
f_s	signal fraction	0.1736 ± 0.0012
τ_-	negative bkg lifetime [ps]	0.1588 ± 0.0062
τ_+	short-lived positive bkg lifetime [ps]	0.3350 ± 0.0063
τ_{++}	long lived positive bkg lifetime [ps]	1.590 ± 0.041
f_g	Gaussian fraction of bkg time	0.6334 ± 0.0049
f_-	fraction of bkg that decays with τ_-	0.0986 ± 0.0065
f_+	fraction of bkg that decays with τ_+	0.2002 ± 0.0079
a	background mass slope	-0.2207 ± 0.0052
a_1	first parameter for bkg θ	-1.381 ± 0.055
a_2	second parameter for bkg θ	-0.828 ± 0.059
b_1	parameter for bkg ψ	-0.229 ± 0.013
c_0	first parameter for bkg ϕ	-3.131 ± 0.011
c_1	second parameter for bkg ϕ	0.3902 ± 0.0043

Appendix C

General Appendix

C.1 Background Mass Plot

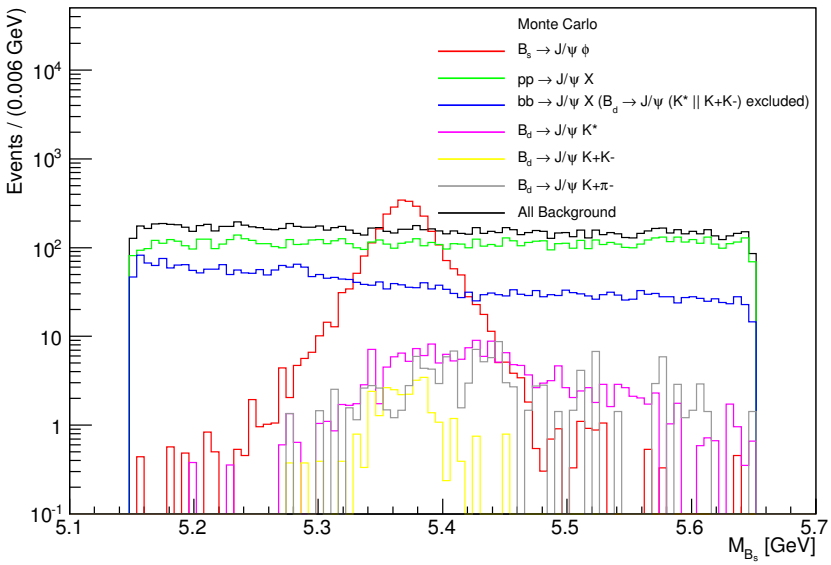

Figure C.1: Mass distribution of the B_s^0 candidates reconstructed in MC samples of signal and the different backgrounds. The plot has a logarithmic scale on the y-axis to make the shape of the dedicated B_d^0 background visible. The different background sources are explained in chapter 5.4.

C.2 B_s Lifetime Measurements in the $\Delta\Gamma_s - \tau_s$ Plane

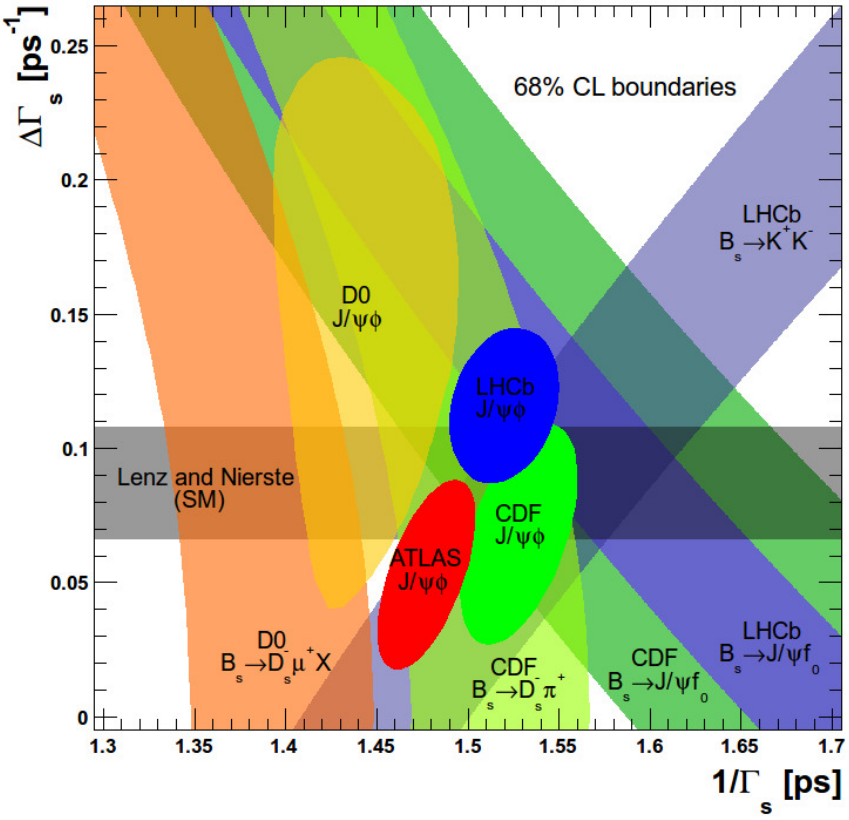

Figure C.2: Experimental measurements and SM prediction for $\Delta\Gamma_s$ vs. $\tau_s = \frac{1}{\Gamma_s}$, with 68% CL boundaries [83]. The ellipses are from $B_s \to J/\psi\phi$ studies: ATLAS [24] (red), LHCb [84] (blue), CDF [56] (green) and D0 [57] (yellow). The bands are from: $B_s \to J/\psi f_0$ studies by LHCb [85] and CDF [86] (assuming $\phi_s = 0$); $B_s \to K^+K^-$ study by LHCB [87] (assuming $A_{\Delta\Gamma_s} = -0.972$ [88]); $B_s \to D_s\pi$ study by CDF [89]; $B_s \to D_s\mu X$ study by D0 [90]. The grey band represents the Standard Model value predicted by Lenz and Nierste [55].

Bibliography

[1] S. L. Glashow, *Partial-Symmetries of Weak Interactions*, Nuclear Physics **22** (1961) 579 – 588.

[2] S. Weinberg, *A Model of Leptons*, Phys. Rev. Lett. **19** (1967) 1264–1266.

[3] A. Salam, *Weak and Electromagnetic Interactions*, *8th Nobel Symposium, 19-25 May 1968, Lerum, Sweden*, vol. C680519 (1968) 367–377.

[4] P. W. Higgs, *Broken Symmetries and the Masses of Gauge Bosons*, Phys. Rev. Lett. **13** (1964) 508+.

[5] P. W. Higgs, *Spontaneous Symmetry Breakdown without Massless Bosons*, Phys. Rev. **145** (1966) 1156–1163.

[6] F. Englert and R. Brout, *Broken Symmetry and the Mass of Gauge Vector Mesons*, Phys. Rev. Lett. **13** (1964) 321–323.

[7] G. S. Guralnik, C. R. Hagen and T. W. B. Kibble, *Global Conservation Laws and Massless Particles*, Phys. Rev. Lett. **13** (1964) 585–587.

[8] T. W. B. Kibble, *Symmetry Breaking in Non-Abelian Gauge Theories*, Phys. Rev. **155** (1967) 1554–1561.

[9] ATLAS Collaboration, *Combined Coupling Measurements of the Higgs-Like Boson with the ATLAS Detector Using up to 25 fb^{-1} of Proton-Proton Collision Data*, Tech. Rep. ATLAS-CONF-2013-034, CERN, Geneva (2013).

[10] S. Chatrchyan et al., *Observation of a New Boson with Mass near 125 GeV in pp Collisions at sqrt(s) = 7 and 8 TeV* (2013), `arXiv:1303.4571`.

[11] P. Ade et al., *Planck 2013 Results. I. Overview of products and scientific results* (2013), `arXiv:1303.5062`.

[12] A. Unsöld and B. Baschek, *Der neue Kosmos*, Springer (2005).

[13] A. Sakharov, *Violation of CP Invariance, C Asymmetry, and Baryon Asymmetry of the Universe*, JETP Lett. **5** (1967) 24.

[14] J. H. Christenson, J. W. Cronin, V. L. Fitch and R. Turlay, *Evidence for the 2π Decay of the K_2^0 Meson*, Phys. Rev. Lett. **13** (1964) 138–140.

[15] M. Kobayashi and T. Maskawa, *CP-Violation in the Renormalizable Theory of Weak Interaction*, Prog. Theor. Phys. **49** (1973) 652–657.

[16] S. W. Herb et al., *Observation of a Dimuon Resonance at 9.5 GeV in 400-GeV Proton-Nucleus Collisions*, Phys. Rev. Lett. **39** (1977) 252–255.

[17] A. B. Carter and A. I. Sanda, *CP Violation in B-Meson Decays*, Phys. Rev. D **23** (1981) 1567–1579.

[18] I. I. Bigi and A. I. Sanda, *Notes on the Observability of CP Violations in B Decays*, Nuclear Physics B **193** (1981) 85 – 108.

[19] K. Abe et al., *Observation of Large CP Violation in the Neutral B Meson System*, Phys. Rev. Lett. **87** (2001) 091802, `arXiv:hep-ex/0107061`.

[20] B. Aubert et al., *Observation of CP Violation in the B Meson System*, Phys. Rev. Lett. **87** (2001) 091801, `arXiv:hep-ex/0107013`.

[21] J. Beringer et al. (Particle Data Group), *2012 Review of Particle Physics*, Phys. Rev. D **86** (2012) 010001, http://pdglive.lbl.gov/.

[22] M. Bona et al., *Constraints on new Physics from the Quark Mixing Unitarity Triangle*, Phys. Rev. Lett. **97** (2006) 151803, `arXiv:hep-ph/0605213`.

[23] A. Lenz and U. Nierste, *Theoretical Update of $B_s^0 - \overline{B}_s^0$ Mixing*, JHEP **0706** (2007) 072, `arXiv:hep-ph/0612167`.

[24] G. Aad et al., *Time-Dependent Angular Analysis of the Decay $B_s^0 \to J/\psi\phi$ and Extraction of $\Delta\Gamma_s$ and the CP-Violating Weak Phase ϕ_s by ATLAS*, JHEP **1212** (2012) 072, `arXiv:1208.0572`.

[25] ATLAS Collaboration, *Flavour Tagged Time Dependent Angular Analysis of the $B_s \to J/\psi\phi$ Decay and Extraction of $\Delta\Gamma$ and the Weak Phase ϕ_s in ATLAS*, Tech. Rep. ATLAS-CONF-2013-039, CERN, Geneva (2013).

[26] C. Heller, *Measurement of ϕ_s, $\Delta\Gamma_s$ and Lifetime in $B_s \to J/\psi\phi$ at ATLAS and CMS*, Tech. Rep. ATL-PHYS-PROC-2013-135, CERN, Geneva (2013).

[27] ATLAS Collaboration, *Study of Alignment-Related Systematic Effects on the ATLAS Inner Detector Tracking*, Tech. Rep. ATLAS-CONF-2012-141, CERN, Geneva (2012).

[28] E. Rutherford, *The Scattering of α and β Particles by Matter and the Structure of the Atom*, Philosophical Magazine Series 6 **21** (1911) 669–688.

[29] D. Griffiths, *Introduction to Elementary Particles*, Wiley, New York (1987).

[30] C. Rubbia, *Experimental Observation of the Intermediate Vector Bosons W^+, W^-, and Z*, Rev. Mod. Phys. **57** (1985) 699–722.

[31] C. S. Wu, E. Ambler, R. W. Hayward, D. D. Hoppes and R. P. Hudson, *Experimental Test of Parity Conservation in Beta Decay*, Phys. Rev. **105** (1957) 1413–1415.

[32] W. Pauli, *Niels Bohr and the Development of Physics*, McGraw-Hill (1955).

[33] N. Cabibbo, *Unitary Symmetry and Leptonic Decays*, Phys. Rev. Lett. **10** (1963) 531–533.

[34] S. L. Glashow, J. Iliopoulos and L. Maiani, *Weak Interactions with Lepton-Hadron Symmetry*, Phys. Rev. D **2** (1970) 1285–1292.

[35] L. Wolfenstein, *Parametrization of the Kobayashi-Maskawa Matrix*, Phys. Rev. Lett. **51** (1983) 1945–1947.

[36] G. Branco, L. Lavoura and J. Silva, *CP Violation*, vol. 103 of *International series of monographs on physics*, Clarendon Press, Oxford (1999).

[37] A. J. Buras, M. E. Lautenbacher and G. Ostermaier, *Waiting for the Top Quark Mass, $K^+ \to \pi^+\nu\bar{\nu}$, $B_0^s - \bar{B}_0^s$ Mixing and CP Asymmetries in B decays*, Phys. Rev. D **50** (1994) 3433–3446, `arXiv:hep-ph/9403384`.

[38] C. Jarlskog and R. Stora, *Unitarity Polygons and CP Violation Areas and Phases in the Standard Electroweak Model*, Phys. Lett. B **208** (1988) 268.

[39] I. Bigi and A. Sanda, *CP Violation*, Cambridge University Press, Cambridge (2009).

[40] J. Charles et al., *CP Violation and the CKM matrix: Assessing the Impact of the Asymmetric B Factories*, Eur. Phys. J. C **41** (2005) 1–131, updated results and plots availvable at: http://ckmfitter.in2p3.fr, arXiv:hep-ph/0406184.

[41] Y. Grossman, *Introduction to Flavor Physics*, CERN Yellow Report CERN-2010-002 (2010) 111–144, arXiv:1006.3534.

[42] M. Artuso, E. Barberio and S. Stone, *B Meson Decays*, PMC Phys. A **3** (2009) 3, arXiv:0902.3743.

[43] A. J. Buras, *Flavor Dynamics: CP Violation and Rare Decays*, A. Zichichi (ed.), *Theory and experiment heading for new physics. Proceedings, 38th course of the International School of subnuclear physics, Erice, Italy, August 27-September 5, 2000* (2001) 200–337, arXiv:hep-ph/0101336.

[44] P. Ball and R. Fleischer, *An Analysis of B_s Decays in the Left-Right Symmetric Model with Spontaneous CP Violation*, Phys. Lett. B **475** (2000) 111–119, arXiv:hep-ph/9912319.

[45] I. Dunietz, R. Fleischer and U. Nierste, *In Pursuit of New Physics with B_s Decays*, Phys.Rev. D **63** (2001) 114015, arXiv:hep-ph/0012219.

[46] A. Lenz et al., *Anatomy of New Physics in $B - \bar{B}$ Mixing*, Phys. Rev. D **83** (2011) 036004, arXiv:1008.1593.

[47] R. Harnik, D. T. Larson, H. Murayama and A. Pierce, *Atmospheric Neutrinos Can Make Beauty Strange*, Phys. Rev. D **69** (2004) 094024, arXiv:hep-ph/0212180.

[48] M. Antonelli et al., *Flavor Physics in the Quark Sector*, Phys. Rept. **494** (2010) 197–414, arXiv:0907.5386.

[49] A. S. Dighe, I. Dunietz, H. J. Lipkin and J. L. Rosner, *Angular Distributions and Lifetime Differences in $B_s \to J/\psi\phi$ Decays*, Phys. Lett. B **369** (1996) 144–150, arXiv:hep-ph/9511363.

[50] F. Azfar et al., *Formulae for the Analysis of the Flavor-Tagged Decay $B_s^0 \to J/\psi\phi$*, JHEP **1011** (2010) 158, arXiv:1008.4283.

[51] S. Stone and L. Zhang, *S-waves and the Measurement of CP Violating Phases in B_s Decays*, Phys. Rev. D **79** (2009) 074024, arXiv:0812.2832.

[52] Y. Xie, P. Clarke, G. Cowan and F. Muheim, *Determination of $2\beta_s$ in $B_s^0 \to J/\psi K^+K^-$ Decays in the Presence of a K^+K^- S-Wave Contribution*, JHEP **0909** (2009) 074, arXiv:0908.3627.

[53] E. Norrbin and T. Sjostrand, *Production and Hadronization of Heavy Quarks*, Eur. Phys. J. C **17** (2000) 137–161, arXiv:hep-ph/0005110.

[54] T. Sjostrand, S. Mrenna and P. Z. Skands, *PYTHIA 6.4 Physics and Manual*, JHEP **0605** (2006) 026, arXiv:hep-ph/0603175.

[55] A. Lenz and U. Nierste, *Numerical Updates of Lifetimes and Mixing Parameters of B Mesons*, *CKM unitarity triangle. Proceedings, 6th International Workshop, CKM 2010, Warwick, UK, September 6-10, 2010* (2011) arXiv:1102.4274.

[56] T. Aaltonen et al., *Measurement of the Bottom-Strange Meson Mixing Phase in the Full CDF Data Set*, Phys. Rev. Lett. **109** (2012) 171802, arXiv:1208.2967.

[57] V. M. Abazov et al., *Measurement of the CP-Violating Phase $\phi_s^{J/\psi\phi}$ Using the Flavor-Tagged Decay $B_s^0 \to J/\psi\phi$ in 8 fb^{-1} of $p\bar{p}$ Collisions*, Phys. Rev. D **85** (2012) 032006, arXiv:1109.3166.

[58] CMS Collaboration, *Measurement of the Bs Lifetime Difference*, Tech. Rep. CMS-PAS-BPH-11-006, CERN, Geneva (2012).

[59] R. Aaij et al., *Measurement of CP Violation and the B_s^0 Meson Decay Width Difference with $B_s^0 \to J/\psi K^+K^-$ and $B_s^0 \to J/\psi\pi^+\pi^-$ Decays*, Tech. Rep. LHCB-PAPER-2013-002, CERN (2013), arXiv:1304.2600.

[60] O. S. Brüning et al., *LHC Design Report*, CERN, Geneva (2004), CERN-2004-003-V-1.

[61] ATLAS Collabortion, *ATLAS Detector and Physics Performance: Technical Design Report, 1*, Technical Design Report ATLAS, CERN, Geneva (1999).

[62] ATLAS Collaboration, *The ATLAS Experiment at the CERN Large Hadron Collider*, JINST **3** (2008) S08003.

[63] M. Elsing and T. Schoerner-Sadenius, *Configuration of the ATLAS Trigger System* (2003), arXiv:physics/0306046.

[64] ATLAS Collaboration, *ATLAS Tunes of PYTHIA 6 and Pythia 8 for MC11*, Tech. Rep. ATL-PHYS-PUB-2011-009, CERN, Geneva (2011).

[65] M. Smizanska, *PythiaB an Interface to Pythia6 Dedicated to Simulation of Beauty Events*, Tech. Rep. ATL-COM-PHYS-2003-038, CERN, Geneva (2003), aTLAS members access only.

[66] S. Agostinelli et al., *Geant4: a Simulation Toolkit*, Nuclear Instruments and Methods in Physics Research Section A: Accelerators, Spectrometers, Detectors and Associated Equipment **506** (2003) 250 – 303.

[67] ATLAS Collaboration, *Atlas Computing: Technical Design Report*, CERN, Geneva (2005).

[68] P. Řezníček, *Measurement of the B_d^0 Meson Lifetime at ATLAS Detector*, PhD thesis, Charles University, Prague (2012).

[69] V. Kostyukhin, *VKalVrt - Package for Vertex Reconstruction in ATLAS.*, Tech. Rep. ATL-PHYS-2003-031, CERN, Geneva (2003).

[70] F. James and M. Roos, *Minuit: A System for Function Minimization and Analysis of the Parameter Errors and Correlations*, Comput. Phys. Commun. **10** (1975) 343–367.

[71] R. Brun and F. Rademakers, *ROOT An Object Oriented Data Analysis Framework*, Nuclear Instruments and Methods in Physics Research Section A: Accelerators, Spectrometers, Detectors and Associated Equipment **389** (1997) 81 – 86.

[72] M. Abramowitz and I. A. Stegun, *Handbook of Mathematical Functions with Formulas, Graphs, and Mathematical Tables* , Dover (1972), online version available at http://people.math.sfu.ca/ cbm/aands/.

[73] A. Dewhurst, *A Study of $B_s \to J/\psi\phi$ and $B_d \to J/\psi K^{0*}$ Decays with the ATLAS Experiment*, PhD thesis, Lancaster University (2009).

[74] J. A. C. Weideman, *Computation of the Complex Error Function*, SIAM J. Numer. Anal. **31** (1994) 1497–1518.

[75] L. B. Oakes, *Measurement of the CP Violating Phase β_s in $B_s^0 \to J/\psi\phi$ Decays*, PhD thesis, St Cross College, Oxford (2010).

[76] G. Punzi, *Comments on Likelihood Fits with Variable Resolution* (2004), `arXiv:physics/0401045`.

[77] G. Aad et al., *Measurement of the Λ_b^0 Lifetime and Mass in the ATLAS Experiment*, Phys. Rev. D **87** (2013) 032002, arXiv:1207.2284.

[78] R. Aaij et al., *Measurement of the CP-Violating Phase ϕ_s in the Decay $B_s^0 \to J/\psi\phi$*, Phys. Rev. Lett. **108** (2012) 101803, arXiv:1112.3183.

[79] R. Aaij et al., *Determination of the Sign of the Decay Width Difference in the B_s System*, Phys. Rev. Lett. **108** (2012) 241801, arXiv:1202.4717.

[80] J. Alison et al., *Alignment of the ATLAS Inner Detector Tracking System with 2010 LHC Proton-Proton Collisions at $\sqrt{s}$ = 7 TeV*, Tech. Rep. ATLAS-COM-CONF-2011-013, CERN, Geneva (2010).

[81] G. Aad et al., *Charged-particle multiplicities in pp interactions measured with the ATLAS detector at the LHC*, New J. Phys. **13** (2011) 053033, arXiv:1012.5104.

[82] G. Aad et al., *Measurement of Upsilon Production in 7 TeV pp Collisions at ATLAS*, Phys. Rev. D **87** (2013) 052004, arXiv:1211.7255.

[83] C. Heller, *Summary of Measurments of B_s Lifetime and Decay Width Difference*, Tech. Rep. ATL-COM-PHYS-2012-1303, CERN, Geneva (2012), aTLAS members access only.

[84] LHCb Collaboration, *Tagged Time-Dependent Angular Analysis of $B_s^0 \to J/\psi\phi$ Decays at LHCb, 47th Rencontres de Moriond on Electroweak Interactions and Unified Theories, La Thuile, Italy, 3 - 10 Mar 2012* (2012) .

[85] R. Aaij et al., *Measurement of the B_s Effective Lifetime in the $J/\psi f_0(980)$ Final State*, Phys. Rev. Lett. **109** (2012) 152002, arXiv:1207.0878.

[86] T. Aaltonen et al., *Measurement of Branching Ratio and B_s^0 Lifetime in the Decay $B_s^0 \to J/\psi f_0(980)$ at CDF*, Phys. Rev. D **84** (2011) 052012, arXiv:1106.3682.

[87] R. Aaij et al., *Measurement of the Effective $B_s^0 \to K^+K^-$ Lifetime*, Phys. Lett. B **716** (2012) 393–400, arXiv:1207.5993.

[88] K. De Bruyn et al., *Branching Ratio Measurements of B_s Decays*, Phys. Rev. D **86** (2012) 014027, arXiv:1204.1735.

[89] T. Aaltonen et al., *Measurement of the B_s Lifetime in Fully and Partially Reconstructed $B_s \to D_s^-(\phi\pi^-)X$ Decays in $\bar{p}-p$ Collisions at $\sqrt{s} = 1.96$ TeV*, Phys. Rev. Lett. **107** (2011) 272001, `arXiv:1103.1864`.

[90] V. Abazov et al., *A Precise Measurement of the B_s^0 Lifetime*, Phys. Rev. Lett. **97** (2006) 241801, `arXiv:hep-ex/0604046`.

[91] ATLAS Collaboration, *Observation of the $B^\pm$ meson in the decay $B^\pm \to J/\psi(\mu^+\mu^-)K^\pm$ in ATLAS*, Tech. Rep. ATLAS-CONF-2010-098, CERN (2010).

[92] ATLAS Collaboration, *Commissioning of the ATLAS High-Performance b-Tagging Algorithms in the 7 TeV Collision Data*, Tech. Rep. ATLAS-CONF-2011-102, CERN, Geneva (2011).

[93] M. Cacciari, G. P. Salam and G. Soyez, *The Anti-k_t Jet Clustering Algorithm*, JHEP **0804** (2008) 063, `arXiv:0802.1189`.

[94] ATLAS Collaboration, *Measurement of the B^0 and B_0^s Lifetimes in the Decay Modes $B^0 \to J/\psi K^{*0}$ and $B_s^0 \to J/\psi\phi$ in ATLAS*, Tech. Rep. ATLAS-CONF-2011-092, CERN (2011).

[95] E. Prinker, *Parameterization of ATLAS Detector Efficiency with Spherical harmonics for the Decay $B_s^0 \to J/\psi\phi$*, Bachelor thesis, Ludwig-Maximilans-Universität München (2012).

List of Figures

List of Tables

Acknowledgements

Finally I would like to thank many people who helped and supported me during the last three years.

First of all, I would like to thank my supervisor Prof. Dr. Jochen Schieck for giving me the opportunity to write this thesis and giving me the chance to work in the fascinating field of elementary particle physics. I would also like to thank him for taking care of the financial support during my time at the Excellence Cluster Universe and making numerous trips to CERN and conferences possible.

I would like to thank Prof. Dr. Christian Kiesling for agreeing to be referee of my thesis and arouse my interest for particle physics during his lectures at the university.

My thanks also go to Dr. Pavel Řezníček and Dr. Louise Oakes for their advice and discussions about computing, analysis techniques and physics. Without their help this thesis would not have been possible.

Moreover I would like to thank the member of the ATLAS B-physics group who contributed to the analysis: Mária Smižanská, Alastair Dewhurst, Adam Barton, Tatjana Jovin, James Walder, Tomas Jakoubek, William Dearneley and all the others.

Last but not least I would like to thank my girlfriend, my dear friend Joris and my father for proofreading the thesis despite not being acquainted with the subject.